Three dimensional channeling flow in fractured reservoir

Tohoku University
Graduate School of Environmental Studies

Three dimensional channeling flow in fractured reservoir

(き裂型貯留層における 3 次元チャネリングフロー)

A Dissertation in
Environmental Studies
by
Takuya Ishibashi

Submitted in Partial Fulfillment
of the Requirements
for the Degree of

Doctor of Philosophy

January 2014

The dissertation of Takuya Ishibashi was reviewed and approved by the following:

Noriyoshi Tsuchiya
Professor of Graduate School of Environmental Studies
Dissertation Advisor
Chair of Committee

Toshiyuki Hashida
Professor of Graduate School of Engineering

Takatoshi Ito
Professor of Institute of Fluid Science

Noriaki Watanabe
Assistant Professor of Graduate School of Environmental Studies

ABSTRACT

In the Earth's crust, rock fractures play important roles on fluid flow and heat/mass transfer with fluid, since fractures usually have much greater permeability than the matrix permeability. An accurate understanding of the flow and transport characteristics through rock fracture networks is of critical importance in many engineering and scientific applications, and will help us to propose a solution to current energy and environmental problems or natural disaster prevention. With respect to a single rock fracture, it is widely acceptable that the aperture distribution is heterogeneous and fluid flow within it is characterized by formation of preferential flow paths (i.e. channeling flow). Considering this fact, to capture the reality of the fluid flow within a fracture network, it is desirable to explicitly consider the formation of three dimensional (3-D) preferential flow paths within a fracture network (i.e., 3-D channeling flow). However, to date there is no practical modeling method that precisely represents the 3-D channeling flow. Additionally, a prediction of channeling flow through subsurface rock fractures beyond laboratory scale is also a remained issue. Objectives of this study are developing a novel method to analyze and predict channeling flow in actual fractured reservoirs and clarifying the characteristics and impacts of the 3-D channeling flow. In this study, both experimental and numerical approaches are taken to achieve the objective.

In Chapter Ⅱ, a fluid flow experiment on a cylindrical granite sample containing two intersecting fractures are conducted. At constant confining pressure, water is supplied to the sample via a single inlet port, and the effluent is collected using four isolated outlet ports. The flow rate varies widely among these ports, which demonstrates that the 3-D channeling flow must be considered to interpret fluid flow even in the simplest fracture network. To simulate 3-D channeling flow within rock fracture networks, a novel discrete fracture network (DFN) model simulator, GeoFlow, is developed, where rock fractures are modeled by pairs of rough fracture surfaces having heterogeneous aperture distributions. A fluid flow simulation is conducted with GeoFlow, where aperture distributions within the two fractures are determined by using fracture surface topography data. Despite the simplicity of the simulation, GeoFlow revealed a 3-D channeling flow within the sample and successfully reproduced the experimental result. Thus, the significant potential of GeoFlow to predict 3-D channeling flow in a fracture

network is revealed

In Chapter Ⅲ, for granite fractures of various scales (0.05 m × 0.075 m, 0.1 m × 0.15 m, 0.2 m × 0.3 m), the fracture aperture distribution under confining stress (10, 20, and 30 MPa) and the fluid flow through the aperture distributions are determined using data of the fracture surface topography and measured fracture permeability. Subsequently, the scale dependencies of the aperture distribution and the resulting fluid flow characteristics for rock fractures are evaluated under the confining stress. As a significant result, it is revealed that the contact area in the fracture plane is independent of scale. The scale-independent contact areas of fractures with and without a shear displacement are approximately 40% and 60%, respectively. By combining this characteristic with the fractural nature of the fracture surface, a method for predicting fracture aperture distributions beyond laboratory scale is developed. In this method, the aperture distribution of a fracture of any size can be predicted by simply placing the two fractal fracture surfaces in contact so that the fracture has the scale-independent contact area. The validity of the proposed method was revealed through the reproduction of the results in a laboratory investigation and the maximum aperture-fracture length relations, which have been reported in the literature, for natural fractures (i.e., joints and faults).

In Chapter Ⅳ, aperture distributions and fluid flows are numerically determined for rock fractures with various combination of fracture scale and shear displacement by using the prediction method of fracture aperture distributions beyond laboratory scale, which is developed in Chapter Ⅲ. Through evaluating the aperture distributions and fluid flows, fluid flow characteristics of subsurface rock fractures under confining stress (up to ~ 100 MPa) are revealed as followings; flow area within a fracture plane is limited to 5-25% regardless of fracture scale (m), l, or shear displacement (m), δ, since preferential flow paths are consistently formed within subsurface rock fractures (i.e. channeling flow). This fact also indicates that the noncontact area with stagnant fluid within rock fractures is approximately 33-53%. Furthermore, mean aperture (mm), e_m, and permeability (m^2), k, of rock fractures are respectively formulated as $e_{mean} = (1.42 \times 10) \cdot L^{0.66} \cdot (\delta / L)^{0.60}$ and $k = (2.66 \times 10^{-6}) \cdot L^{1.43} \cdot (\delta / L)^{1.21}$, which can reproduce the mean apertures and permeabilities of real fractures. Owing to these universal modeling, we can now create realistic discrete fracture network models of a fractured reservoir

for GeoFlow simulation. Additionally, these results are also expected to be fundamentals to reach a new insight for permeability evolutions of rock fractures (natural faults) caused by earthquakes.

In Chapter Ⅴ, realistic DFN models, where heterogeneous aperture distributions are given for individual fractures depending on their scale and shear displacement under confining stress, are created for an actual fracture reservoir (i.e. the Yufutsu oil/gas field) and fluid flows in the reservoir are simulated. Through a series of the fluid flow simulations, it is revealed that the reality of fluid flow within a fractured reservoir is 3-D channeling flow, which should be considered for predicting the optimum well locations for a fractured reservoir. Specifically, three order of magnitude difference in the productivities between the neighboring two wells, which is indeed observed in the Yufutsu field, is reproduced successfully for the first time by considering the occurrence of the 3-D channeling flow. Specifically, the impact of 3-D channeling flow is expected to be significant in the domain where the degree of fracture connectivity is relatively limited. Moreover, there are some concerns that we will come to the wrong conclusions for development or utilization of a fractured reservoir, if the occurrence of 3-D channeling flow within the reservoirs is ignored. As long as highly-reliable discrete fracture networks are created for a fracture reservoir on the basis of 3-D seismic data, crustal stress data, and so on, we can now map the realistic flow path distribution (i.e. 3-D channeling flow) with GeoFlow.

As described above, a novel method to analyze and predict 3-D channeling flow in actual fractured reservoirs is established for the first time. Owing to the novel method, our understandings of fluid flow characteristics (i.e. 3-D channeling flow characteristics) in fractured reservoirs are significantly promoted. Considering the practicality of our suggested method, it is desirable that the method will be applied to fractured reservoirs of various fields hereafter. If such results are accumulated, our understandings for the reality of fluid flow in subsurface rock fracture networks are further advanced. In the future, it is also desirable that the following relationships are clarified; (1) 3-D channeling flow and heat extraction, (2) 3-D channeling flow and multi-phase flow and transport process, and (3) 3-D channeling flow and mechanisms of induced seismicity in fractured reservoirs.

Table of Contents

List of Tables xiii

List of Figures ix

Acknowledgements xiv

Chapter Ⅰ Introduction 1

1.1. Background 1
1.2. Previous studies 4
1.3. Objectives and thesis structure 8

Chapter Ⅱ GeoFlow: A novel model simulator for prediction of the three dimensional channeling flow in a rock fracture network 10

2.1. Introduction 10
2.2. Methods 11
2.2.1. Multiple-fracture flow experiment 11
2.2.2. GeoFlow simulation 14
2.3. Results and Discussion 18
2.4. Conclusions 23

Chapter Ⅲ Beyond-laboratory-scale prediction for channeling flows through subsurface rock fractures 24

3.1. Introduction 24
3.2. Methods 25
3.2.1.Evaluation of fracture aperture distributions and fluid flows on the laboratory scale 25
3.2.2. Prediction of fracture aperture distributions and fluid flows beyond laboratory scale 30
3.3. Results and Discussion 31
3.3.1. Channeling flows through heterogeneous aperture distributions of laboratory scale fractures 31
3.3.2. Validity of the method for predicting fracture aperture distributions beyond the laboratory scale 41
3.3.3. Scale dependency of a channeling flow through a heterogeneous fracture aperture distributions 48
3.4. Conclusions 51
Appendix 3-A. Spectral method for modeling a self-similar fracture surface 51
Appendix 3-B. Method for modeling the other fracture surface 53
Nomenclature & Greek symbols 55

Chapter Ⅳ Universal modeling of fluid flow characteristics through subsurface rock fractures 56

4.1. Introduction 56
4.2. Methods 57

4.3. Results and Discussion.....59
4.3.1. Channeling flows through heterogeneous aperture distributions of the field scale subsurface rock fractures.....59
4.3.2. Mean aperture and permeability of subsurface rock fracture formulated by fracture scale and shear displacement.....69
4.4. Conclusions.....75

Chapter Ⅴ Modeling of three-dimensional channeling flow in a fractured reservoir with GeoFlow.....76

5.1. Introduction.....76
5.2. Reviews for three orders of magnitude difference in well productivity observed in a fractured reservoir (the Yufutsu oil/gas field).....77
5.3. Methods.....81
5.3.1. Modeling of a fractured reservoir.....81
5.3.2. Analysis of fluid flow in a fractured reservoir.....88
5.4. Results and Discussion.....89
5.4.1. Reproduction of the huge difference in well productivity.....89
5.4.2. Clarification of the mechanism causing the huge difference in well productivity.....107
5.5. Conclusions.....114
Appendix 5-A. Representation of the shape of rock fractures.....115
Appendix 5-B. Change in the fluid flow characteristics of a fracture network depending on the aperture distributions of individual fractures.....119

Chapter Ⅵ Conclusions.....124

References.....127

Publications.....136

List of Tables

Table 3-1. Parameter values characterizing the channeling flow through the heterogeneous aperture distribution of the real fracture. 39

Table 3-2. Parameter values characterizing the channeling flow through the heterogeneous aperture distributions of the predict fracture under confining stress. 45

Table 4-1. Parameters used in the numerical modeling of rock fracture surfaces. 57

Table 4-2. Parameters characterizing the channeling flow within heterogeneous aperture distributions of numerically modeled fractures in field-scale. 66

Table 4-3. Fitting parameters of α_1, α_2, β_1, and β_2 determined for different scales of fractures. .69

Table 5-1. Parameter set for the fluid flow simulations of the Yufutsu oil/gas field. 87

Table 5-2. Permeabilities of the fractured reservoir evaluated with GeoFlow models and flowing fluid existing volumes in the direction of x-, y-, and z-axis. The ensemble average values for permeability and fluid existing volume are also shown herein. 92

Table 5-3. Dependencies of the flowing fluid existing volume on the shear displacement of critically-stressed fractures for GeoFlow model and Conventional DFN model. 99

Table 5-4. Dependencies of the productivities of Well A and Well B on the shear displacement of critically-stressed fractures for GeoFlow model and Conventional DFN model. 105

Table A-1. Permeabilities of the fracture networks and flowing fluid existing volumes evaluated for squared-shaped fracture network and circle-shaped fracture network. 119

Table A-2. Permeabilities of the fracture networks and flowing fluid existing volumes evaluated for fracture networks with different sets of aperture distributions. 123

List of Figures

Figure 1-1. Schematic illustration of the Enhanced Geothermal Systems (modified after *Huang* (2012)).....3

Figure 1-2. Schematic illustration of the seismic source distribution at downdip portion of the subduction zone (modified after *Ito et al.* (2007)). 4

Figure 1-3. Schematic illustration of modeling approaches for a fractured rock with (a) continuum model and (b) three dimensional discrete fracture network (DFN) model (modified after *Illman et al.* (2009) and *Frampton and Cvetkovic* (2010)). 5

Figure 1-4. Schematic illustration of the reality of fluid flow within a subsurface rock fracture. Preferential flow paths are formed within a heterogeneous aperture distribution of rock fracture (modified after *Watanabe et al.* (2009)).....7

Figure 1-5. Channeling flow seen as discrete outflow of ground water from a continuous fracture at the Tatsunokuchi gorge in Sendai City, Japan.....7

Figure 2-1. (a) Multiple-fracture sample containing two intersecting mated tensile fractures (Fractures A and B), and (b) the experimental setup for the evaluation of uneven fluid flow within the sample under confining pressure.....13

Figure 2-2. Relationship between the total flow rate and hydraulic pressure difference for the multiple-fracture sample at 36 MPa. The linear curve shows the result of the least squares regression at hydraulic pressures of ≤ 0.6 MPa.....14

Figure 2-3. (a) 3-D matrix containing a network of the 2-D fractures with aperture distributions, (b) which is divided into the matrix elements and is finally converted into the equivalent permeability continuum, in which the Darcy flow through the element interface is calculated. 17

Figure 2-4. (a) Equivalent permeability continuum model of the multiple-fracture sample at a confining pressure of 36 MPa, as represented by a permeability distribution, and (b) the fluid flow model of the sample, as represented by a distribution of flow rate for the unidirectional fluid flow from top to bottom (hatched boundaries: constant hydraulic pressure, other boundaries: non-flow), as derived by the GeoFlow simulation. 21

Figure 2-5. Comparison of the experimentally observed flow rate ratios for the ports and the numerical prediction by GeoFlow simulation for the fluid flow through the multiple-fracture sample. 23

Figure 3-1. 3-1. Cylindrical granite samples containing single tensile fractures of different sizes having either (a) no shear displacement or (b) a shear displacement of 5 mm in the radial direction.....26

Figure 3-2. Experimental system for permeability measurement of the fracture within the granite sample under confining stress. 29

Figure 3-3. Boundary conditions in the unidirectional fluid flow simulation for the fracture

aperture distribution created in a 0.25-mm square grid system. 29

Figure 3-4. Changes in the fracture permeability with fracture length for real laboratory-scale fractures with no shear displacement and with a shear displacement of 5 mm at confining stresses of from 10 to 30 MPa. 32

Figure 3-5. Representative results for the channeling flow within the heterogeneous aperture distribution of the real laboratory-scale fractures (a) with no shear displacement and (b) with a shear displacement of 5 mm. 34

Figure 3-6. Representative results for the histograms of the aperture for the real laboratory-scale fractures with (a) no shear displacement and (b) a shear displacement of 5 mm. 36

Figure 3-7. Changes in (a) the geometric mean of aperture and (b) the contact area for the real laboratory-scale fractures with no shear displacement and with a shear displacement of 5 mm at confining stresses of 10, 20, and 30 MPa. 37

Figure 3-8. Changes in the flow area with the fracture length for the real laboratory-scale fractures with no shear displacement and a shear displacement of 5 mm at confining stresses of 10, 20, and 30 MPa. 38

Figure 3-9. Representative results for the channeling flow within the heterogeneous aperture distribution of the predicted fractures (a) with no shear displacement and (b) with a shear displacement of 5 mm. 43

Figure 3-10. Comparisons of (a) the geometric mean of aperture and (b) the permeability between the predicted and the real laboratory-scale fractures with no shear displacement and with a shear displacement of 5 mm. The values for the real fractures are determined at confining stresses of 10, 20, and 30 MPa. 44

Figure 3-11. Comparison of the maximum aperture-fracture length relations between the predicted and the natural fractures. The results are for the predicted fractures with two types of shear displacement: (1) a constant shear displacement of 5 mm and (2) a shear displacement that is a constant 1% of the fracture length. One of the linear curves, $e_{max} = 2.5\times10^{-3}l^{0.48}$, corresponds to the relation of the joint, whereas the other linear curves correspond to the relations of the fault [*Schlische et al.*, 1996; *Schultz et al.*, 2008]. 47

Figure 3-12. Predicted typical changes in the (a) geometric mean of aperture, (b) the permeability, and (c) the flow area, all with respect to the fracture length, for fractures with no shear displacement (joints) and fractures with a constant ratio of shear displacement to fracture length (faults). 50

Figure 4-1. Length, width, and shear displacement defined for a fracture with shear displacement. 58

Figure 4-2. Representative results for the heterogeneous aperture distributions of numerically modeled fractures with various combinations of fracture scale and shear displacement under confining stress. 60

Figure 4-3. Representative results for the formation of preferential flow paths (i.e. channeling flow) within heterogeneous aperture distributions of numerically modeled fractures with

various combinations of fracture scale and shear displacement under confining stress. 62

Figure 4-4. Scale dependent changes in the formation of preferential flow paths (i.e. channeling flow) within heterogeneous aperture distributions of rock fractures with (a) 0.25% shear displacement and (b) 5.0% shear displacement.....64

Figure 4-5. Mean apertures of numerically created heterogeneous aperture distributions of subsurface rock fractures with various combinations of fracture scale and shear displacement. Approximated curves by Eq. 4-2 are represented herein.....67

Figure 4-6. Comparison of the maximum aperture-fracture length relations between the predicted and the natural fractures. Linear curves shown in the figure correspond to the relations of the fault [*Cowie and Scholz*, 1992; *Vermilye and Scholz*, 1992; *Schultz et al.*, 2008]. 67

Figure 4-7. (a) Fracture permeability and (b) Flow area of numerically created heterogeneous aperture distributions of subsurface rock fractures with various combinations of fracture scale and shear displacement. Approximated curves by Eq. 4-3 are represented in Figure 4-7a.....68

Figure 4-8. Changes in the fitting parameters, which constrain mean aperture (a) and permeability (b) of subsurface rock fractures.....70

Figure 4-9. Changes in (a) mean aperture and (b) permeability of subsurface rock fractures with increasing shear displacement, where fracture scale varies. 72

Figure 4-10. Changes in (a) mean aperture and (b) permeability of subsurface rock fractures with increasing fracture scale, where shear displacement varies. 74

Figure 5-1. (a) Index map showing the location of Yufutsu oil/gas field, and (b) Geological cross section of the Yufutsu field. Gr = Group. 78

Figure 5-2. (a) Locations of four wells (Well A, B, C, and D) in the Yufutsu oil/gas field. Study area of GeoFlow simulation in the present study is enclosed with bold line. Over the area, 3-D surface seismic data, which are shown as (b) seismic amplitude and (c) variance of seismic amplitude, are acquired. Furthermore, (d) fault-extraction processed data is also obtained based on the seismic data. 80

Figure 5-3. (a) Relationship between cumulative frequency of fractures and fracture length and (b) an example of created DFN for the Yufutsu oil/gas field. 83

Figure 5-4. Relationship between fracture permeability and fracture length for both noncritically-stressed fractures and critically-stressed fractures. 85

Figure 5-5. An example of permeability map for the equivalent permeability continuum of the Yufutsu oil/gas field evaluated in GeoFlow model. 87

Figure 5-6. Boundary conditions for (a) unidirectional fluid flow simulation and (b) radial fluid flow simulation.....88

Figure 5-7. (a) Permeabilities of the fractured reservoir evaluated with GeoFlow models and (b)

flowing fluid existing volumes for x-, y-, and z-directions. Distributions of fractures are stochastically equivalent for these 15 models, and the ensemble averages for each direction are shown with the different type of broken lines. 91

Figure 5-8. Permeability maps for the Yufutsu field evaluated with (a) GeoFlow model and (b) Conventional DFN model. Highly permeable zone in critically-stressed fractures are shown with colors. Note that the shear displacement of critically-stressed fractures is 4×10^{-3} (0.4%). 94

Figure 5-9. Flow path distributions for the Yufutsu field evaluated with (a) GeoFlow model and (b) Conventional DFN model. The shear displacement of critically-stressed fractures is 4×10^{-3} (0.4%). 97

Figure 5-10. Flow path distributions for the Yufutsu field evaluated with (a) GeoFlow model and (b) Conventional DFN model. The shear displacement of critically-stressed fractures is 1×10^{-3} (0.1%). 100

Figure 5-11. Flow path distributions for the Yufutsu field evaluated with (a) GeoFlow model and (b) Conventional DFN model. The shear displacement of critically-stressed fractures is 2×10^{-2} (2%). 101

Figure 5-12. Flow path distributions for the Yufutsu field evaluated with (a) GeoFlow model and (b) Conventional DFN model. The shear displacement of critically-stressed fractures is 4×10^{-2} (4%). 102

Figure 5-13. Dependencies of the fluid existing volume on the shear displacement of critically-stressed fractures evaluated with GeoFlow model (solid square symbols) and Conventional DFN model (open circle symbols). 103

Figure 5-14. Dependencies of the productivities of Well A and Well B on the shear displacement of critically-stressed fractures evaluated with (a) GeoFlow model and (b) Conventional DFN model. 106

Figure 5-15. Dependencies of the ratio of productivity of Well A to that of Well B on the shear displacement of critically-stressed fractures evaluated with GeoFlow model (solid square symbols) and Conventional DFN model (open circle symbols). Dashed line represents the approximated linear curve for the relationship evaluated with GeoFlow model. 107

Figure 5-16. Flow path distributions of the Yufutsu field in a state of nature for (a) x-direction, (b) y-direction, and (c) z-direction. Furthermore, (d) superimposed flow path distribution for the three directions is also shown. The shear displacement of critically-stressed fractures is 2×10^{-2}. 110

Figure 5-17. (a) Conceptual diagram of the network of critically-stressed fractures around Well B in the Yufutsu oil/gas field, and (b) Schematic illustration for the anisotropy of fluid flow characteristics of a single rock fracture with shear displacement. 113

Figure A-1. Conceptual illustration of conversion for the fracture shape. 115

Figure A-2. Permeability maps and flow path distributions evaluated for (a) squared-shaped fracture network and (b) circle-shaped fracture network. Model number of the stochastic

equivalent discrete fracture network is Network 08.....116

Figure A-3. Permeability maps and flow path distributions evaluated for (a) squared-shaped fracture network and (b) circle-shaped fracture network. Model number of the stochastic equivalent discrete fracture network is Network 10.....117

Figure A-4. Permeability maps and flow path distributions evaluated for (a) squared-shaped fracture network and (b) circle-shaped fracture network. Model number of the stochastic equivalent discrete fracture network is Network 14.....118

Figure A-5. Permeability maps and flow path distributions evaluated for the fracture network (aforementioned Network 08) where the model number of heterogeneous aperture distributions is (a) Aperture distribution 01, (b) Aperture distribution 02, (c) Aperture distribution 03, (d) Aperture distribution 04, and (e) Aperture distribution 05.....121

Acknowledgments

First and foremost, I thank my advisor, Prof. Noriyoshi Tsuchiya from Tohoku University, for not only giving me the opportunity to work in his group but also being a great mentor, scientific-wise and life wise. Prof. Tsuchiya is the best advisor and mentor I can ask for and I will always be grateful for his guidance and support and patience, and the faith he placed in me.

I thank my committee members: Prof. Toshiyuki Hashida, Prof. Takatoshi Ito, and Assistant. Prof. Noriaki Watanabe, all from Tohoku University, for taking the time to review this manuscript and for their help in developing various elements of the project. Dr. Watanabe has spent a lot of time in teaching me how to design experimental systems and discussing to advance my research, and helping me become an independent scientist. I sincerely thank Dr. Watanabe for his mentorship.

I thank Ass. Prof. Atsushi Okamoto and Assistant. Prof. Nobuo Hirano from Tohoku University for their support and guidance during the 6 years spending in Geomaterials and Energy science Laboratory. I sincerely thank Dr. Okamoto for giving me broad-ranging scientific knowledges.

I thank Dr. Kimio Watanabe from Renergies, Ltd. for coding GeoFlow simulator.

I thank Dr. Tetsuya Tamagawa, Dr. Kazuhiko Tezuka, Dr. Masahiko Yagi, Dr. Yusuke Kumano, Yutaka Ohsaki, and their group from Japan Petroleum Exploration Co., Ltd. for the excellent collaboration.

I thank Prof. Derek Elsworth, Prof. Chris Marone, Dr. Shugang Wang, Dr. Thomas P. McGuire, Divya Chandra, Rohan Belvalkar, Baisheng Zheng, Dr. Brett Carpenter, Dr. Hiroko Kitajima, Marco Scuderi, Steve Swavely, all from Pennsylvania State University, for their help during my stay at Pennsylvania State University in 2011. I sincerely thank Derek for his mentorship and all of his kindest helps.

I thank Assistant Prof. Akihisa Kizaki, Assistant. Prof. Hiroyuki Shimizu, Ass. Prof. Kiyotoshi Sakaguchi, Prof. Koji Matsuki, Assistant. Prof. Takahiro Watanabe, Prof. Takeshi Komai, Assistant. Prof. Tatsu Kuwatani, Prof. Yuichi Niibori, and Dr. Yusuke Mukuhira, all from Tohoku University, for many valuable discussions. I thank Ass. Prof. Hideaki Yasuhara from Ehime University, and Ass. Prof. Ikuo Katayama from Hiroshima University for many valuable discussions.

I thank Dr. Hiroshi Asanuma, Dr. Kasumi Yasukawa, Dr. Keiichi Sakaguchi, Dr. Shinsuke Nakao, Dr. Toshiyuki Tosya, Dr. Yuji Mitsuhata, all from National Institute of Advanced

Industrial Science and Technology, for many valuable discussions.

Thanks also to the many friends that I have made over the years, for their friendship and support that I have made my time in Tohoku University a lot of fun. In particular, I want to thank Keisuke Sakurai, Ryosuke Oyanagi, Ryo Yamada, and Yuki Kawada, great friends, not only for their willing help, but most importantly for his encouragement during my difficult time. I wish them the best in their career. Thanks also go to: Anna Suzuki, Chizu Sekiguchi, Goit Jay Prakash, Hanae Saisyu, Hiroki Ishihara, Keisuke Yagi, Masahiro Kajiwara, Michimasa Musya, Naoki Konda, Noriyuki Maki, Masato Uehara, Mikako Kondo, Takayuki Ono, Rei Takeda, Soryu Fujii, Teruhiro Ozawa, Tomohisa Saito, Yoshinobu Hatori, Yoshinori Matsubara, and all colleagues of Tsuchiya Laboratory.

This research was supported by a Grant-in Aid for JSPS Fellows (24・3097). I would like to express my gratitude and appreciation to Japanese Society for the Promotion of Science.

Lastly, I thank my parents and my brother for their unconditional love and wonderful support.

Chapter Ⅰ

Introduction

1.1. Background

In the Earth's crust, rock fractures play important roles on fluid flow and heat/mass transfer with fluid, since fractures usually have much greater permeability than the matrix permeability [*Durham*, 1994; *Watanabe et al.*, 2008, 2009]. An accurate understanding of the flow and transport characteristics through rock fracture networks is of critical importance in many engineering and scientific applications, and will help us to propose a solution to current energy and environmental problems or natural disaster prevention.

In the volcanic countries, which include our country, Japan, geothermal resource is one of the most promising renewable energies, and expected to be efficiently utilized rather than the atomic power generation. The significant advantage in geothermal resource utilization is that the emission of greenhouse gases associated with power generation is quite low. Specifically, the EGS (engineered geothermal system or enhanced geothermal system), where artificial fractures are created by hydraulic fracturing underground, has been studied over the years, and demonstration experiments for the EGS have been performed in several countries (Cooper Basin in Australia, Soultz in France, Ogachi and Hijiroi in Japan, and so on) [*Abe et al.*, 1999a, 1999b; *Niitsuma et al.*, 1999]. Additionally, a new concept of EGS in ductile formation zone is recently proposed. To demonstrate the feasibility of the development of EGS in ductile zone, Japan beyond-brittle project (JBBP) is launched [*Asanuma et al.*, 2012]. In development of these EGSs, rock fractures work as heat exchangers and pathways of geothermal fluids, and the conceptual diagram of the EGS is shown in Figure 1-1 [*Huang*, 2012]. So, one of the keys to lead the EGS project toward success is to understand fluid flow through rock fracture networks precisely.

The same is equally true of the development for fractured reservoirs of hydrocarbon. Fractured reservoirs of hydrocarbon have been recognized as well as the porous reservoirs for a long time, and it is estimated that more than 60% of the world's hydrocarbon reservoirs are fractured reservoir. Since the evaluation techniques of subsurface rock fractures have not been

established, the development of the fractured reservoirs is considered to be significantly difficult. However, the fracture evaluation techniques have also been accumulated in the non-petro sectors such as geothermal or geological disposal, and the potential of these techniques for the development of the fractured reservoirs has been revealed. For instance, commercial productions of hydrocarbon from fractured reservoirs are successfully achieved at the Rang Dong field (Vietnam) and the Yufutsu field (Japan) [*Agatsuma et al.*, 1996; *Isoe and Onobe*, 2001; *Matsuura et al.*, 2003; *Shiomoto et al.*, 2006].

In contrast, when we assess the long-term safety of CCS (Carbon Dioxide Capture and Storage) or geological disposal of the high-level radioactive waste, which are the essential technologies to be established for sustainable growth of the next generations, the flow and transport characteristics through rock fracture networks are still necessary to be understood precisely. This is because possible leakages of the carbon dioxide or the nuclear waste to the biosphere are considered through the fracture networks within the rock masses with low permeability [*Cvetkovic et al.*, 2004; *Cvetkovic and Frampton*, 2010; *Iding and Ringrose*, 2010].

Furthermore, fluid flow and mass/heat transport through rock fracture networks are also the key phenomenon in revealing the geophysical phenomenon, such as the earthquake mechanisms or the role of fluid during volcanic explosion [*Caine et al.*, 1996; *Curewitz and Karson*, 1997; *Ito et al.*, 2007; *Nakaya and Nakamura*, 2007]. For instance, Figure 1-2 shows conceptual illustration of the asperity model for downdip portion of the subduction zone. This area can be considered as a kind of fracture, where water can exist at non-asperities parts. Heterogeneous distribution of water at the subduction zone is essential in modeling the time-dependent destruction of asperities parts and the resulting earthquake generation processes.

Thus, the significant importance of clarifying the flow and transport characteristics through rock fracture networks is demonstrated. Although a numerical modeling is one of the most powerful ways to reveal these characteristics, to date there is no practical modeling method that precisely represents the reality of the fluid flow through rock fracture networks. For instance, three orders of magnitude difference in well productivity, which is observed in a fractured reservoir (i.e. the Yufutsu oil/gas field), has never been reproduced in the previous modeling, which implicates that further efforts of modifying the modeling for fluid flow

through rock fracture networks are required.

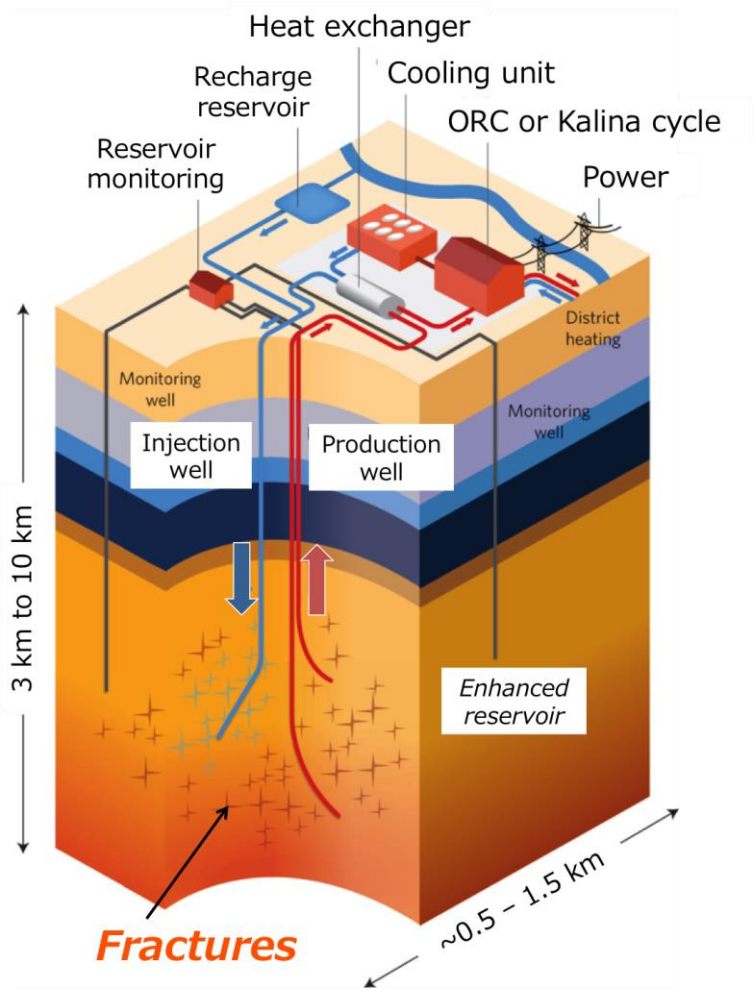

Figure 1-1. Schematic illustration of the Enhanced Geothermal Systems (modified after *Huang* (2012)).

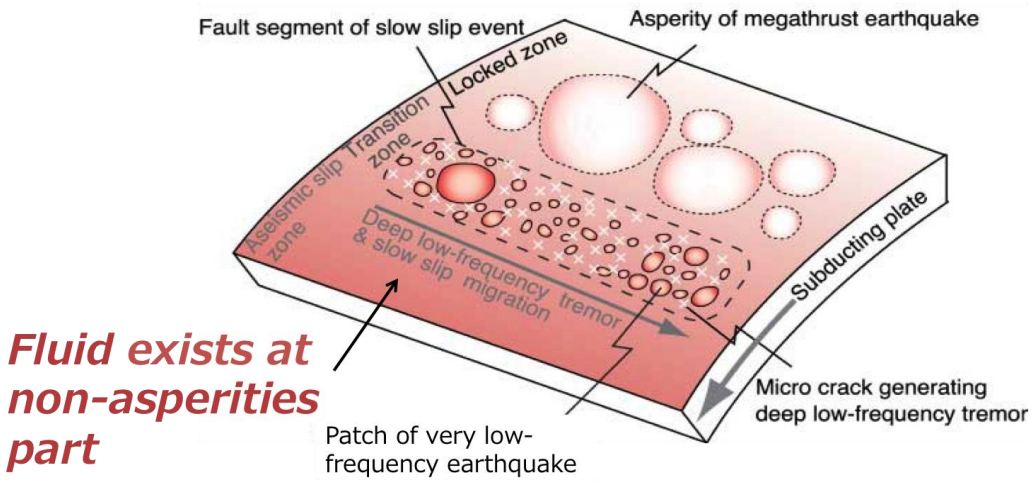

Figure 1-2. Schematic illustration of the seismic source distribution at downdip portion of the subduction zone (modified after *Ito et al.* (2007)).

1.2. Previous studies

In analyzing fluid flow and heat/mass transfer with fluid through rock fracture networks, numerical methods are more practical and effective than experimental methods, because it is difficult to conduct experiments using a multiple-fracture sample. With respect to numerical methods, modeling approaches for a fractured rock have traditionally been divided into two rough classes: continuum models and discrete fracture network (DFN) models [*Long et al.*, 1982; *Vesselinov et al.*, 2001; *Berkowitz,* 2002; *Ando et al.*, 2003; *Neuman,* 2005 *Illman et al.*, 2009; *Frampton and Cvetkovic.* 2010]. Furthermore, each class can be formulated in deterministic and stochastic frameworks. One example of continuum model is shown in Figure 1-3a, whereas that of DFN model is shown in Figure 1-3b. Continuum models are applied mainly for the prediction of fluid flow behavior averaged over a large domain. Single values of hydraulic parameters are defined at each point throughout the domain of interest in deterministic continuum models, while the interior bulk flow and transport properties of dominant fractured rock features, and remaining rock mass, are represented as separate correlated random function of space in stochastic continuum models. On the other hand, DFN models are best treated in a stochastic framework by considering Monte Carlo analyses based on multiple realizations of a fractured system, because complete field data for deterministic models are usually difficult to obtain. DFN models can naturally incorporate geometrical properties in fractures (fracture size,

aperture, location, orientation, and density), and as a result can account explicitly for the contribution of individual fractures on fluid flow, which cannot be considered properly in continuum models.

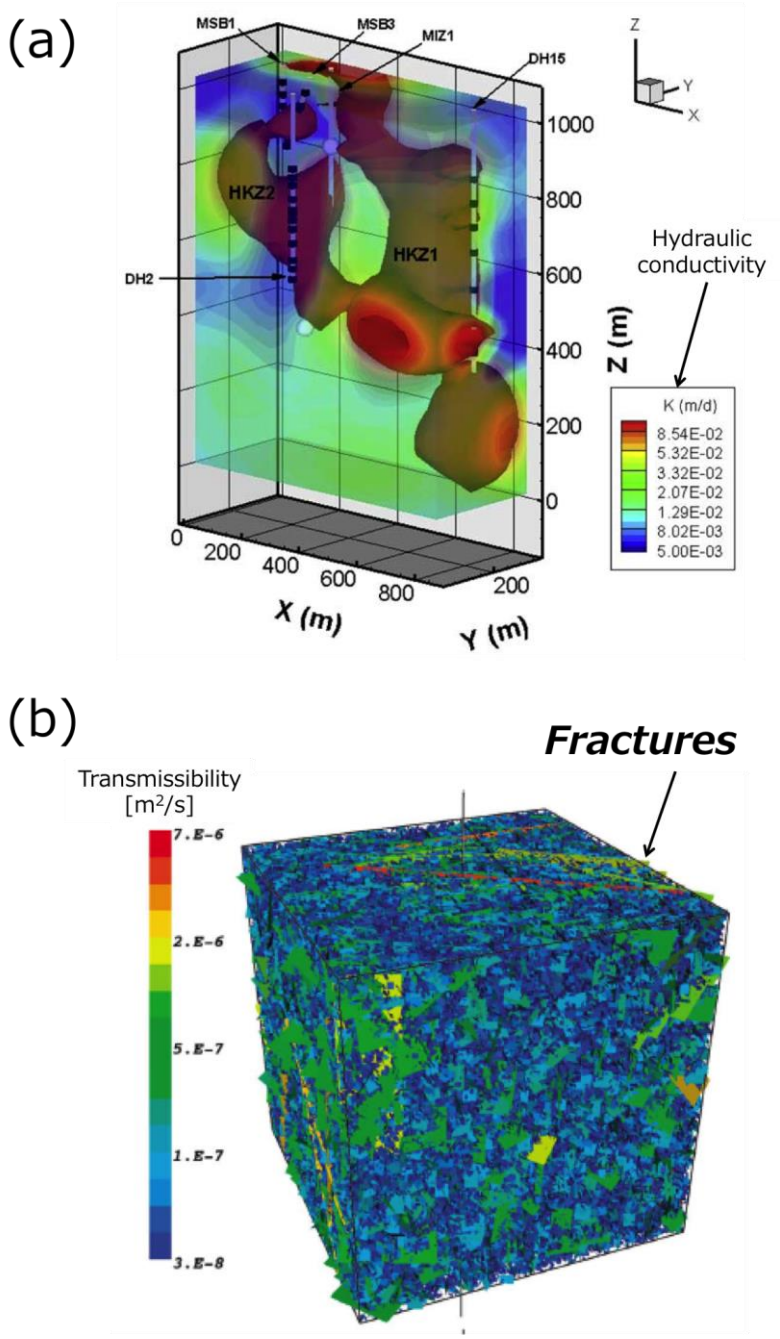

Figure 1-3. Schematic illustration of modeling approaches for a fractured rock with (a) continuum model and (b) three dimensional discrete fracture network (DFN) model (modified after *Illman et al.* (2009) and *Frampton and Cvetkovic* (2010)).

In the conventional DFN models, individual fractures are represented by pairs of parallel smooth plates having single aperture value [*Jing et al.*, 2000; *Min et al.*, 2004; *Klimczak et al.*, 2010; *Dreuzy et al.*, 2013]. However, fractures have heterogeneous aperture distributions because the apertures are formed by pairs of rough surfaces that are in partial contact with each other. Such a heterogeneous aperture distribution of rock fracture is precisely visualized using X-ray CT at atmospheric pressure or under confining stress [*Watanabe et al.*, 2011a, 2011b, and 2012]. Consequently, fluid flows through rock fractures are characterized by the formation of preferential flow paths (i.e., channeling flow) [*Brown*, 1987b and 1989; *Pyrak-Nolte et al.*, 1988; *Brown et al.*, 1995; *Brown et al.*, 1998; *Sausse*, 2002; *Watanabe et al.*, 2008; *Nemoto et al.*, 2009; *Talon et al.*, 2010]. The reality of fluid flow within a subsurface rock fracture is shown in Figure 1-4, where the fluid flow along the preferential flow path is explicitly visualized. The occurrence of channeling flows within fractures was examined through field investigations at the Stripe mine in Sweden [*Abelin et al.*, 1985; *Tsang and Neretnieks*, 1998]. Moreover, evidence of a channeling flow can be easily found through field observation as a discrete outflow of groundwater from a continuous fracture (Figure 1-5). Therefore, in the next generation of fracture network model simulator, for better understanding of fluid flow and transport phenomena, explicit consideration of the formation of 3-D preferential flow paths (i.e., 3-D channeling flow) in fracture networks is desirable. To achieve these purposes, rock fractures should be modeled by pairs of rough fracture surfaces having heterogeneous aperture distributions in the next generation of simulator.

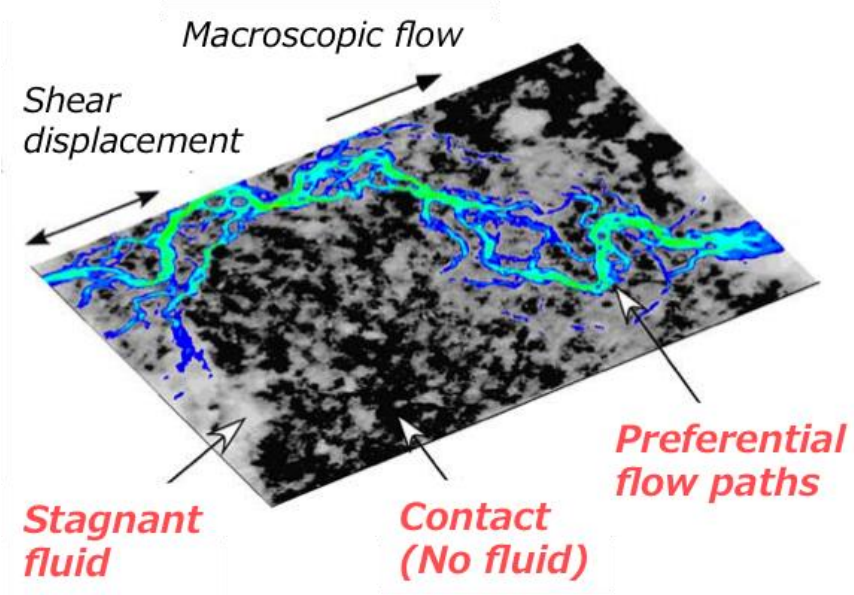

Figure 1-4. Schematic illustration of the reality of fluid flow within a subsurface rock fracture. Preferential flow paths are formed within a heterogeneous aperture distribution of rock fracture (modified after *Watanabe et al.* (2009)).

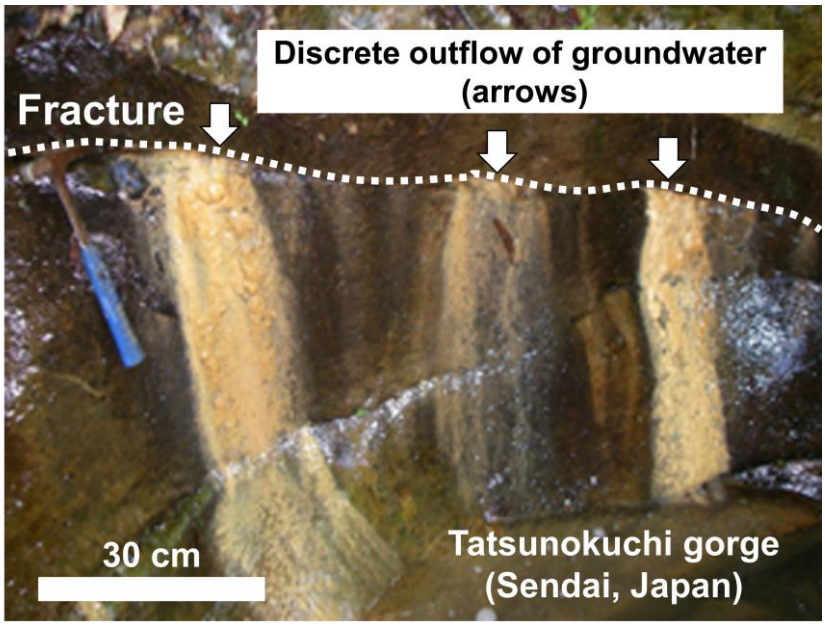

Figure 1-5. Channeling flow seen as discrete outflow of ground water from a continuous fracture at the Tatsunokuchi gorge in Sendai City, Japan.

For the fracture aperture distribution and resulting fluid flow characteristics, such as the permeability and flow paths, these parameters are known to be constrained by fracture surface

topography, shear displacement, and confining stress [*Tsang and Witherspoon*, 1981; *Durham and Bonner*, 1994; *Durham*, 1997; *Yeo et al.*, 1998; *Esaki et al.*, 1999; *Chen et al.*, 2000; *Plouraboué et al.*, 2000; *Pyrak-Nolte and Morris*, 2000; *Auradou et al.*, 2005 and 2006; *Koyama et al.*, 2008; *Walsh et al.*, 2008; *Watanabe et al.*, 2008 and 2009]. Furthermore, these characteristics are known to vary with time as a result of mechanical and chemical influences, such as the pressure solution at contacting asperities or dissolution at noncontacting asperities [*Durham et al.*, 2001; *Yasuhara et al.*, 2006; *Ishibashi et al.*, 2013; *Elkhoury et al.*, 2013]. On the other hand, it remains unclear how the fracture aperture distribution and resulting fluid flow characteristics are constrained by the fracture scale. Considering that an actual fractured reservoir is constructed by a number of fractures with various scales, such findings are critically important in simulating fluid flow within an actual fractured reservoir.

Based on the fluid flow experiments and field investigations, *Witherspoon et al*. (1979) and *Raven and Gale* (1985) reported that the scale of the rock fracture influences on its permeability for the first time, although their results are inconsistent. *Matsuki et al*. (2006), on this, suggested that experimentally determining the scale dependency for the permeability of a fracture is difficult because individual samples have unique aperture layouts. Therefore, they investigated the scale dependencies in the aperture and the permeability of fractures both with and without shear displacement using numerically created fractures. Their results have significant advantages in that their investigations were systematic. However, the effect of confining stress on the fracture flow characteristics is not strictly introduced in their evaluation because they assumed constant mean apertures. Furthermore, they never compared the aperture and the permeability with those for actual rock fractures. Thus, predicting the flow characteristics of rock fractures remains difficult, and a novel predicting method of channeling flow through subsurface rock fractures beyond laboratory scale is desirable to be developed.

1.3. Objectives and thesis structure

Objectives of this study are developing a novel method to analyze and predict three dimensional (3-D) channeling flow in actual fractured reservoirs and clarifying the characteristics and impacts of the 3-D channeling flow. In this study, both experimental and

numerical approaches are taken to achieve the objective.

"GeoFlow: A novel model simulator for prediction of the three dimensional channeling flow in a rock fracture network" is presented in Chapter Ⅱ. A novel DFN model simulator for analyzing 3-D channeling flow within rock fracture networks is developed. This simulator is subsequently applied to analyze fluid flow through a cylindrical granite sample containing two intersecting fractures, and it is clarified that the 3-D channeling flow is necessary to be considered in laboratory-scale.

"Beyond-laboratory-scale prediction for channeling flows through subsurface rock" is presented in Chapter Ⅲ. On the basis of laboratory investigations, insight into the scale dependencies of the aperture distribution and the resulting fluid flow characteristics for rock fractures under confining stress is obtained. Based on the investigations, a novel method to predict fracture aperture distributions beyond the laboratory scale is developed.

"Universal modeling of fluid flow characteristics through subsurface rock fractures" is presented in Chapter Ⅳ. Using the developed method to predict fracture aperture distributions beyond laboratory scale, aperture distributions and fluid flows are numerically determined for the subsurface rock fractures with various combinations of fracture scale and shear displacement. Through evaluating the aperture distributions and fluid flows, fluid flow characteristics of the rock fractures are revealed for a wide range of conditions for fracture scale, shear displacement, and confining stress.

"Modeling of three dimensional channeling flow in a fractured reservoir with GeoFlow" is presented in Chapter Ⅴ. Realistic DFN models, where heterogeneous aperture distributions are given for individual fractures depending on their scale and shear displacement under confining stress, are created for an actual fractured reservoir. By simulating fluid flows within the reservoir with GeoFlow, the characteristics and impact of 3-D channeling flow in fractured reservoirs are revealed.

Conclusions and some recommendations for future research are shown in Chapter Ⅵ.

Chapter Ⅱ

GeoFlow: A novel model simulator for prediction of the three dimensional channeling flow in a rock fracture network

2.1. Introduction

As described in Chapter Ⅰ, in the Earth's crust, rock fractures are recognized as the predominant pathways of resources and hazardous materials, such as groundwater, hydrocarbons, geothermal fluids, and the high-level nuclear wastes. This is because rock fractures usually have much greater permeability than the matrix permeability [*Watanabe et al.*, 2009]. According to the previous studies, a fluid flow within a fracture network is generally characterized by formation of three dimensional preferential flow paths (i.e. 3-D channeling flow) [*Abelin et al*., 1985; *Tsang and Neretnieks*, 1998; *Johnson et al.*, 2006]. Therefore, occurrence of 3-D channeling flow should be addressed in evaluating fluid flow characteristics for fracture networks. However, to date there are no practical simulators which can explicitly consider the formation of the 3-D preferential flow paths within fracture networks.

In order to consider the formation of the 3-D preferential flow paths within fracture networks, GeoFlow, a novel discrete fracture network (DFN) model simulator, is developed. In this simulator, rock fractures are modeled by pairs of rough fracture surfaces having heterogeneous aperture distributions, rather than pairs of parallels smooth plates with unique apertures. Although numerical methods for a 3-D fluid flow simulation in a network of fractures with aperture distributions have been reported [*Morris et al.*, 1999, *Stockman et al.*, 2001, *Johnson et al.*, 2006], these methods focus only on fracture flow and so would not be suitable for DFN model simulations on natural fractured rocks with non-zero matrix permeabilities. In contrast, one novel aspect of GeoFlow is the combination of fractures having aperture distributions with a matrix, and this aspect was reached by applying hybrid DFN and continuum model.

In this chapter, we first describe a fluid flow experiment on a cylindrical granite sample containing two intersecting fractures to demonstrate that 3-D channeling flow must be considered to interpret fluid flow even in the simplest fracture network. A fluid flow simulation

of the sample by GeoFlow is then conducted, and the potential of GeoFlow to predict 3-D channeling flows in fracture networks is demonstrated.

2.2. Methods

2.2.1. Multiple-fracture flow experiment

The fluid flow experiment is conducted using a cylindrical granite sample (diameter: 100 mm, length: 147 mm) having two intersecting tensile fractures (Fractures A and B) (Figure 2-1). A multiple-fracture sample (Figure 2-1a) is prepared as follows. First, two tensile fractures are sequentially induced within a cube of Inada granite, quarried in Ibaraki, Japan. The fractured granite is then fixed with mortar so that the fractures are mated fractures. The granite is then cored and cut to the prescribed dimensions. Before the experiment, the surface topography of the entire fracture plane is measured in a 0.25-mm square grid system using the Laser-scanning equipment reported in *Watanabe et al*. [2008] to determine the aperture distributions of Fractures A and B in the fluid flow simulation by GeoFlow.

A custom experimental system (Figure 2-1b) is used to obtain data for comparison with the results obtained by GeoFlow. The experimental system is equipped with a water pump, a pressure gauge, and a confining pressure vessel similar to that reported by *Watanabe et al.* [2008]. The confining pressure vessel enables the evaluation of uneven outflow from the sample at a prescribed confining pressure. Using the water pump, room temperature water is injected into the top of the confining pressure vessel through a single inlet port. Water flows through the sample and out of the bottom of the confining pressure vessel through five outlet ports (Ports 1 through 5), which are isolated from each other by a port separator of stainless steel. The port separator is attached with a silicone rubber sealant. Note that the sample is hydraulically saturated in advance by injecting water from the bottom through Ports 1 through 4, and that Port 5 is used only to confirm the isolation of the ports. The pressure gauge is used to measure the hydraulic pressure at the inlet side (the atmospheric pressure at the outlet side), where the outlet tube is placed at the same elevation as the inlet tube to cancel the effect of gravity and maintain the saturated condition.

The present experiment is conducted at a constant confining pressure of 36 MPa and a

hydraulic pressure difference of 0.6 MPa (Figure 2-2). The confining pressure resulted in normal stresses of 35 MPa and 30 MPa for Fractures A and B, respectively. During the experiment, flow rates from the outlet ports (Ports 1 through 4) are measured and analyzed. Ports 1 and 2 are assigned to Fracture A, and Ports 3 and 4 are assigned to Fracture B. Based on the confirmation of the total flow rate (sum of flow rates from all ports) being proportional to the hydraulic pressure difference of $\leq$ 0.6 MPa for the sample at the given confining pressure, although a deviation from linearity occurred at > 0.6 MPa probably due to the fracture opening as a result of the higher pore pressure, a GeoFlow fluid flow simulation based on Darcy's law would be appropriate for the present experiment.

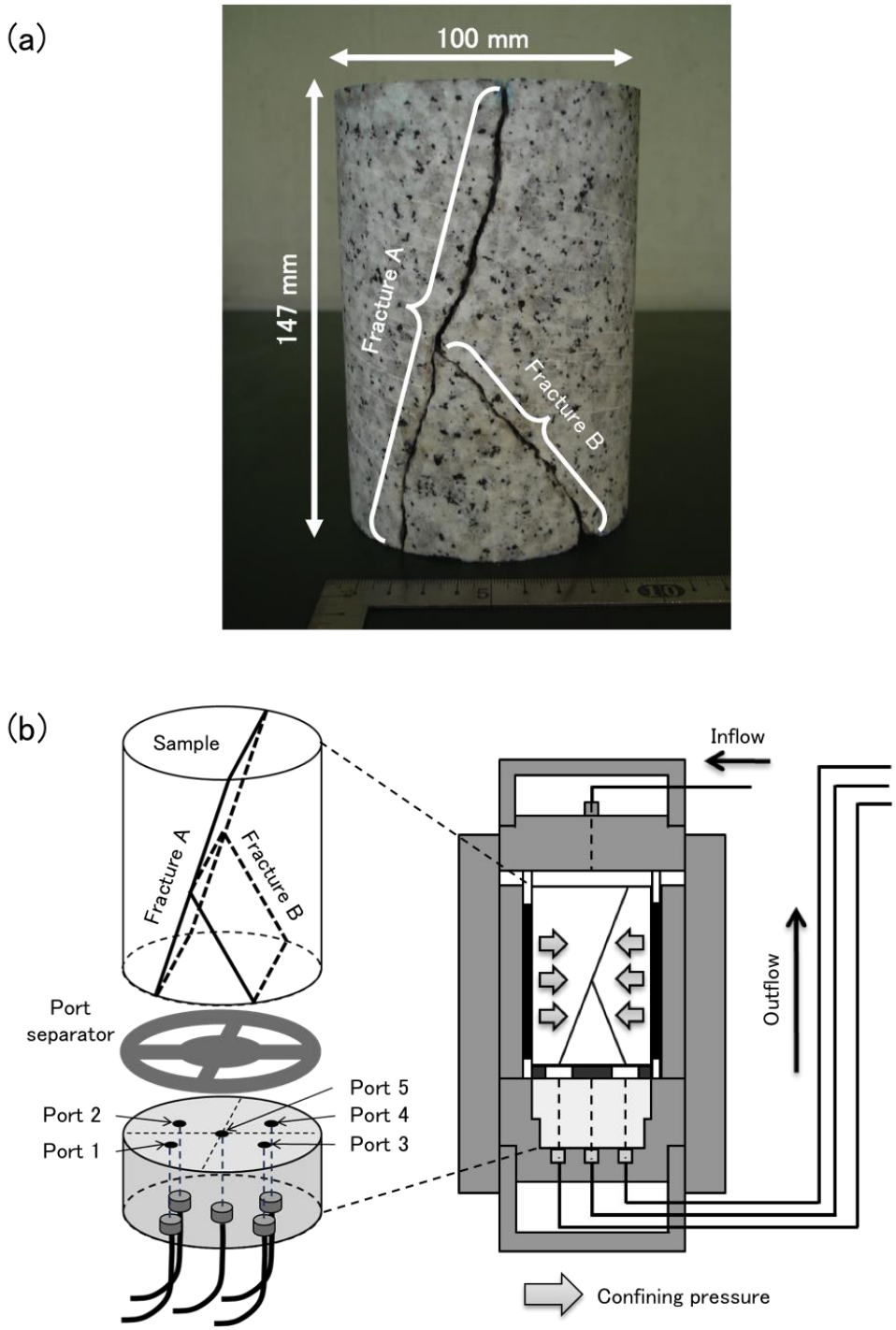

Figure 2-1. (a) Multiple-fracture sample containing two intersecting mated tensile fractures (Fractures A and B), and (b) the experimental setup for the evaluation of uneven fluid flow within the sample under confining pressure.

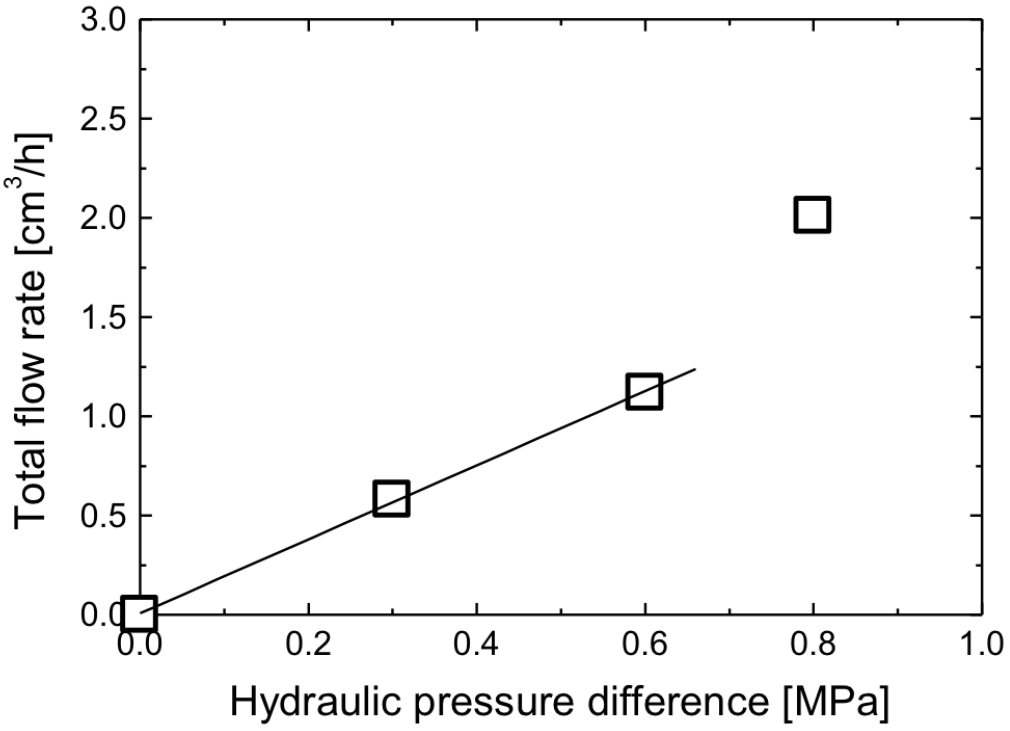

Figure 2-2. Relationship between the total flow rate and hydraulic pressure difference for the multiple-fracture sample at 36 MPa. The linear curve shows the result of the least squares regression at hydraulic pressures of ≤ 0.6 MPa.

2.2.2. GeoFlow simulation

A GeoFlow fluid flow simulation (GeoFlow simulation) involves the following two main steps (Figure 2-3). A fracture network is first created in a 3-D matrix by mapping 2-D fractures with aperture distributions. The Darcy flow through a matrix element interface is then calculated for an equivalent permeability continuum reflecting contributions of both the matrix and fracture permeabilities.

The fracture is a rectangular plane having dimensions of $L_i \times L_j$ in the *i*-*j* coordinate system, whereas the matrix is a rectangular parallelepiped space having dimensions of $L_x \times L_y \times L_z$ in the *x*-*y*-*z* coordinate system (Figure 2-3a). The fracture is divided into $N_i \times N_j$ elements, where the fracture element is a rectangular cell having dimensions of $L_i/N_i \times L_j/N_j$, and each cell has an

aperture value, $a(i, j)$ (Figure 2-3a). The aperture value of each cell is determined based on the results of surface topography measurement in the present study, as described later. However, the aperture determination method is not limited to the present method. The fracture is mapped in the *x*-*y*-*z* coordinate system by determining the coordinates of the centroid and the direction of a specific pair of normal and tangent vectors for the fracture plane.

The matrix containing fractures is divided into $N_x \times N_y \times N_z$ elements so that the matrix element is a rectangular parallelepiped cell having dimensions of $L_x/N_x \times L_y/N_y \times L_z/N_z$ (Figure 2-3b), and a steady-state laminar flow of a viscous, incompressible fluid is calculated for an equivalent permeability continuum. In preliminary study, it is empirically confirmed that the ratio of the matrix element to the fracture element should be less than two, so that fluid flow through a specific fracture simulated by a 2-D Reynolds equation can be reproduced in a 3-D GeoFlow simulation with preserving characteristics of the original aperture distribution. For the equivalent permeability continuum reflecting contributions of both the matrix and fracture permeabilities, the fluid flow model based on Darcy's law is as follows:

$$\frac{\partial}{\partial x}\left(\frac{A_x k_x}{\mu}\frac{\partial P}{\partial x}\right)+\frac{\partial}{\partial y}\left(\frac{A_y k_y}{\mu}\frac{\partial P}{\partial y}\right)+\frac{\partial}{\partial z}\left(\frac{A_z k_z}{\mu}\frac{\partial P}{\partial z}\right)=0, \qquad (2\text{-}1)$$

where A_x, A_y, and A_z are the cross-sectional areas, k_x, k_y, and k_z are the permeabilities, in different directions, and μ and P are the viscosity and pressure of the fluid, respectively. In order to determine the Darcy flow through the matrix element interface, a finite difference form of Eq. (2-1) is solved under given boundary conditions with the incomplete Cholesky-conjugate gradient (ICCG) method, in which the use of the product, $A_i k_i$ (i=x, y, z), represented by the following equation, characterizes the GeoFlow simulation:

$$A_i k_i = \sum_n \frac{w_{f,n} \cdot a_{f,n}^3}{12} + A_m k_m \quad (i = x, y, z), \qquad (2\text{-}2)$$

where $w_{f,n}$ and $a_{f,n}$ are the width and aperture, respectively, of the nth fracture element intersecting the matrix element interface, and A_m and k_m are the area and permeability,

respectively, of the matrix part (Figure 3-3b). As expressed by Eq. (2-2), equivalent permeabilities are determined at all matrix element interfaces in GeoFlow simulation (Figure 2-3b). Fundamental concept of this conversion technique for equivalent permeability was previously reported in *Jing et al.* [2000], and quite different from the concept of *Snow* [1969] or *Long et al.* [1982] which determines single isotropic equivalent permeabilities for the matrix elements. The first term of the right side of Eq. 2-2 is based on the local cubic law assumption [*Ge*, 1997; *Oron and Berkowitz*, 1998; *Brush and Thomson*, 2003; *Konzuk and Kueper*, 2004].

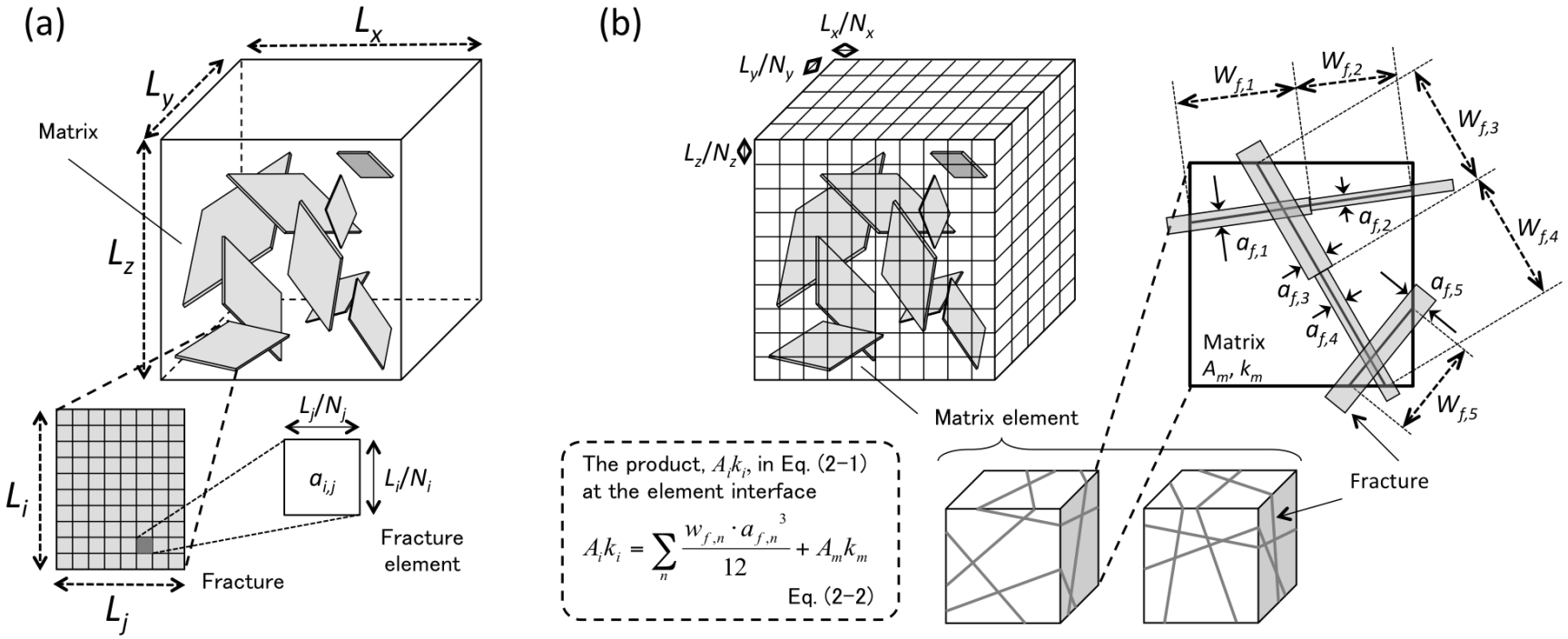

Figure 2-3. (a) 3-D matrix containing a network of the 2-D fractures with aperture distributions, (b) which is divided into the matrix elements and is finally converted into the equivalent permeability continuum, in which the Darcy flow through the element interface is calculated.

A fracture network consisting of two fractures, which have aperture distributions of Fractures A and B under the given stress conditions, is created in the matrix of 140 mm × 140 mm × 140 mm by imitating the spatial configuration of fractures in the sample. The aperture distributions are determined using the surface topography data for Fractures A and B by closing two opposite surfaces so that the total flow rate in the GeoFlow simulation is approximately equal to the experimental value. Aperture determination is based on *Watanabe et al.* [2008], where the fracture closure under normal stress is simulated simply by uniform reduction of all apertures in conjunction with replacing overlapping asperities (negative apertures) with zero-apertures. Ideally, it is desirable to determine the aperture distribution for each fracture using the surface topography and permeability data for that fracture. However, the permeability of each fracture could not be measured separately in the present experiment. Therefore, the two fractures are assumed to have the same permeabilities (2.9×10^{-13} m^2) or hydraulic apertures (1.87 μm) at the given normal stresses because the difference in the applied normal stress between Fractures A and B is small (35 MPa for Fracture A and 30 MPa for Fracture B). Since the surface topography is measured in the 0.25-mm square grid system, the fracture element have dimensions of 0.25 mm × 0.25 mm. The matrix is divided into matrix elements of 280 × 280 × 280 so that the dimensions of the matrix element are 0.5 mm × 0.5 mm × 0.5 mm. In order to simulate the fluid flow experiment, the unidirectional water flow is analyzed by GeoFlow. Matrix permeability, constant viscosity, and hydraulic pressure difference are respectively set as 1×10^{-19} m^2, 1×10^{-3} Pa·s, and 0.6 MPa. Note that the matrix permeability is based on the permeability of Inada granite [*Takahashi et al., 1990*]. The boundary conditions for the analysis are shown in Figure 2-4.

2.3. Results and Discussion

The fluid flow experiment provides flow rates of 0.13 cm^3/h for Port 1, 0.38 cm^3/h for Port 2, 0.05 cm^3/h for Port 3, and 0.58 cm^3/h for Port 4 (total flow rate: 1.14 cm^3/h). In the experiment, Ports 1 and 2 (or Ports 3 and 4) are both assigned to Fracture A (or Fracture B). However, the flow rates differ significantly between the two ports. In the case of Fracture A, the flow rate for Port 2 is approximately three times greater than that for Port 1. Moreover, in case

of Fracture B, the difference in the flow rate exceeds one order of magnitude, indicating a considerably uneven flow within the sample.

Calculating the flow rate ratio as a flow rate for the port over the total flow rate, the flow rate ratio is 11% for Port 1, 33% for Port 2, 5% for Port 3, and 51% of Port 4 (see Figure 2-5). Surprisingly, considering the total flow rate in the fractured rock sample, the flow rate ratio for Port 3 is almost negligible, whereas the flow rate ratio for Port 4, assigned to an identical fracture, accounts for approximately half of the total flow rate. This is the most remarkable experimental finding.

The experimental results indicate 3-D channeling flow, which is not predicted by the conventional DFN model simulations but should be predicted to clarify fluid migration especially in the field of reservoir engineering. Reservoir engineers have encountered a large difference in productivity between wells when developing fractured reservoirs. *Tamagawa et al*. [2012] attempted to determine the reason for a three-order-of-magnitude difference in productivity between two wells in the Yufutsu oil/gas field in Hokkaido, Japan. However, it was not possible to reproduce the large difference in productivity by the conventional DFN model simulation, despite a reliable fracture network model based on seismic data, well logging, acoustic emission, and stress measurements. Considering the nature of the conventional DFN simulation, which ignores the 3-D channeling flow in a fracture network, this may be a logical result. In order to address this concern, we first investigate 3-D channeling flow in lab-scaled fracture networks, as described herein.

The GeoFlow simulation clearly exhibits 3-D channeling flow in the equivalent permeability continuum of the multiple-fracture sample, which has an equivalent permeability distribution generated by the combination of the aperture distributions of Fractures A and B at the given stresses with the matrix permeability (Figure 2-4). The average permeability at each element in the equivalent permeability continuum is calculated using k_i in Eq. (2) of the six element interfaces (A_i is the area of those element interfaces), and elements having a permeability of $\geq 1\times10^{-14}$ m^2 are shown in different colors depending on the value (Figure 2-4a). Uncolored points are elements whose interfaces have no fracture or small-aperture fracture(s), therefore their permeabilities are less than 1×10^{-14} m^2. The gray points indicate the locations of

two fractures. Since the topographies of two opposite fracture surfaces are not identical, the aperture is not uniform throughout the fracture plane, but rather an aperture distribution and corresponding permeability distribution is produced in each fracture plane. The present GeoFlow simulation for the equivalent permeability continuum provides a flow rate distribution in a unidirectional flow, from top to bottom in the figure. The flow rate at each element is normalized by the maximum value for all of the flow rates. Figure 2-4b shows the elements that have a normalized flow rate of ≥ 0.001 as different colors depending on the value, while remarkable localization of the fluid flow in the fracture network is visualized. Uncolored points are elements having flow rates of < 0.001, and gray points show the locations of two fractures. Since the fracture part has much higher permeability than the matrix part (Figure 2-4a), only the fracture part conducted the fluid flow, and preferential flow paths are formed due to the permeability distribution in the fracture network. Even visual observation reveals that the flow rate for Port 4 is dominant, as observed in the fluid flow experiment.

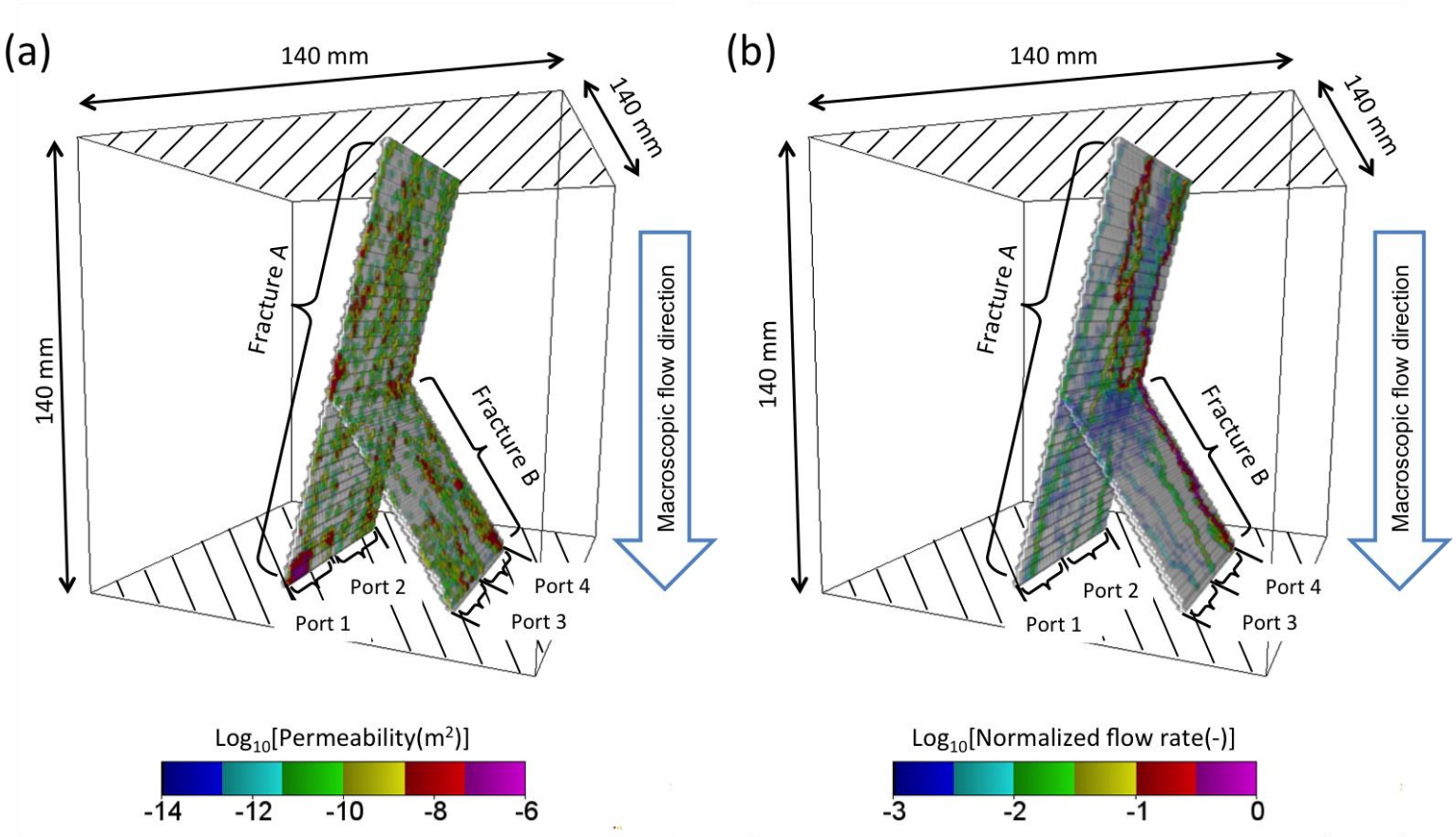

Figure 2-4. (a) Equivalent permeability continuum model of the multiple-fracture sample at a confining pressure of 36 MPa, as represented by a permeability distribution, and (b) the fluid flow model of the sample, as represented by a distribution of flow rate for the unidirectional fluid flow from top to bottom (hatched boundaries: constant hydraulic pressure, other boundaries: non-flow), as derived by the GeoFlow simulation.

The GeoFlow simulation provides flow rates of 0.07 cm^3/h for Port 1, 0.05 cm^3/h for Port 2, 0.02 cm^3/h for Port 3, and 0.87 cm^3/h for Port 4 (total flow rate: 1.01 cm^3/h). The flow rate ratio is 7% for Port 1, 5% for Port 2, 2% for Port 3, and 86% for Port 4 (Figure 2-5). As shown in Figure 5, it is possible to reproduce the most remarkable experimental finding that the flow rate ratio of Port 4 for Fracture B is dominant, whereas the flow rate ratio of Port 3 for the identical fracture is considerably small. However, the numerical results don't exactly match the experimental results. This may have been caused by a difficulty in the aperture determination. Since the present method involves dismantling of the sample, the apertures within the sample, particularly at the intersection of the fractures, cannot be exactly the same as the real values. A more accurate aperture determination would be possible using a method that does not involve dismantling the sample, which is beyond the scope of the present study. Therefore, the flow paths predicted by the present GeoFlow simulation cannot be exactly the same as the real flow paths, and, consequently, the present level of disagreement between the numerical and experimental results is reasonable. Nevertheless, despite the simplicity, the most remarkable experimental finding can be reproduced, demonstrating that the GeoFlow has significant potential to predict 3-D channeling flow in a fracture network.

As described herein, GeoFlow allows novel techniques for the investigation of fluid flows, especially in lab-scaled fracture networks. Based on previously reported aperture distribution data, the investigation of fluid flows in various types of fracture network can be conducted systematically with no technical difficulty. Moreover, using the aperture distribution determined by X-ray CT for naturally fractured core samples [*Watanabe et al*., 2011] should be effective when considering an application of GeoFlow simulation in a specific field. However, the final goal in GeoFlow studies is the investigation of fluid flows in field-scale fracture networks. For this purpose, the aperture distributions of fractures of various sizes must be predicted from information of lab-scale fractures. Moreover, even if the aperture distributions can be predicted, an up-scaling method is necessary in creating an equivalent permeability continuum for field-scale investigations.

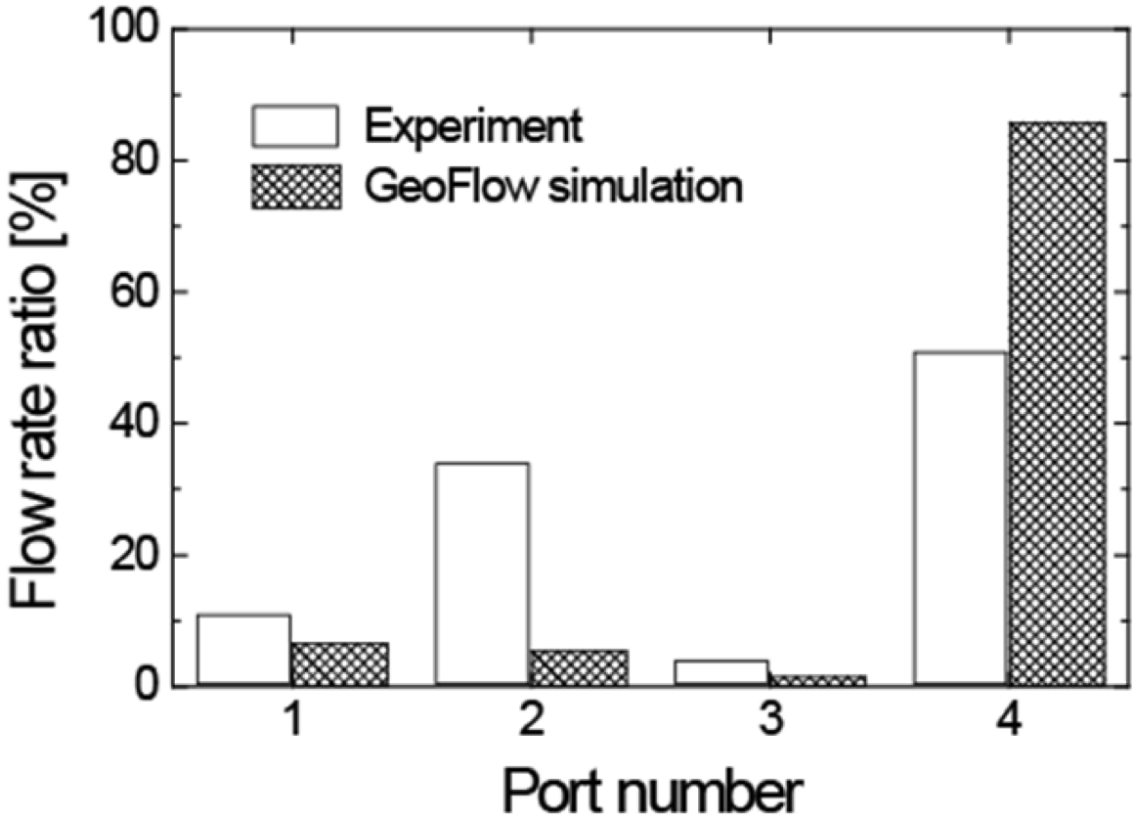

Figure 2-5. Comparison of the experimentally observed flow rate ratios for the ports and the numerical prediction by GeoFlow simulation for the fluid flow through the multiple-fracture sample.

2.4. Conclusions

Since fractures having heterogeneous aperture distributions act as predominant pathways in rocks, 3-D channeling flows in fracture networks should be investigated to better understand fluid migration. As demonstrated by the present fluid flow experiment, fluid flows in fracture networks are characterized by considerably uneven fluid flows, which are cannot be predicted by existing model simulators. In contrast to other model simulators, as demonstrated herein, the GeoFlow discrete fracture network model simulator has significant potential to predict a 3-D channeling flow in a fracture network. GeoFlow will provide a new way to investigate fluid flow in a fracture network.

Chapter Ⅲ

Beyond-laboratory-scale prediction for channeling flows through subsurface rock fractures

3.1. Introduction

In Chapter Ⅱ, based on the fluid flow experiment, it is revealed that the reality of fluid flow through rock fracture network is 3-D channeling flow. 3-D channeling flow is necessary to be considered in an actual fractured reservoir. To analyze the 3-D channeling flow, a novel discrete fracture network (DFN) model simulator, GeoFlow, is developed and its potential is revealed.

In order to model an actual fractured reservoir with DFN, a prediction method of heterogeneous aperture distribution and resulting fluid flow of fractures beyond-laboratory-scale is necessary to be developed. This is because an actual fractured reservoir is constructed by a number of fractures with various scales. However, it is not completely revealed that how the fracture aperture distribution and resulting fluid flow characteristics are constrained by the fracture scale [*Witherspoon et al.*, 1979; *Raven and Gale*, 1985; *Matsuki et al.*, 2006], and predicting the flow characteristics of rock fractures remains difficult.

Thus, in this chapter, insight into the scale dependencies of the aperture distribution and the resulting fluid flow characteristics for rock fractures is obtained under confining stress on the basis of laboratory investigations. A novel method by which to predict fracture aperture distributions beyond the laboratory scale is developed on the evaluation in the present chapter. This method is verified through the reproduction of the results obtained in the laboratory investigation, as well as the maximum aperture-fracture length relations, which have been reported in the literature, for natural fractures. Furthermore, conceivable scale dependencies of aperture distributions and fluid flow characteristics of subsurface fractures, such as joints and faults, are suggested.

3.2. Methods

3.2.1. Evaluation of fracture aperture distributions and fluid flows on the laboratory scale

The fracture aperture distribution under confining stress and the fluid flow through the aperture distributions are determined using data of the fracture surface topography and permeability, as described in the literature [*Watanabe et al.*, 2008 and 2009]. Measurements of the fracture surface topography and permeability are, therefore, conducted on single fractures for scales of 0.05 m × 0.075 m, 0.1 m × 0.15 m, and 0.2 m × 0.3 m. These fractures are contained in cylindrical samples of Inada medium-grained granite (Ibaraki Prefecture, Japan), and the diameters and lengths of these samples are equivalent to the short and long side lengths, respectively, of the rectangular fractures (Figure 3-1). The fracture is a tensile fracture induced by a wedge and has either no shear displacement or a shear displacement of 5 mm in the radial direction. The shear displacement is created by the lateral offset of initially well-mated fracture surfaces that are created in a cubic granite block and is maintained by fixing the fractured granite block with mortar during coring. Since both fractures with and without shear displacement are prepared for each fracture scale, the total number of rock samples is six. The surface topography is measured for each fracture before measuring the permeability under confining stress. Two-dimensional distributions of surface height are measured in a 0.25-mm square grid system with a laser profilometer, which has a height resolution of 1 μm and a positioning accuracy of 20 μm. The data for surface topographies are used as input data for the numerical determination of fracture aperture distributions and the fluid flows within the fractures by means of the permeability matching method described later herein.

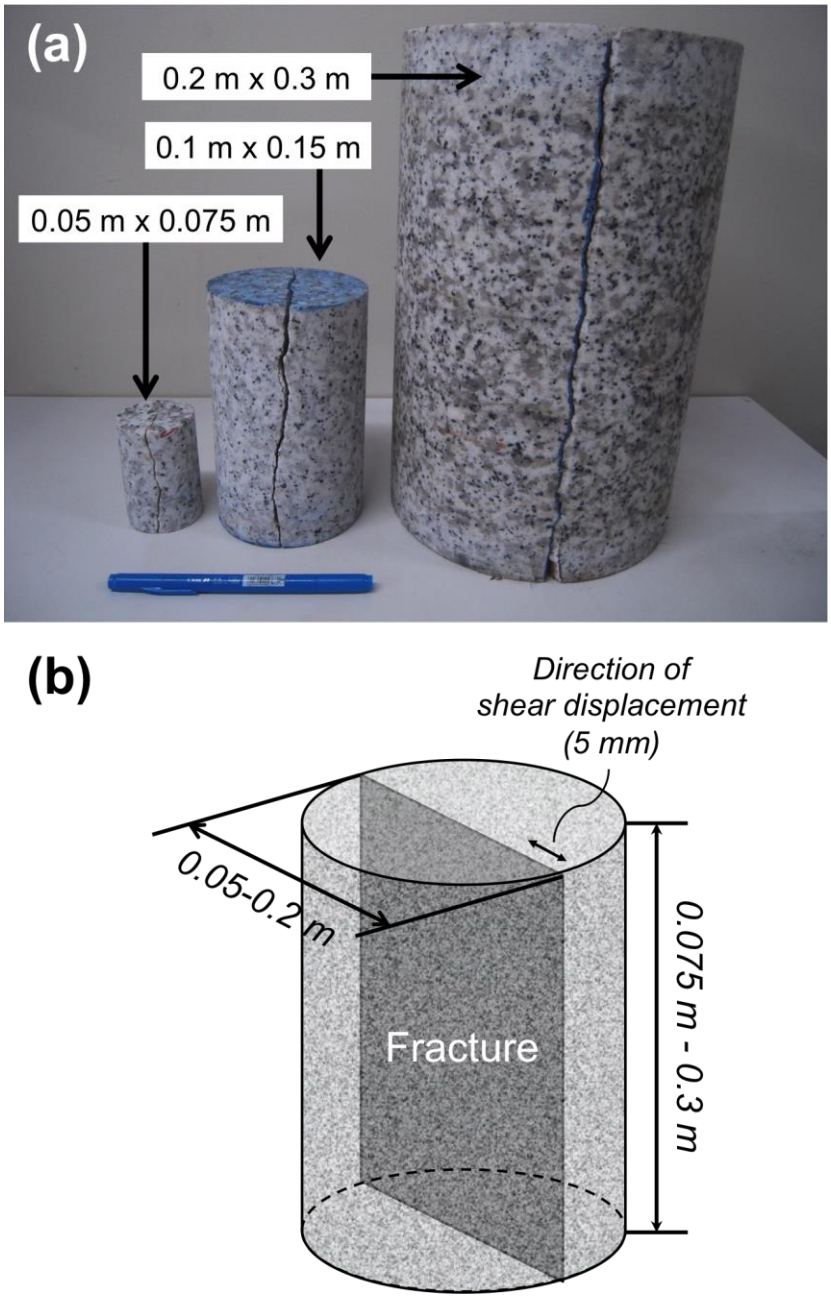

Figure 3-1. Cylindrical granite samples containing single tensile fractures of different sizes having either (a) no shear displacement or (b) a shear displacement of 5 mm in the radial direction.

The permeability for each fracture is measured at confining stresses of 10, 20, and 30 MPa through a unidirectional fluid flow experiment along the sample axis at room temperature (Figure 3-2). The rubber-sleeved fractured sample is subjected to confining stress (hydrostatic

pressure by water) in a pressure vessel. While distilled water flows from the bottom to the top of the sample at a constant flow rate, a corresponding differential pressure between the inlet and the outlet is measured by a differential pressure gauge. The flow rate is controlled by a water pump and confirmed by measuring the weight of the effluent using an electronic balance. Low pore pressures of less than 5% of the given confining stress are used so that the effective confining stresses do not differ significantly from the confining stress values. Since linear relationships between the flow rate and the differential pressure are observed for all given conditions, the fracture permeability is determined for the sample with a negligible matrix permeability of from 10^{-19} to 10^{-18} m^2 based on the cubic law [*Witherspoon et al.*, 1980; *Tsang and Witherspoon*, 1981]:

$$k = \frac{e_h^2}{12}, \tag{3-1}$$

where k is the fracture permeability, and e_h is the hydraulic aperture, which is described as follows:

$$e_h = \left(-\frac{12\mu L Q}{W \Delta P} \right)^{1/3}, \tag{3-2}$$

where Q is the flow rate, ΔP is the differential pressure, μ is the viscosity of the fluid, and L and W are the long and short side lengths, respectively, of the fracture.

Based on the measurements of the fracture surface topography and permeability, 2-D aperture distributions of the fractures under the confining stresses are numerically determined by computer through a permeability matching method, in which the pairs of fracture surfaces are in contact with each other, so that the aperture distributions have the experimentally determined fracture permeabilities. In this permeability matching, an aperture distribution with at least a single contact point is first created in the 0.25-mm square grid system, and the apertures are decreased to simulate fracture closure due to confining stress. The apertures are local separations between two opposite fracture surfaces in the direction normal to their mean planes. In decreasing the apertures, the two fracture surfaces become close together and some asperities are overlapped. Overlapping asperities are assumed to be contacting asperities (i.e., regions of zero aperture), and fracture surface deformations are not considered. [*Zimmerman et al.*, 1992; *Matsuki et al.*, 2006]. The permeability of the aperture distribution is evaluated by

simulating a unidirectional fluid flow 2-D (*x*-*y*) field with the Reynolds equation for a steady-state laminar flow of a viscous and incompressible fluid [*Brown*, 1987b; *Ge*, 1997; *Oron and Berkowitz*, 1998; *Yeo et al.*, 1998; *Sausse*, 2002; *Brush and Thomson*, 2003; *Jaeger et al.*, 2007]:

$$\frac{\partial}{\partial x}\left(e^3 \frac{\partial P}{\partial x}\right)+\frac{\partial}{\partial y}\left(e^3 \frac{\partial P}{\partial y}\right)=0, \tag{3-3}$$

where e is the aperture, and P is the pressure of the fluid. The Reynolds equation is solved with a finite difference method under the same boundary condition as that in the fluid flow experiment (Figure 3-3). In solving the Reynolds equation, the contacting asperities are replaced with a negligibly small nonzero aperture of 1 μm because the pressure cannot be defined at zero aperture. Since the fluid flow simulation mimics the fluid flow experiment, the permeabilities for the aperture distributions are also determined using Equations (3-1) and (3-2).

As described later herein, all aperture distributions obtained in the present study are characterized by a significant number of contacting asperities (regions of zero aperture) and the skewed distributions of nonzero apertures with long tails, i.e., lognormal-like distributions. Hence, the aperture distributions are evaluated based on the percentages of contacting asperities for all data points (i.e., contact area), the geometric mean, and the geometric standard deviation of the apertures (nonzero values). In evaluating the fluid flows resulting from the fluid flow simulation for the aperture distributions, the area of preferential flow paths in the fracture plane is evaluated because the fluid flows are always characterized as channeling flows.

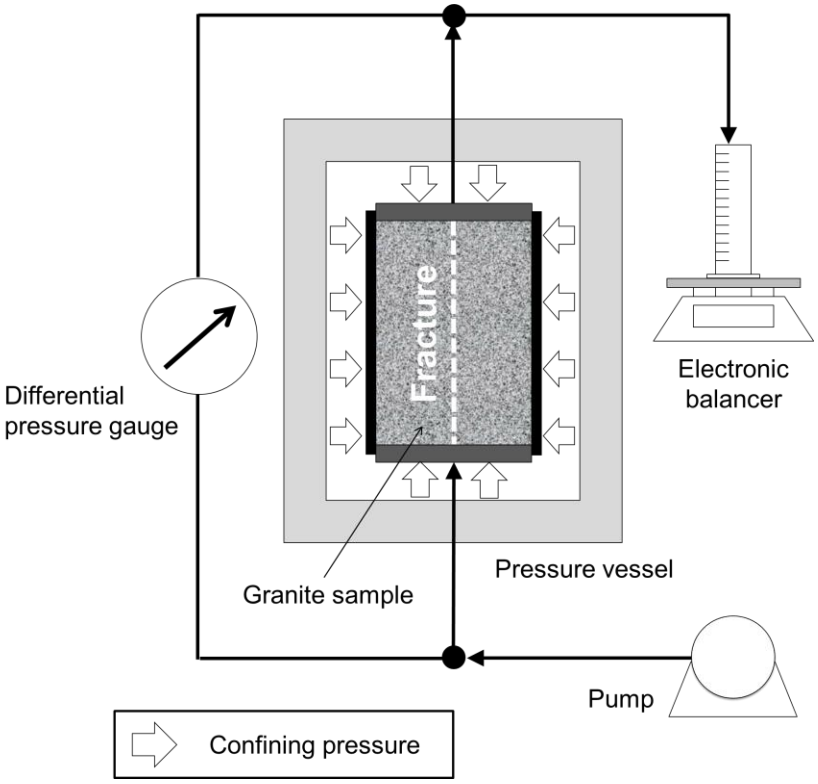

Figure 3-2. Experimental system for permeability measurement of the fracture within the granite sample under confining stress.

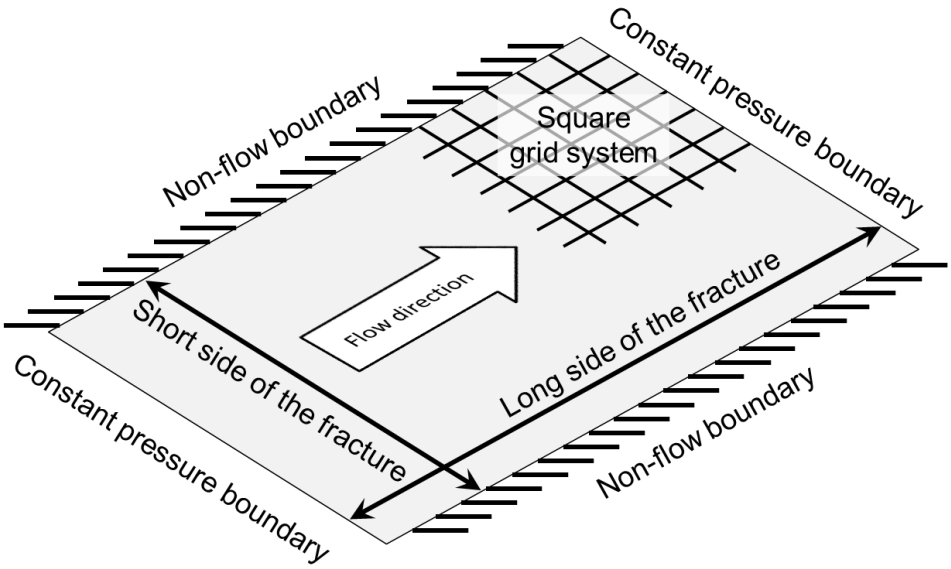

Figure 3-3. Boundary conditions in the unidirectional fluid flow simulation for the fracture aperture distribution created in a 0.25-mm square grid system.

3.2.2. Prediction of fracture aperture distributions and fluid flows beyond laboratory scale

The results of the laboratory investigation inspired the following novel idea of predicting the aperture distributions of beyond laboratory-scale fractures under confining stress. The fractal nature of fracture surface topography is well known [*Brown*, 1987a; *Power et al.*, 1987; *Kumar and Bodvarsson*, 1990; *Power and Durham*, 1997]. Based on the fractal nature, the fracture surface topography can be numerically created [*Brown*, 1995; *Glover et al.*, 1997 and 1998; *Matsuki et al.*, 2006]. Moreover, the fractal nature has been confirmed to be valid for the natural fault roughness from the micro-scale to the continental scale [*Candela et al.*, 2012; *Renard et al.*, 2013]. Consequently, a method used to predict the fracture surface topography beyond the laboratory scale has already been developed. Therefore, the only problem in predicting the aperture distributions of fractures beyond the laboratory scale is how closely the two opposite fracture surfaces are situated under confining stress.

Fracture permeability, mean aperture, or contact area may be used to predict the aperture distribution under confining stress, as long as their scale dependencies are clear and formulated. As described later herein, the scale dependencies of fracture permeability and mean aperture are not clear in the laboratory investigation, which precludes the formulation of their scale dependencies. On the other hand, the scale independency of the contact area has been suggested, and a novel method by which to predict the aperture distributions of fractures from a laboratory scale to a field scale has been developed based on the fractal nature of the fracture surface and the scale-independent contact area. In other words, the aperture distribution of a fracture of any size can be predicted by simply placing the two fractal fracture surfaces in contact so that the fracture has the scale-independent contact area.

The method developed by *Matsuki et al.* [2006] is used in creating a pair of fractal fracture surfaces. Their method is a modification of the method of *Brown* [1995] or *Glover et al.* [1997 and 1998], so that the desired degree of matedness of the two fracture surfaces can be considered. The detail for creating one of two fracture surfaces (upper fracture surface) with the desired fractal dimension and roughness magnitude is explained in Appendix 3-A. Furthermore, the creation of the opposite fracture surface (lower fracture surface) having the desired degree of matedness with the upper fracture surface is explained in detail in Appendix 3-B. Thus, the

required parameters and their values in the present study are described below.

For creating the upper fracture surface, the fractal dimension of the fracture surface, D, and the standard deviation of the fracture surface height, σ_{h0}, along a linear profile of reference length, L_0, are required. In contrast, the mismatch length scale, λ_c, and the ratio of the power spectral density (PSD) of the initial aperture to the PSD of the surface height as a function of spatial frequency, $R(f)$, are required in creating the lower fracture surface. In the present study, the representative parameter values are computed for the fracture surface topographies of the 0.2 m × 0.3 m surface, providing a fractal dimension of 2.3, a standard deviation of 1.3 mm for a reference length of 0.2 m, and a mismatch length scale of 0.7 mm. In addition, the ratio of the PSD of the initial aperture to the PSD of the surface height is approximated by:

$$R(f) = e^{\left\{-6.5\times10^{-3}\cdot(\ln f)^3 - 2.9\times10^{-1}\cdot(\ln f)^2 - 2.2\times10^{-1}\cdot(\ln f) - 5.5\times10^{-1}\right\}}. \quad (3\text{-}4)$$

With these parameter values, pairs of surface topographies of square fractures on a 0.25-mm square grid system are numerically created on a scale of from 0.05 m × 0.05 m to 0.6 m × 0.6 m. Aperture distributions having a scale-independent contact area are then determined and evaluated as described earlier herein. Then, the fluid flows through the predicted aperture distributions are determined and evaluated. The present study essentially provides results for factures beyond the laboratory scale, because even the present maximum fracture size is too large to experimentally determine its aperture distribution and corresponding fluid flow under confining stress.

3.3. Results and Discussion

3.3.1. Channeling flows through heterogeneous aperture distributions of laboratory scale fractures

The results of the permeability measurement for the laboratory scale fractures reveal different changes in permeability (or corresponding hydraulic aperture) with fracture scale between the fractures with and without shear displacement (Figure 3-4). Note that the scales for the rectangular laboratory-scale fractures in the following figures are represented by the shorter side lengths. The fracture permeabilities and corresponding hydraulic apertures are summarized in Table 3-1. For the case of a fracture without shear displacement, the permeability, which has

a lower value at a higher confining stress, increases with the fracture length from 0.05 m to 0.1 m and decreases with the increase in the fracture length from 0.1 m to 0.2 m at all given confining stresses. Consequently, the permeability for the fracture without shear displacement shows no clear scale dependency. On the other hand, the permeability of the fracture with shear displacement, which is much higher than that of the fracture without shear displacement, increases with the fracture length, where no significant change in permeability with confining stress is observed.

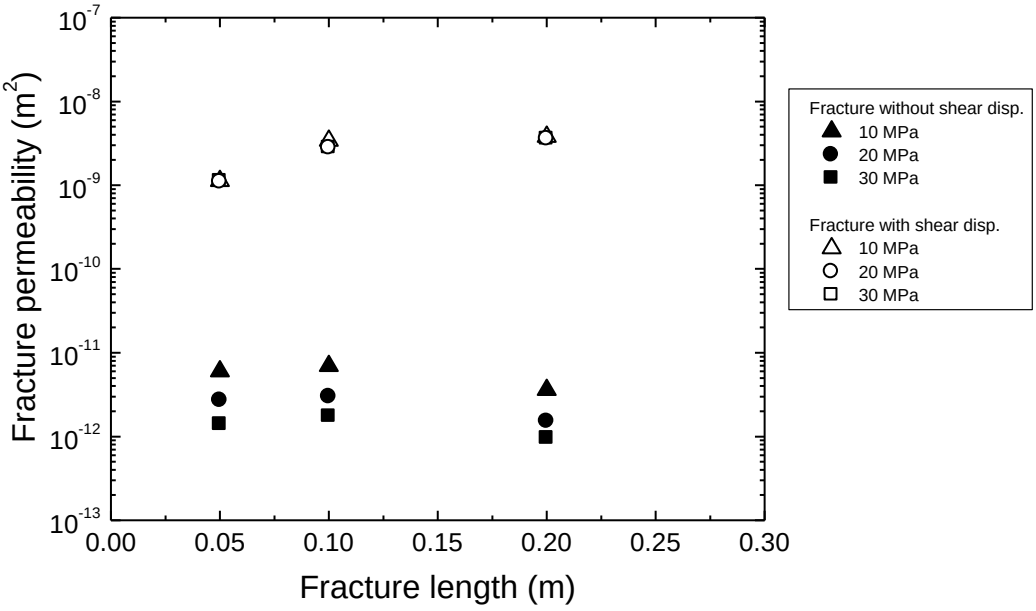

Figure 3-4. Changes in the fracture permeability with fracture length for real laboratory-scale fractures with no shear displacement and with a shear displacement of 5 mm at confining stresses of from 10 to 30 MPa.

Based on the measurements of the fracture permeability and surface topography, the fracture aperture distribution and the corresponding fluid flow are numerically determined for each given condition, indicating heterogeneous aperture distributions and the resulting channeling flows for all conditions. Figure 3-5 shows the representative results for channeling flows through the heterogeneous aperture distributions for the laboratory-scale fractures. In this

figure, the flow rate distributions shown in color scale are superimposed on the corresponding aperture distributions, which are shown in gray scale. In Figure 3-5, the contacting asperities are represented by the minimum apertures of 1 μm for convenience, as described in Section 3.2.1. Moreover, the flow rates in each figure are normalized by the total flow rate for each condition, and flow rates of ≥ 0.01 (1% of the total flow rate) are shown in the figure. The distribution of the colored points therefore maps the dominant flow paths within the aperture distribution, because colorless points have negligibly small flow rates. As shown in the figure, in general, there are a significant number of nonzero aperture points that have a negligible flow rate, which demonstrates the formation of preferential flow paths (i.e., channeling flow).

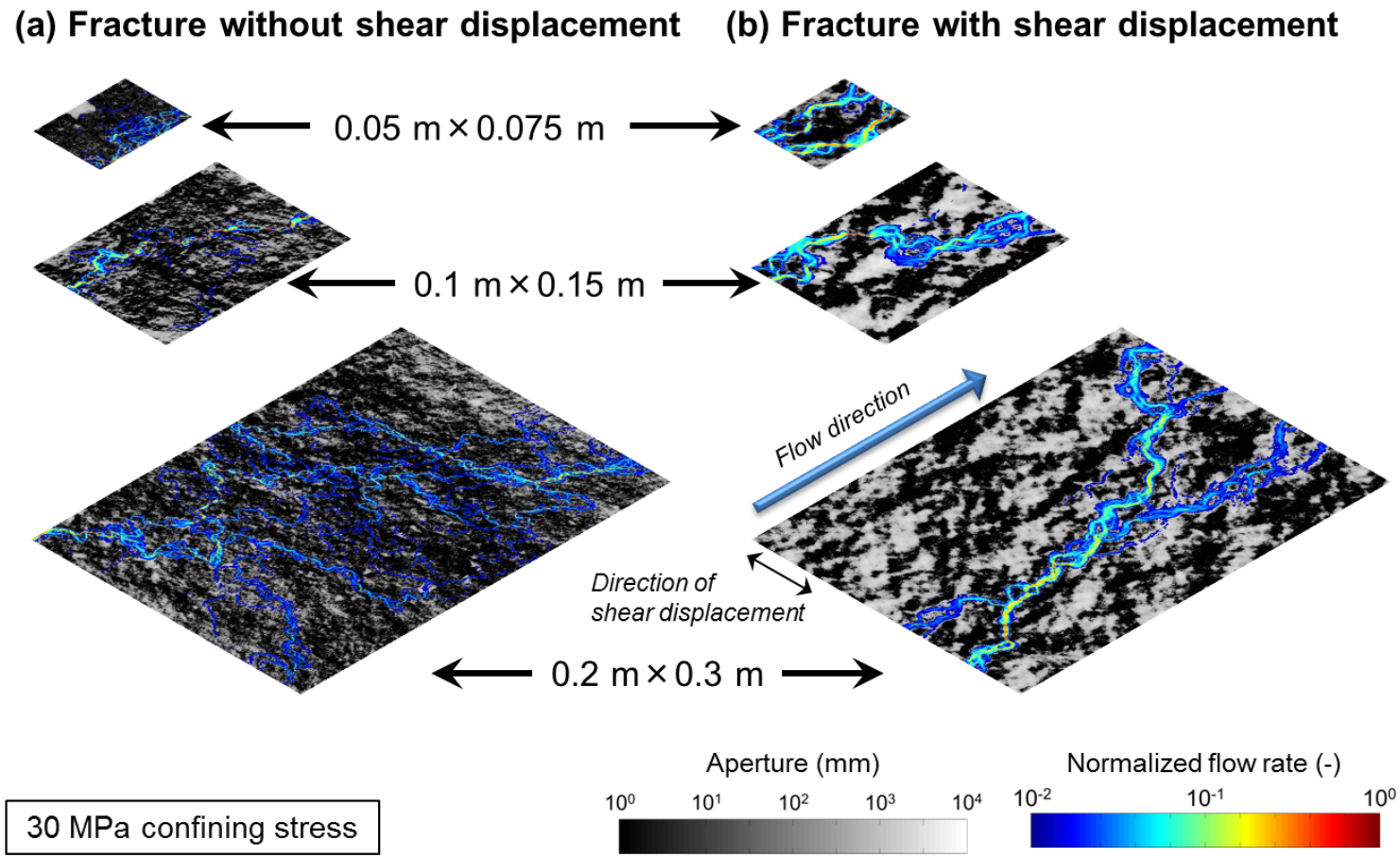

Figure 3-5. Representative results for the channeling flow within the heterogeneous aperture distribution of the real laboratory-scale fractures (a) with no shear displacement and (b) with a shear displacement of 5 mm.

Histograms of the aperture are generally characterized by a significant number of contacting asperities (regions of zero aperture) and the skewed distributions of regions of nonzero aperture with long tails, i.e., lognormal-like distributions, as reported in the literature [*Watanabe et al.,* 2008 and 2009] (Figure 3-6). Therefore, the aperture distributions are evaluated by the geometric mean and standard deviation of nonzero apertures and the percentage of zero apertures (contact area), and these values are summarized in Table 3-1. Figure 3-7 shows the changes in the geometric mean of apertures, referred to hereinafter as the mean aperture, and the contact area with the respect to the fracture length. Due to the shear dilation, fractures with shear displacement generally have a large mean aperture. In addition, fractures without shear displacement have a large contact area due to the high degree of matedeness of the fracture surfaces. The mean aperture of the fracture without shear displacement, which does not change significantly with confining stress, increases with increasing fracture length. On the other hand, the mean aperture of the fracture with shear displacement, which does not change significantly with confining stress, first increases and then decreases with the increase in the fracture length. Since the mean aperture of the largest fracture remains greater than that of the smallest fracture, the mean aperture of the fracture with shear displacement essentially increases with increasing fracture length. The contact area of the fracture without shear displacement, which is slightly larger at higher confining stress, decreases slightly with the increase in the fracture length. In contrast, the contact area of the fracture with shear displacement, which does not change significantly with confining stress, increases slightly with increasing fracture length. The geometric standard deviations are essentially constant for all given conditions, as shown in Table 3-1.

The area of the preferential flow paths, referred to herein as the flow area, is calculated to evaluate the degree of channeling flow (Figure 3-8). For all of the given conditions, the flow area is far from 100% of the fracture plane, demonstrating the difference between reality and the fluid flow through a fracture modeled by parallel smooth plates. The fractures with shear displacement have a rather large flow area, except for the largest fracture, and this trend does not change significantly with confining stress. In the case of a fracture without shear displacement, the flow area is approximately constant throughout the tested fracture scales. On

the other hand, the flow area of the fracture with shear displacement decreases slightly with the increase in the fracture length. In addition to these small flow areas, large differences between the mean aperture and the hydraulic aperture can be found in Table 3-1.

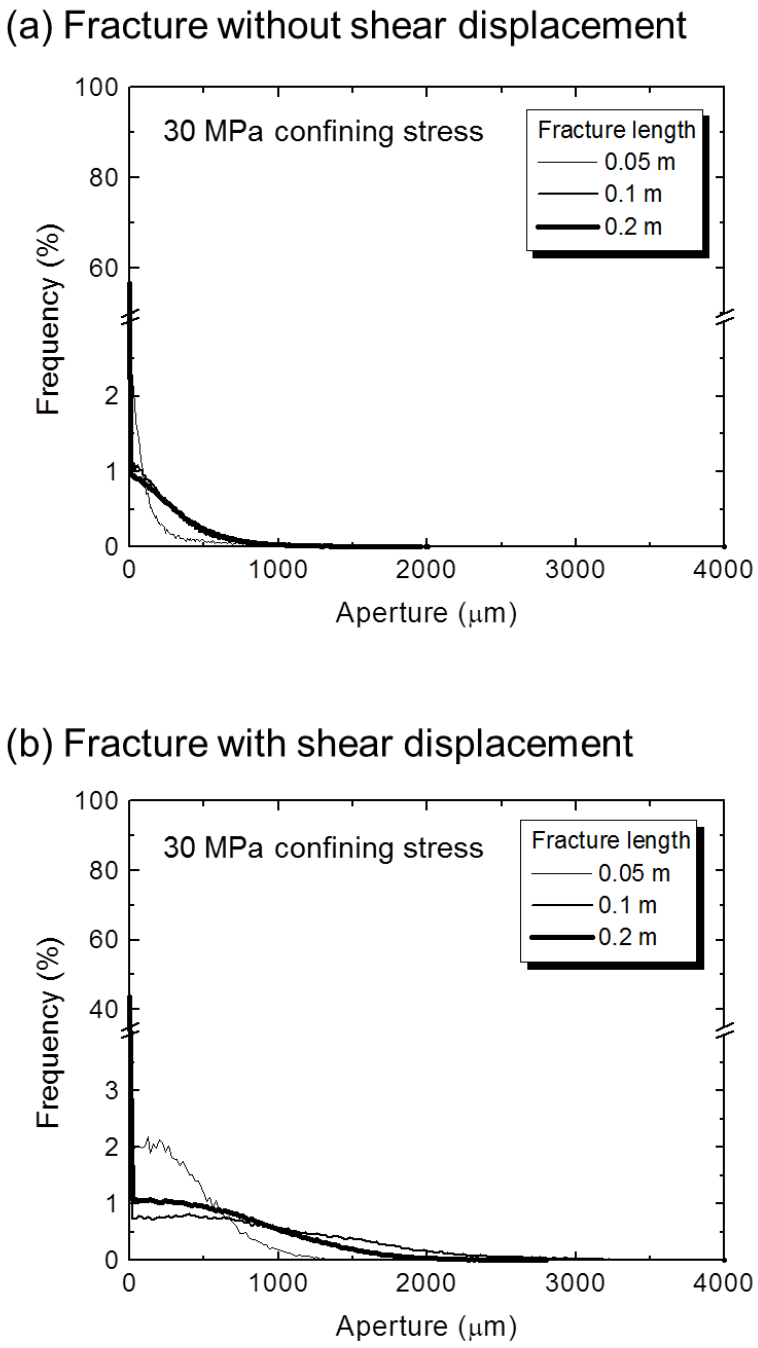

Figure 3-6. Representative results for the histograms of the aperture for the real laboratory-scale fractures with (a) no shear displacement and (b) a shear displacement of 5 mm.

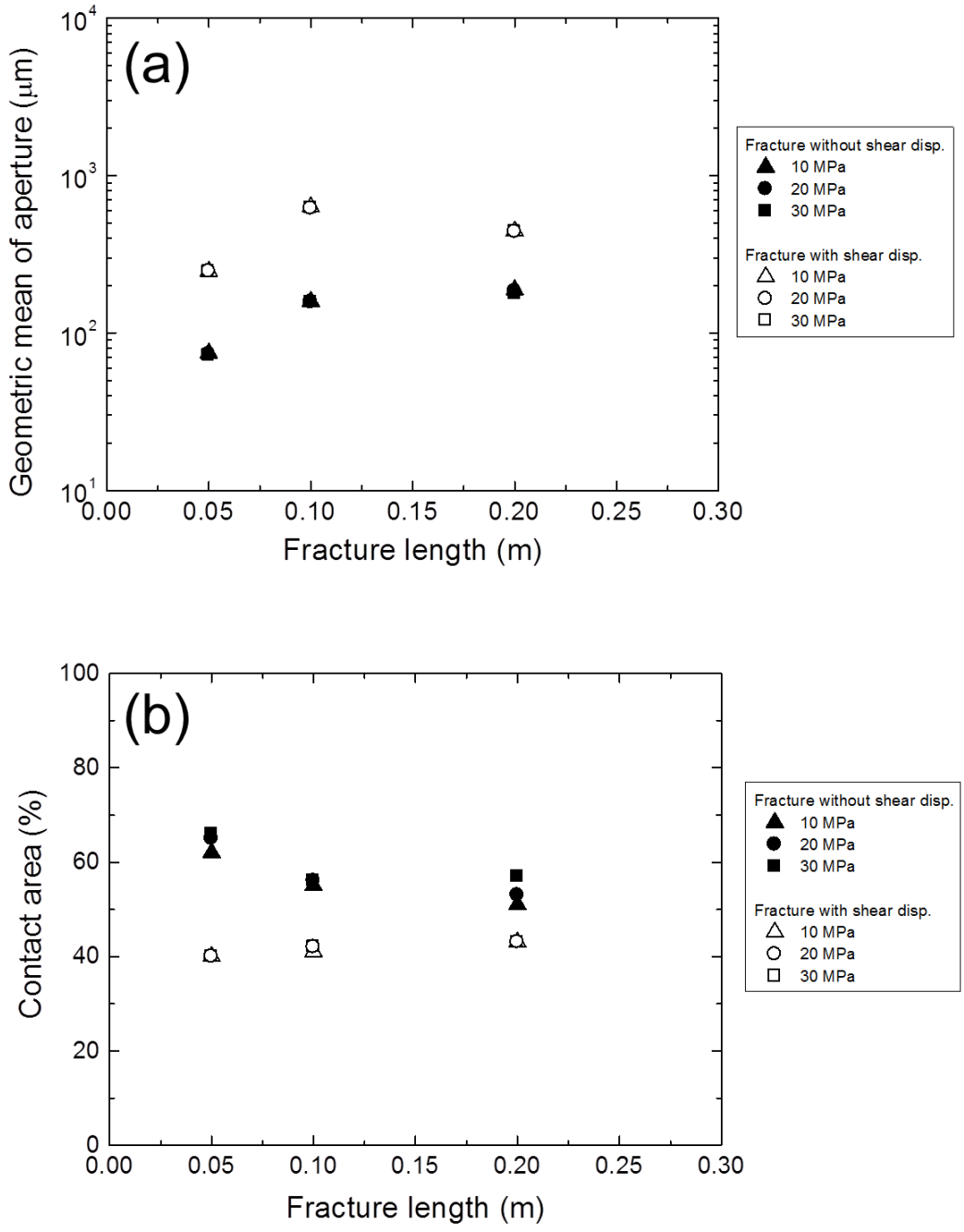

Figure 3-7. Changes in (a) the geometric mean of aperture and (b) the contact area for the real laboratory-scale fractures with no shear displacement and with a shear displacement of 5 mm at confining stresses of 10, 20, and 30 MPa.

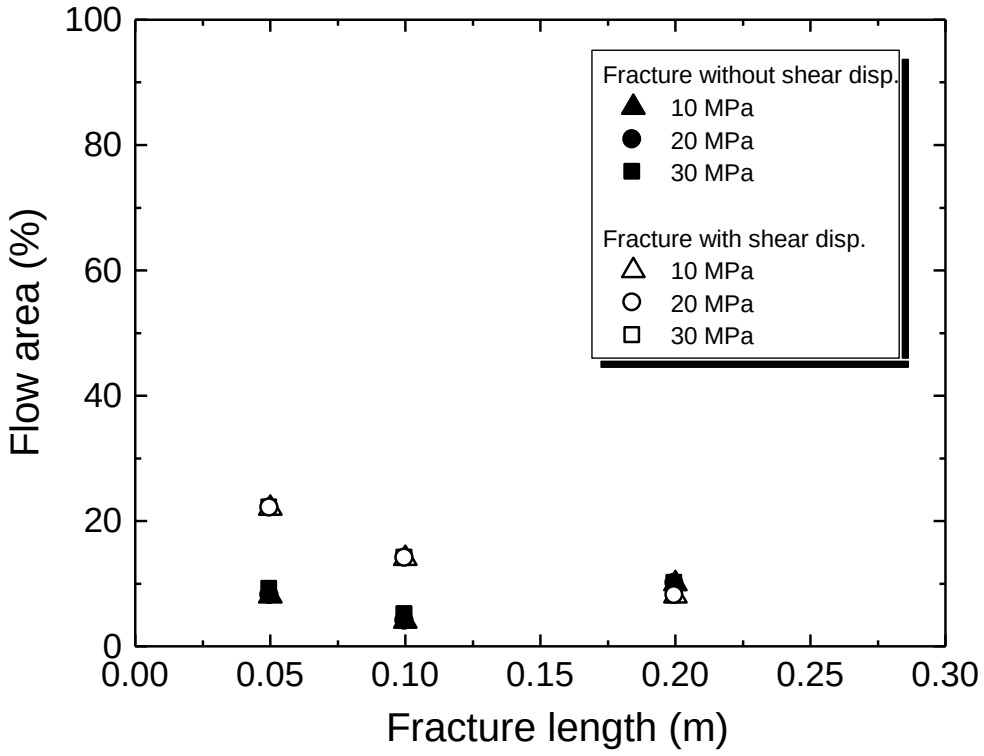

Figure 3-8. Changes in the flow area with the fracture length for the real laboratory-scale fractures with no shear displacement and a shear displacement of 5 mm at confining stresses of 10, 20, and 30 MPa.

Table 3-1. Parameter values characterizing the channeling flow through the heterogeneous aperture distribution of the real fracture.

Shear disp (mm)	Confining stress (MPa)	Fracture length		Fracture permeability (m^2)	Hydraulic aperture (μm)	Flow area (%)	Aperture		Contact area (%)
		Short side (m)	Long side (m)				Geometric mean (μm)	Geometric std. (-)	
0	10	0.05	0.075	6.0×10^{-12}	8.5	8	75	3.7	62
0	10	0.1	0.15	7.0×10^{-12}	9.1	4	158	3.2	55
0	10	0.2	0.3	3.6×10^{-12}	6.6	10	188	3.1	51
0	20	0.05	0.075	2.7×10^{-12}	5.7	8	73	3.8	65
0	20	0.1	0.15	3.0×10^{-12}	6.0	4	158	3.2	56
0	20	0.2	0.3	1.5×10^{-12}	4.3	10	184	3.1	53
0	30	0.05	0.075	1.4×10^{-12}	4.1	9	72	3.8	66
0	30	0.1	0.15	1.7×10^{-12}	4.6	5	157	3.2	56
0	30	0.2	0.3	9.6×10^{-13}	3.4	10	177	3.1	57
5	10	0.05	0.075	1.1×10^{-9}	116	22	246	2.8	40
5	10	0.1	0.15	3.4×10^{-9}	203	14	630	2.8	41
5	10	0.2	0.3	3.8×10^{-9}	213	8	443	2.9	43
5	20	0.05	0.075	1.1×10^{-9}	116	22	246	2.8	40
5	20	0.1	0.15	2.8×10^{-9}	182	14	619	2.9	42
5	20	0.2	0.3	3.6×10^{-9}	208	8	441	2.9	43
5	30	0.05	0.075	1.1×10^{-9}	116	22	246	2.8	40
5	30	0.1	0.15	2.8×10^{-9}	184	14	619	2.9	42
5	30	0.2	0.3	3.6×10^{-9}	207	8	441	2.9	43

Based on the above-described results, the scale dependencies of the heterogeneous fracture aperture distribution and the channeling flow therein are inferred as follows. For both fractures with and without shear displacement, the mean aperture increases with the increase in the fracture length, as demonstrated herein. This scale dependency of the mean aperture may be true because the fractal fracture surface has larger roughness at a larger fracture scale. In the laboratory scale, however, the mean aperture may not always increase significantly with the increase in the fracture scale, due to the self-affinity, rather than self-similarity, of the fractal fracture surface. On the other hand, for both fractures with and without shear displacement, the contact area is virtually independent of scale. In the present study, the contact areas of the fractures with and without shear displacement exhibit opposite changes with respect to increasing fracture length. However, the changes in the absolute contact area are negligible, and there is no reason for such opposite changes for these fractures. As such, these changes in the contact area are not essential, which indicates the scale independency of the contact area. This concept has also been suggested in the literature [*Witherspoon et al.*, 1979]. The scale independency of the contact area may simply implicate the physical balance between confining stress and reactive force at the contacting asperities. The combination of the scale-dependent mean aperture and the scale-independent contact area suggests that the fracture permeability either remains constant or increases with the increase in the fracture length. In the case of a fracture without shear displacement, the permeability may remain approximately constant with the increase in the fracture length because the increase in the aperture has little influence on the permeability enhancement due to the large contact area. In contrast, for a fracture with shear displacement, the permeability may increase monotonically with the increase in the fracture scale due to the small contact area. Moreover, the formation of preferential flow paths with a rather small flow area, which is quite different from the assumption in the parallel smooth plate model, causes the non-monotonic permeability increasing with the fracture scale, as shown herein and inferred from the results in the literature [*Witherspoon et al*., 1979; *Raven and Gale*, 1985; *Matsuki et al.*, 2006].

As described herein, the laboratory investigation provides insight into the scale dependencies of the aperture distributions and channeling flows for subsurface fractures.

However, it is difficult to determine the scale dependencies due to the limited results for a relatively small range of fracture scale in the laboratory investigation. Therefore, a method by which to predict fracture aperture distributions beyond the laboratory scale has been developed based on the fractal nature and the scale-independent contact area of the fracture surface and has been used to address the prescribed problem.

3.3.2. Validity of the method for predicting fracture aperture distributions beyond the laboratory scale

Fracture aperture distributions of the square fractures with side lengths of 0.05 to 0.6 m and the corresponding fluid flows are numerically determined by the prediction method, where the scale-independent contact areas of fractures with and without a shear displacement of 5 mm are set to 42% and 59%, respectively. These values can be obtained by calculating the average of contact area with respect to the fracture type, because the confining stress level has little influence on the contact area. Since the contact area and the other characteristic parameters do not change significantly with the confining stress, in the present study, the predicted aperture distributions and fluid flows can be considered to be representative of the fractures with and without shear displacement under confining stress.

In order to evaluate the validity of the prediction method, the occurrence of channeling flows within the predicted aperture distributions is first confirmed. In the same manner as in Figure 3-5, representative results for the aperture distribution and fluid flow are shown in Figure 3-9. Visual comparison of the distributions between the predicted scale fractures and the real, laboratory-scale fractures qualitatively reveals that the prediction method can reproduce the occurrence of a channeling flow within the heterogeneous fracture aperture distribution. The channeling flow for the predicted fractures beyond the laboratory scale of > 0.2 m × 0.3 m can also be observed, which suggests that this flow phenomenon generally characterizes the fluid flow through the rock fracture, regardless of scale. Quantitative evaluation of the validity of the prediction method is then conducted, primarily through the comparisons of two key parameters, namely, the mean aperture and the fracture permeability, between the predicted fractures and the real laboratory-scale fractures (Figure 3-10). The values of the mean aperture and permeability

for the predicted fractures are generally in agreement with those of the real laboratory-scale fractures. Although relatively large differences are observed between the predicted and real permeabilities for the fracture without shear displacement, the differences are consistent within an order of magnitude. Moreover, the scale dependencies of the mean aperture and the permeability, which are observed in the laboratory investigation, are properly reproduced by the prediction method. Therefore, for both fractures with and without shear displacement, the mean aperture is expected to increase with the increase in the fracture length. In addition, the permeability of the fracture without shear displacement is almost scale-invariant, whereas the permeability of the fracture with shear displacement increases with the increase in the fracture length. The parameter values, which characterize the predicted aperture distribution and fluid flow, are listed in Table 3-2 and are generally consistent with those for the real laboratory-scale fractures.

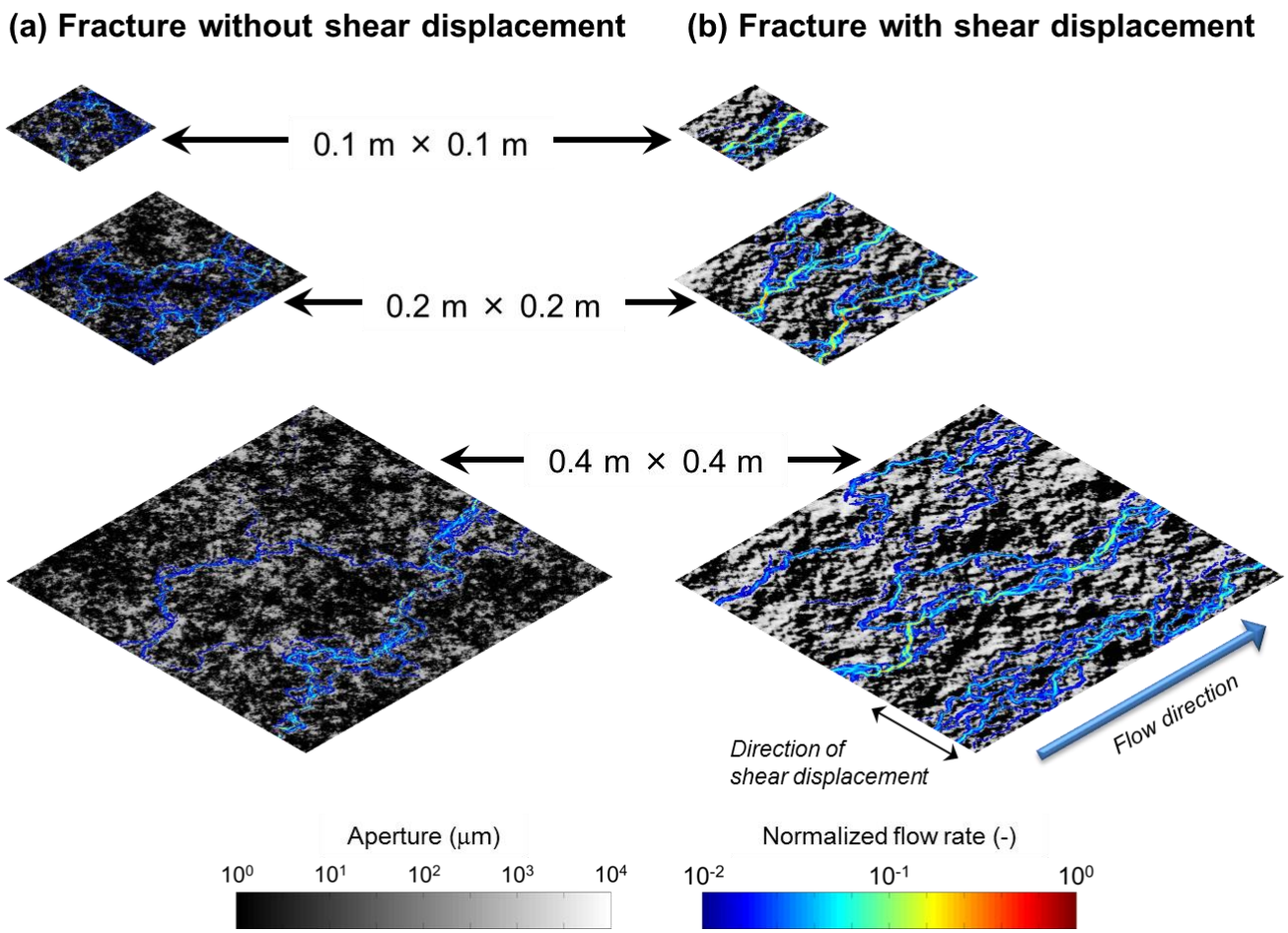

Figure 3-9. Representative results for the channeling flow within the heterogeneous aperture distribution of the predicted fractures (a) with no shear displacement and (b) with a shear displacement of 5 mm.

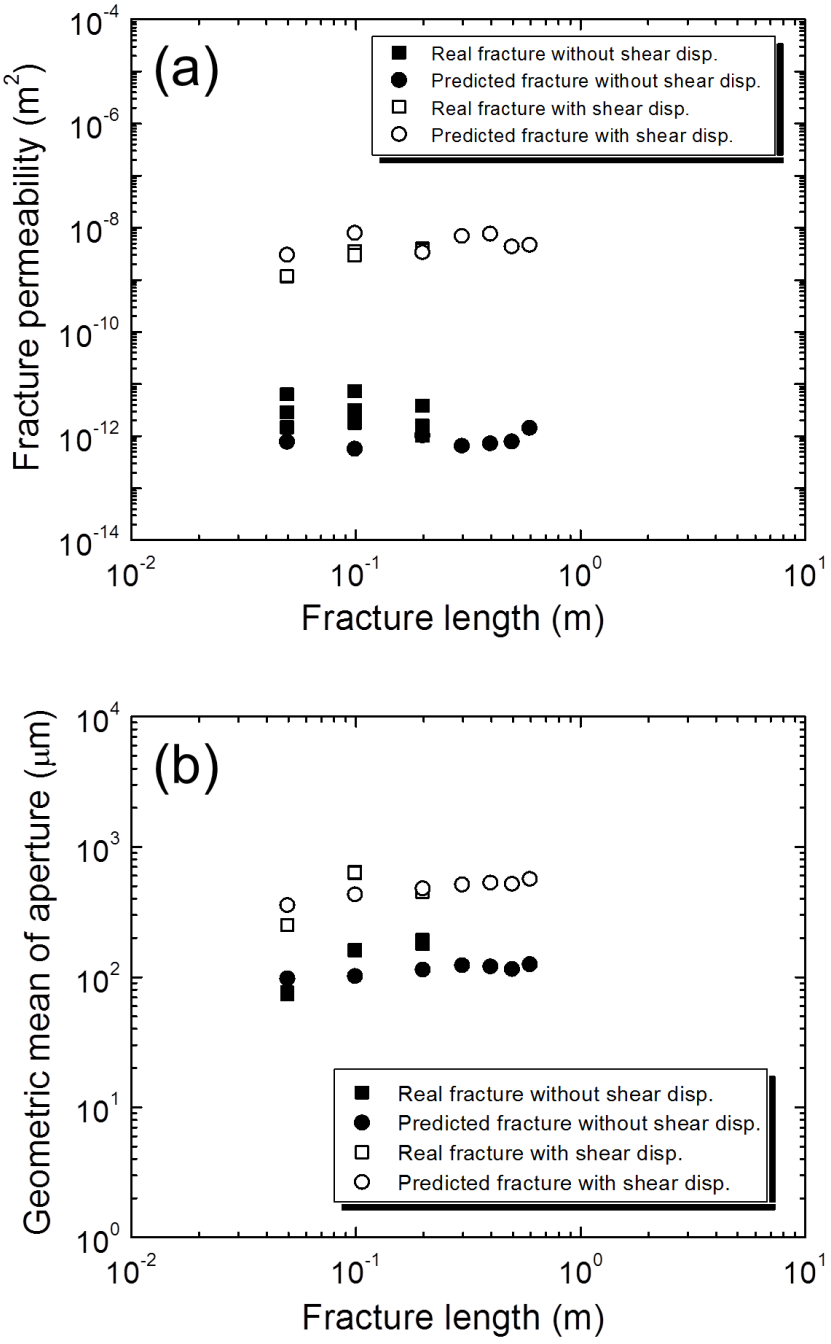

Figure 3-10. Comparisons of (a) the geometric mean of aperture and (b) the permeability between the predicted and the real laboratory-scale fractures with no shear displacement and with a shear displacement of 5 mm. The values for the real fractures are determined at confining stresses of 10, 20, and 30 MPa.

Table 3-2. Parameter values characterizing the channeling flow through the heterogeneous aperture distributions of the predicted fracture under confining stress.

Shear disp. (mm)	Fracture length		Fracture permeability (m^2)	Hydraulic aperture (μm)	Flow area (%)	Aperture		Contact area (%)	Maximum aperture (m)
	Short side (m)	Long side (m)				Geometric mean (μm)	Geometric std. (-)		
0	0.05	0.05	7.4×10^{-13}	3.0	14	95	3.0	59	7.6×10^{-4}
0	0.1	0.1	5.4×10^{-13}	2.5	12	100	3.0	59	8.9×10^{-4}
0	0.2	0.2	9.8×10^{-13}	3.4	13	112	3.0	59	1.0×10^{-3}
0	0.3	0.3	6.2×10^{-13}	2.7	10	121	3.0	59	1.1×10^{-3}
0	0.4	0.4	6.9×10^{-13}	2.9	8	118	3.0	59	1.1×10^{-3}
0	0.5	0.5	7.6×10^{-13}	3.0	11	113	3.0	59	1.2×10^{-3}
0	0.6	0.6	1.4×10^{-12}	4.1	10	123	3.0	59	1.3×10^{-3}
5	0.05	0.05	2.9×10^{-9}	186	14	350	2.9	42	2.2×10^{-3}
5	0.1	0.1	7.6×10^{-9}	301	13	423	2.9	42	3.3×10^{-3}
5	0.2	0.2	3.2×10^{-9}	196	13	471	2.9	42	3.3×10^{-3}
5	0.3	0.3	6.6×10^{-9}	281	12	503	2.9	42	3.5×10^{-3}
5	0.4	0.4	7.3×10^{-9}	296	13	521	2.9	42	3.9×10^{-3}
5	0.5	0.5	4.2×10^{-9}	224	12	509	2.9	42	4.4×10^{-3}
5	0.6	0.6	4.5×10^{-9}	232	12	555	2.9	42	4.3×10^{-3}
0.5*	0.05	0.05	4.1×10^{-10}	70	19	109	2.8	42	7.5×10^{-4}
1*	0.1	0.1	7.7×10^{-10}	96	11	167	2.8	42	1.2×10^{-3}
2*	0.2	0.2	1.9×10^{-9}	152	13	277	2.8	42	2.0×10^{-3}
3*	0.3	0.3	3.2×10^{-9}	197	13	372	2.9	42	2.7×10^{-3}
4*	0.4	0.4	5.9×10^{-9}	266	13	456	2.9	42	3.4×10^{-3}
5*	0.5	0.5	4.0×10^{-9}	219	13	509	2.9	42	4.4×10^{-3}
6*	0.6	0.6	4.7×10^{-9}	236	12	617	2.9	42	5.1×10^{-3}

*Constant ratio of the shear displacement to the short side length of the fracture

As described above, the prediction method has been demonstrated to be valid for fractures created in the laboratory. However, the validity of the prediction method for natural fractures is unclear. To address this concern, the maximum aperture-fracture length relations are obtained for the predicted fractures and are compared to those for natural fractures (joints and faults) reported in the literature [*Cowie and Scholz,* 1992; *Vermilye and Scholz,* 1992; *Schlische et al.,* 1996; *Schultz et al.,* 2008]. Note that the maximum aperture in the present study corresponds to the maximum displacement in the literature. *Vermilye and Scholz* [1992] reported that the maximum aperture (m), e_{max}, and fracture length (m), l, are approximately related by the following formula:

$$e_{\max} = \alpha \cdot l^{n}, \tag{3-5}$$

where α is a pre-exponential factor related to rock properties or tectonic environments, and n is an exponent. In the case of a joint, the maximum aperture ranges from 10^{-4} m to 10^{-3} m for a fracture length ranging from 10^{-2} m to 1 m, and the representative fit curve is given as $e_{\max} = 2.5\times10^{-3}l^{0.48}$ [*Schultz et al.,* 2008]. In contrast, in the case of a fault, the maximum aperture ranges from 10^{-4} m to 10^{5} m for a fracture length ranging from 10^{-3} m to 10^{6} m, which results in a pre-exponential factor of between 0.001 and 0.1 and an exponent of 1.

Figure 3-11 shows the maximum aperture-fracture length relations for the predicted fractures, together with those for joints and faults in nature. In addition to the results for the fractures with no shear displacement and a shear displacement of 5 mm, the results for fractures with a constant ratio of shear displacement to fracture length are summarized in Table 3-2 and are shown in Figure 3-11. In the present study, the results for the fractures with and without shear displacement are compared to those for faults and joints, respectively. However, whether the fractures with a shear displacement of 5 mm are suitable for the comparison remains unclear, because the shear displacement of a fault generally exhibits a linear increase with respect to the fracture scale [*Kanamori and Anderson,* 1975]. Consequently, a constant ratio of shear displacement to fracture length is also used. Here, a relatively large ratio of 0.01 (1% of the fracture length) is assumed because most faults are expected to experience multiple slips, rather than just a single slip. As shown in Figure 3-11, the maximum aperture-fracture length relation for the fracture without shear displacement quantitatively coincided with that for the joint ($e_{\max}$

= $2.5\times10^{-3}l^{0.48}$). Furthermore, the maximum aperture-fracture length relation for the fracture with a constant ratio of shear displacement is quantitatively consistent with the middle relation for the fault ($e_{max} = 0.01l$), whereas the maximum aperture-fracture length relation for a fracture with a constant shear displacement is inconsistent with the relations for natural faults, which is as expected. Thus, the prediction method has also been demonstrated to be valid for natural fractures (joints and faults).

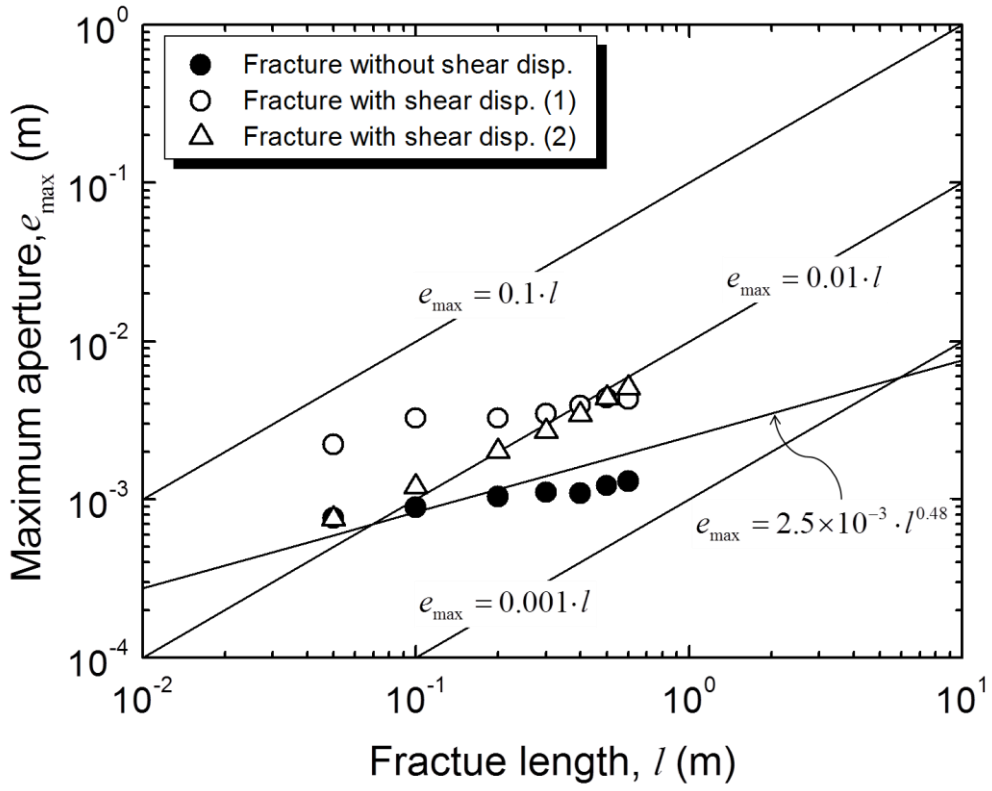

Figure 3-11. Comparison of the maximum aperture-fracture length relations between the predicted and the natural fractures. The results are for the predicted fractures with two types of shear displacement: (1) a constant shear displacement of 5 mm and (2) a shear displacement that is a constant 1% of the fracture length. One of the linear curves, $e_{max} = 2.5\times10^{-3}l^{0.48}$, corresponds to the relation of the joint, whereas the other linear curves correspond to the relations of the fault [*Schlische et al.*, 1996; *Schultz et al.*, 2008].

3.3.3. Scale dependency of a channeling flow through a heterogeneous fracture aperture distribution

Since the prediction method has been demonstrated to be valid for natural fractures, the present study finally discusses conceivable scale dependencies of channeling flows through the heterogeneous aperture distributions of natural fractures, i.e., joints and faults. Considering the above discussion, we assume that the prediction results for fractures without shear displacement are relevant to the typical scale dependencies of joints, whereas the prediction results for the fractures with a constant ratio of shear displacement are relevant to the typical scale dependencies of faults. The parameter values used in the present discussion are listed in Table 3-2.

Figure 3-12a shows the changes in the mean aperture with the fracture length for both fractures with and without shear displacement, which are hereinafter referred to as faults and joints, respectively. For both joints and faults, the mean aperture increases with the increase in the fracture length, whereas the standard deviation is almost independent of scale and is approximately 3, as summarized in Table 3-2. The increase in the mean apertures may have occurred because the fracture surface becomes rougher with the increase in the fracture length and the contact area is a scale-independent value. The increase in mean aperture for joints and faults are linear on a log-log plot, and are respectively approximated by

$$e_{m,\ joint} = 1\times10^{2}l^{0.1}, \tag{3-6}$$

$$e_{m,\ fault} = 1\times10^{3}l^{0.7}, \tag{3-7}$$

where $e_{m,\ joint}$ and $e_{m,\ fault}$ are the mean apertures (μm) of joints and faults, respectively, and l is the fracture length (m). Both equations have exponents smaller than unity due to the self-affine fractal nature of the fracture surface. In particular, the exponent is very small for the joint, indicating the weak scale dependency of the mean aperture. The small exponent is due to the high degree of matedness for the two opposite fracture surfaces.

Figures 3-12b and 12c show the change in permeability and flow area with fracture length for joints and faults. The permeabilities of both joints and faults also increase linearly with fracture length on a log-log plot and are approximated by

$$k_{joint} = 1\times10^{-12}l^{0.2}, \tag{3-8}$$

$$k_{fault} = 1\times10^{-8}l^{1.1}, \quad (3\text{-}9)$$

where k_{joint} and k_{fault} are the permeabilities (m^2) of joints and faults, respectively. For both joints and faults, the exponents for the permeability are greater than those of the mean aperture. The permeabilities have stronger scale dependencies than those of the mean apertures, because the local permeabilities are proportional to the square of the local apertures (i.e., local cubic law). However, the pre-exponential factors and exponents in Equations 3-8 and 3-9 are smaller than those expected from Equations 3-6 and 3-7 with an assumption of the parallel smooth plate model, where the fracture permeability is proportional to the square of the mean aperture. This is because the flow area within a fracture is quite small due to the channeling flow, as shown in Figure 3-12c, which diverges significantly from the assumption. Due to the significantly small exponent for the joint, the permeability is approximately constant with respect to the fracture scale. Note that Equations 3-6 through 3-9 may be used to predict the fracture flow characteristics for a confining stress of up to approximately 100 MPa. This constraint can be inferred from the study of *Watanabe et al.* (2008), who showed that the change in the fluid flow characteristics of the fracture is relatively small with an increase in confining stress of from 30 MPa to 100 MPa. In contrast, for both joints and faults, the flow area is virtually independent of scale and is approximately 10% of the fracture plane. Considering the scale-independent contact area of approximately 60% for joints and 40% for faults, we assume the existence of a noncontact area that does not contribute to the fluid flow for both joint and fault planes. The noncontact areas (i.e., a stagnant area of fluid) of joints and faults, which are also scale-independent values, are estimated to be approximately 30% and 50%, respectively. The estimated flow area within the fracture plane corresponds well with the flow area evaluated through field investigations [*Abelin et al.*, 1985].

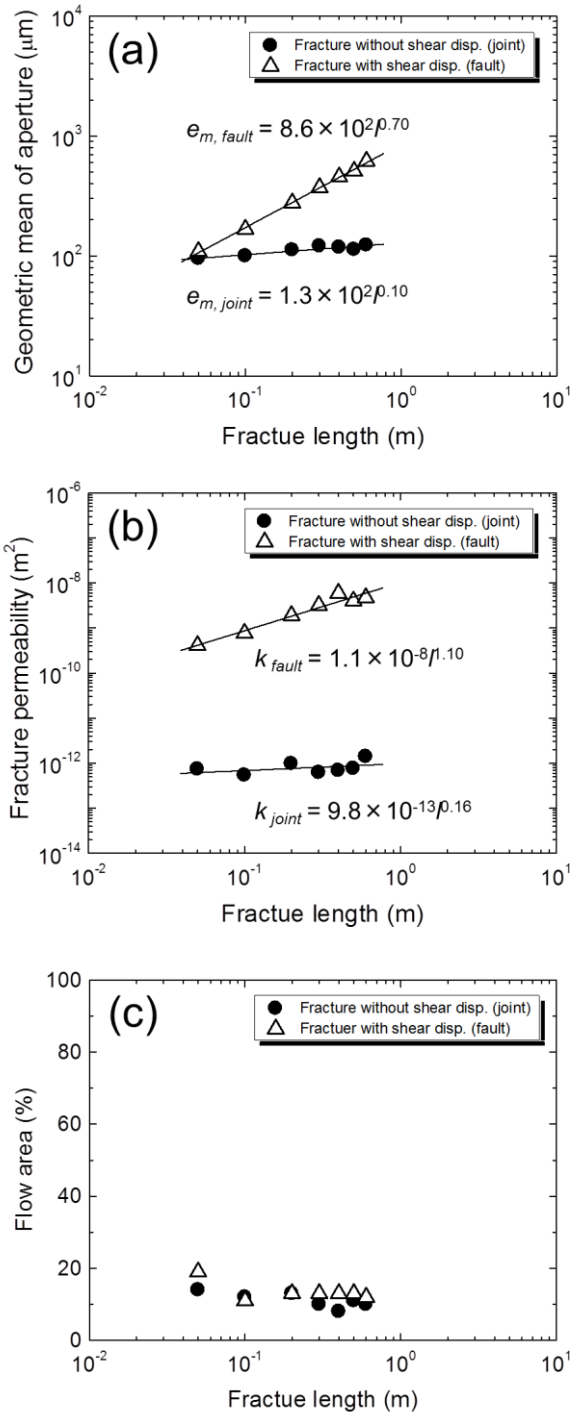

Figure 3-12. Predicted typical changes in the (a) geometric mean of aperture, (b) the permeability, and (c) the flow area, all with respect to the fracture length, for fractures with no shear displacement (joints) and fractures with a constant ratio of shear displacement to fracture length (faults).

3.4. Conclusions

We evaluated heterogeneous aperture distributions and resulting channeling flows for granite fractures of various sizes under confining stress. As a significant result, the scale independency of contact area of the fracture was revealed, which, in combination with the well-known fractal nature of the fracture surfaces, provides a novel method by which to predict fracture aperture distributions beyond the laboratory scale. The validity of the proposed method was revealed through the reproduction of the results in a laboratory investigation and the maximum aperture-fracture length relations, which have been reported in the literature, for natural fractures (i.e., joints and faults).

Subsequently, for joints and faults of various sizes, representative aperture distributions and resulting channeling flows were numerically determined under confining stress. The characteristics of the aperture distributions and the fluid flow were evaluated, and the changes in the mean aperture and permeability with the fracture scale were formulated. Therefore, we can now predict conceivable scale dependencies of channeling flows through heterogeneous aperture distributions from laboratory-scale to field-scale natural fractures.

In summary, these results are essential to the design of fracture networks with scale-dependent heterogeneous aperture distributions in the field scale. Such precise analysis of a fracture network will provide new insight into transport phenomenon within a fracture network, which will be significant for the engineering and scientific applications such as the development of hydrocarbons or geothermal reservoirs and the clarification of earthquake mechanisms.

Appendix 3-A: Spectral method for modeling a self-similar fracture surface

In the present study, we numerically model the surface geometries of rock fractures by a spectral method based on fractional Brownian motion (fBm) [*Peitgen and Saupe*, 1988]. In this method, a fractal surface is created by the inverse Fourier transform of the Fourier components that are given according to the scaling law of the surface height, which is determined by the fractal dimension of the rock surface D. The discrete inverse Fourier transform to create an isotropic fracture surface $h(x,y)$ of size $l \times l$ with $N \times N$ points is given as

$$h(x,y)=\sum_{p=0}^{N-1}\sum_{q=0}^{N-1}a_{p,q}e^{i2\pi((ps+qt)/N)} \tag{A1}$$

where $a_{p,q}$ is a complex Fourier component of the surface for the spatial frequencies p/l and q/l in the X- and Y-directions, respectively. Note that x and y are discretized as

$$x = s\Delta x \ (s = 0, N\text{-}1) \tag{A2}$$

$$y = t\Delta y \ (t = 0, N\text{-}1) \tag{A3}$$

where Δx and Δy are the grid spacing in the X- and Y-directions, respectively ($\Delta x = \Delta y = l/(N\text{-}1)$). Since the surface height data is real numbers, the Fourier components must satisfy the following conjugate conditions [*Peitgen and Saupe*, 1988]:

$$a_{N-p,N-q}=\overline{a_{p,q}} \quad (p,\ q\ >\ 0) \tag{A4}$$

$$a_{0,N-q}=\overline{a_{0,q}} \quad (q>0) \tag{A5}$$

$$a_{N-p,0}=\overline{a_{p,0}} \quad (p\ >\ 0) \tag{A6}$$

$$a_{0,0}=\overline{a_{0,0}} \tag{A7}$$

where the overbar indicates a complex conjugate. Since the constant component $a_{0,0}$ is assumed to be zero in the present study, the mean height of the surface is always zero. For the fracture surface geometry with fractal dimension D, the Fourier component $a_{p,q}$ can be given as a function of the spatial frequency f ($=\sqrt{(p^2+q^2)/l^2}$) in an arbitrary direction by

$$a_{p,q}\propto(p^2+q^2)^{-((4-D)/2)}e^{i2\pi R_1} \tag{A8}$$

where f and R_1 are a spatial frequency and a series of uniform random numbers between 0 and 1, respectively.

In the present study, the surface height is adjusted after taking the inverse Fourier transform of Equation (A8) with an arbitrary proportional constant so that the average standard deviation (SD) determined for all linear profiles of the surface height, σ_h, satisfies the following scaling law for the SD:

$$\sigma_h=\sigma_{h0}\left(\frac{l}{l_0}\right)^{3-D} \tag{A9}$$

where σ_{h0} is the SD of the surface height along a linear profile of a fracture surface of size l_0, and these values are determined for a reference fracture surface. The derivation of Equation (A9) is explained in detail in *Matsuki et al.* (2006). Thus, one of the self-similar fracture surfaces, e.g., the upper surface, can be modeled with a designated roughness for the linear

profiles of the surface height (σ_h) and the fractal dimension (D) for an arbitrary scale.

Appendix 3-B. Method for modeling the other fracture surface

In modeling the other fracture surface (i.e., lower surface), a gradual increase in the matedness between the two surfaces must be considered for wavelengths greater than the mismatch length scale (λ_c) [*Brown et al.*, 1986; *Wang et al.*, 1988; *Brown*, 1995]. Note that the degree of matedness can be evaluated through the ratio of the PSDs of the initial aperture with at least a single contact point and the surface height. To realize this, we introduce a Fourier component for the lower surface having the same amplitude as that for the upper surface, but with a different relative phase from that of the upper surface. As a result, $a_{p,q}$ of the lower surface is given by

$$a_{p,q} \propto (p^2+q^2)^{-((4-D)/2)} e^{i(2\pi R_1 + 2\pi\gamma(f)R_2)} \tag{A10}$$

where R_2 is a series of random numbers that is independent of R_1 in Equation (A8) for the upper surface, and $\gamma(f)$ is a function of the spatial frequency, f, which is less than or equal to 1. Thus, the difference in phases between the two fracture surfaces is given by $2\pi\gamma(f)R_2$, for which

$$\gamma(f) = \begin{cases} 1 & (f \geq f_c) \\ \gamma(f) & (f < f_c) \end{cases} \tag{A11}$$

where f_c is the inverse of the mismatch length scale ($1/\lambda_c$). For both the upper and lower surfaces, the heights are given by the distances from the same reference plane.

Based on the above considerations, the effect of the phase difference on the ratio of the initial aperture PSD to the surface height PSD is considered. The Fourier component of the initial aperture $e_{p,q}$ is given by

$$e_{p,q} \propto (p^2+q^2)^{-((4-D)/2)} e^{i2\pi R_1} (1 - e^{i2\pi\gamma(f)R_2}) \tag{A12}$$

because the initial aperture is obtained by taking the difference between the heights of the upper and lower surfaces. Since the PSD is the squared amplitude of the Fourier component, the ratio of the PSDs between the initial aperture and the surface height, $r(f)$, is defined as

$$r(f) = \left\| \frac{e_{p,q}}{a_{p,q}} \right\|^2 . \tag{A13}$$

By substituting Equations (A8) and (A12) into Equation (A13), we obtain

$$r(f) = 2\{1 - \cos(2\pi\gamma(f)R_2)\}. \tag{A14}$$

Furthermore, the expectation of the ratio, $E(r)$, can be calculated by the following integral with respect to the random number R_2:

$$E(r) = \int_0^1 r(f)dR_2 \ . \tag{A15}$$

Considering Equation (A11), $E(r)$ is obtained as follows:

$$E(r) = \begin{cases} 2 & (f \geq f_c) \\ 2\left(1 - \dfrac{\sin 2\pi\gamma(f)}{2\pi\gamma(f)}\right) & (f < f_c) \end{cases}. \tag{A16}$$

For spatial frequencies greater than f_c, the expectation of the ratio is 2, which indicates that the two surfaces are completely independent of each other. In contrast, the expectation of the ratio is less than 2 for spatial frequencies of less than f_c, which means that the two surfaces are more or less correlated. When a gradual change in the matedness between the two surfaces can be expressed by a curve, $R(f)$, for spatial frequencies of less than f_c, the following equation must be satisfied:

$$2\left(1 - \frac{\sin 2\pi\gamma(f)}{2\pi\gamma(f)}\right) = R(f) \ . \tag{A17}$$

By solving Equation (A17) using the Newton-Raphson method, the function $\gamma(f)$ can be determined. Thus, the other self-similar fracture surfaces, e.g., the lower surface, can be created with the designed roughness, fractal dimension, and matedness with the corresponding upper surface for an arbitrary scale.

Nomenclature & Greek symbols

D	fractal dimension
e	local aperture, m
e_h	hydraulic aperture, m
e_{max}	maximum aperture, m
$e_{mean,\ fault}$	mean aperture of fautl, m
$e_{mean,\ joint}$	mean aperture of joint, m
f	spatial frequency, 1/m
f_c	inverse of the mismatch length scale, 1/m
h	surface height, m
k	fracture permeability, m^2
k_{fault}	permeability of fault, m^2
k_{joint}	permeability of joint, m^2
l	fracture length, m
l_0	reference fracture length, m
L	long side length of fracture, m
P	Pressure of the fluid, Pa
ΔP	differential pressure, Pa
Q	flow rate, m^3/sec
W	short side length of fracture, m
Δx	grid spacing in X-direction, m
Δy	grid spacing in Y-direction, m
α	pre-exponential factor
μ	viscosity of the fluid, Pa·sec
λ_c	mismatch length scale, m
σ_h	standard deviation of surface height, m
σ_{h0}	reference standard deviation of surface height, m

Chapter Ⅳ

Universal modeling of fluid flow characteristics through subsurface rock fractures

4.1. Introduction

In Chapter Ⅲ, a novel predicting method of channeling flow through subsurface rock fractures beyond laboratory scale is developed, where a pair of fractal fracture surfaces are contacted so that they have the scale independent contact area. Then, the validity of the prediction method is revealed, and conceivable scale dependencies of aperture distributions and fluid flow characteristics of subsurface fractures, such as joints and faults, are suggested.

However, the suggested scale dependencies of aperture distributions and fluid flow characteristics of subsurface fractures can be applied just under the regulated condition where the ratio of shear displacement to fracture length is equivalent to 0.01 (1% of the fracture length). In contrast, an actual fractured reservoir is constructed by a number of fractures with various combinations of fracture scale and shear displacement, and it is desirable that fluid flow characteristics of subsurface rock fractures are revealed for a wide range of conditions for fracture scale, shear displacement, and confining stress. Without this finding, it is still difficult to construct realistic discrete fracture network models of a fractured reservoir for analyzing with GeoFlow [*Ishibashi et al.*, 2012]. Such a finding is also valuable for understanding the dynamics of rock fractures, which include shear dilation and induced seismicity due to hydraulic fracturing in fractured reservoirs [*Min et al.*, 2004; *Faoro et al.*, 2009; *Manga et al.*, 2012]. However, to date a comprehensive view for the geometric and hydraulic characteristics of rock fracture, which incorporate all of the prescribed effects *a priori*, has not been evolved.

In this chapter, aperture distributions and fluid flows are numerically determined for rock fractures with various combination of fracture scale and shear displacement by using the prediction method of fracture aperture distributions beyond laboratory scale, which is developed in Chapter Ⅲ. Through evaluating these aperture distributions and fluid flows, fluid flow characteristics of subsurface rock fractures are revealed for a wide range of conditions for fracture scale, shear displacement, and confining stress. Furthermore, geometric and hydraulic characteristics of natural rock fractures are discussed on the basis of these evaluations.

4.2. Methods

In order to determine the aperture distributions of rock fractures with various combinations of fracture scale and shear displacement, the fracture surfaces of various scales are first created numerically. The detail for numerical creation of fracture surfaces with a desired fractal dimension and roughness is explained in Appendix 3-A in Chapter Ⅲ. When this method is applied, the fractal dimension of rock fracture surface (D) and the standard deviation (SD) of the surface height along a linear profile of a fracture surface of size L_0 (σ_{h0}) are set as summarized in Table 4-1. Parameters shown in Table 4-1 are corresponding to the values for the tensile fractures of granite. In the present study, the square fracture surfaces with the scale (L) of 80 and 160 m are created in the 0.1 m square grid system. Furthermore, the square fracture surfaces with the scale of 240, 320, and 400 m are created in the 0.2 m square grid system. These values of grid spacing are enough small to reproduce the original fluid flow paths within the rock fractures, and are generally determined by considering the performance of computers used for the calculation.

Table 4-1. Parameters used in the numerical modeling of rock fracture surfaces.

Fractal dimension, D	2.29
Standard deviation of linear profile of surface height, σ_0 [mm]	1.3
Reference size of fracture surface, L_0 [m]	0.2

By using these fracture surfaces, aperture distributions are numerically determined for rock fractures under confining stress with various combinations of fracture scale (m), L, and shear displacement (m), δ. The prediction method of fracture aperture distributions beyond laboratory scale, which is developed in Chapter Ⅲ, are applied herein. The upper and lower fracture surfaces are first sheared by δ [m] with each other, and then contacted so that the contact area is equivalent to 42%. The aperture of contacting asperities is set to 10 μm for convenience in this chapter, since the maximum apertures for the determined aperture distributions of field scales are relatively large. This assumption is validated preliminarily. Since

the contact area is nearly constant between 30 MPa and 100 MPa [*Watanabe et al.*, 2008], it is considered that the aperture distributions are determined under the condition of confining stress from 30 MPa to 100 MPa. The shear displacement is given in the direction of the fracture's width (*X*-direction), therefore the fracture's width (m), *w*, is δ[m] shorter than the fracture's length (*Y*-direction, m), *l* (Figure 4-1). In this study, the shear displacement, δ, is determined for each scales of fracture so that the ratios of the shear displacement to the fracture scale ("shear displacement" hereafter), δ/L, are equivalent to 0.00125 (0.125%), 0.0025 (0.25%), 0.005 (0.5%), 0.01 (1%), 0.02 (2%), 0.05 (5%), and 0.075 (7.5%). A total of 35 aperture distributions of subsurface rock fractures are created numerically.

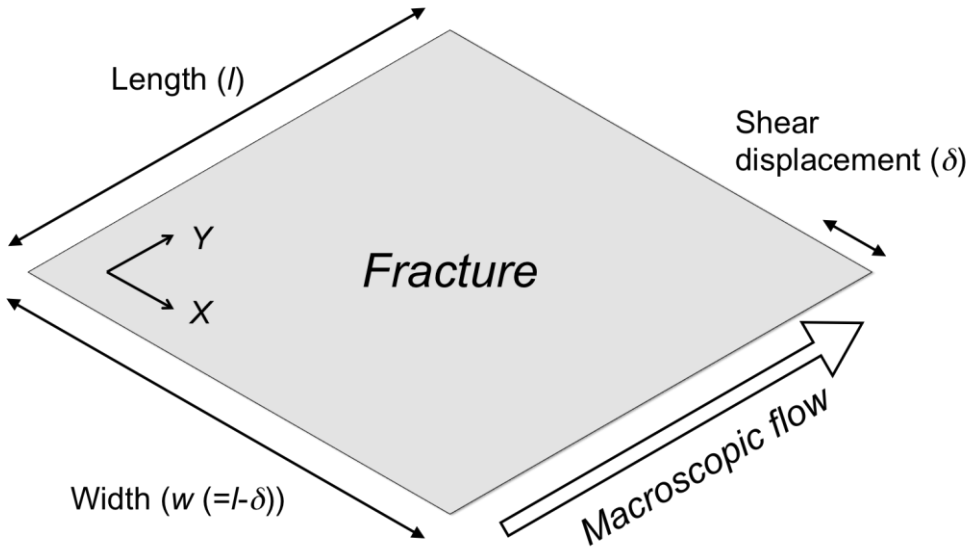

Figure 4-1. Length, width, and shear displacement defined for a fracture with shear displacement.

For these aperture distributions, it is preliminary confirmed that the histograms of heterogeneous apertures are characterized by a significant number of contact points and the skewed distributions of noncontact points (nonzero values) with long tails, i.e., lognormal-like distributions, regardless of fracture scale or shear displacement. Therefore, the numerically created aperture distributions are evaluated by the geometrical mean and standard deviation of local apertures, and the maximum aperture. Then, the fluid flows within these aperture distributions are analyzed, where the Reynolds equation is solved for the each aperture

distributions with a finite difference method. The details of the fluid flow simulation are explained in 3.2.1 in Chapter Ⅲ. With respect to the results of fluid flow simulations, the distributions of flow paths, fracture permeability, hydraulic aperture, and the flow area, which means the area of the preferential flow paths within a fracture, are evaluated.

4.3. Results and Discussion

4.3.1. Channeling flows through heterogeneous aperture distributions of the field scale subsurface rock fractures

Figures 4-2 and 4-3 show the representative results for the numerically created heterogeneous aperture distributions of rock fractures and for the channeling flow through them. In Figure 4-3, the flow rate distributions shown in color scale are superimposed on the corresponding aperture distributions, which are shown in gray scale. Moreover, the scale dependent changes in the heterogeneous aperture distributions and the channeling flow within rock fractures are highlighted in Figure 4-4. The flow rates in Figure 4-3 and 4-4 are normalized by the total flow rate for each condition, and flow rates of ≥ 0.01 (1% of the total flow rate) are shown in these figures. The distribution of the colored points therefore maps the dominant flow paths within the aperture distribution, because colorless points have negligibly small flow rates. As is revealed in Figure 4-3, regardless of fracture scale or shear displacement, fluid flows within subsurface fractures are consistently characterized by channeling flow. Figures 4-2 and 4-3 suggest the following; for each scale of fracture, the groupings of contacting asperities arrayed in the perpendicular direction to the shear displacement are advanced with increasing shear displacement. Moreover, large flow rates appear with a relatively high frequency for the fractures with relatively large shear displacement, which means that the degree for the concentration of preferential flow path become higher with increasing the shear displacement. Figure 4-4 suggests that the width of flow paths increases with increasing fracture scale regardless of shear displacement.

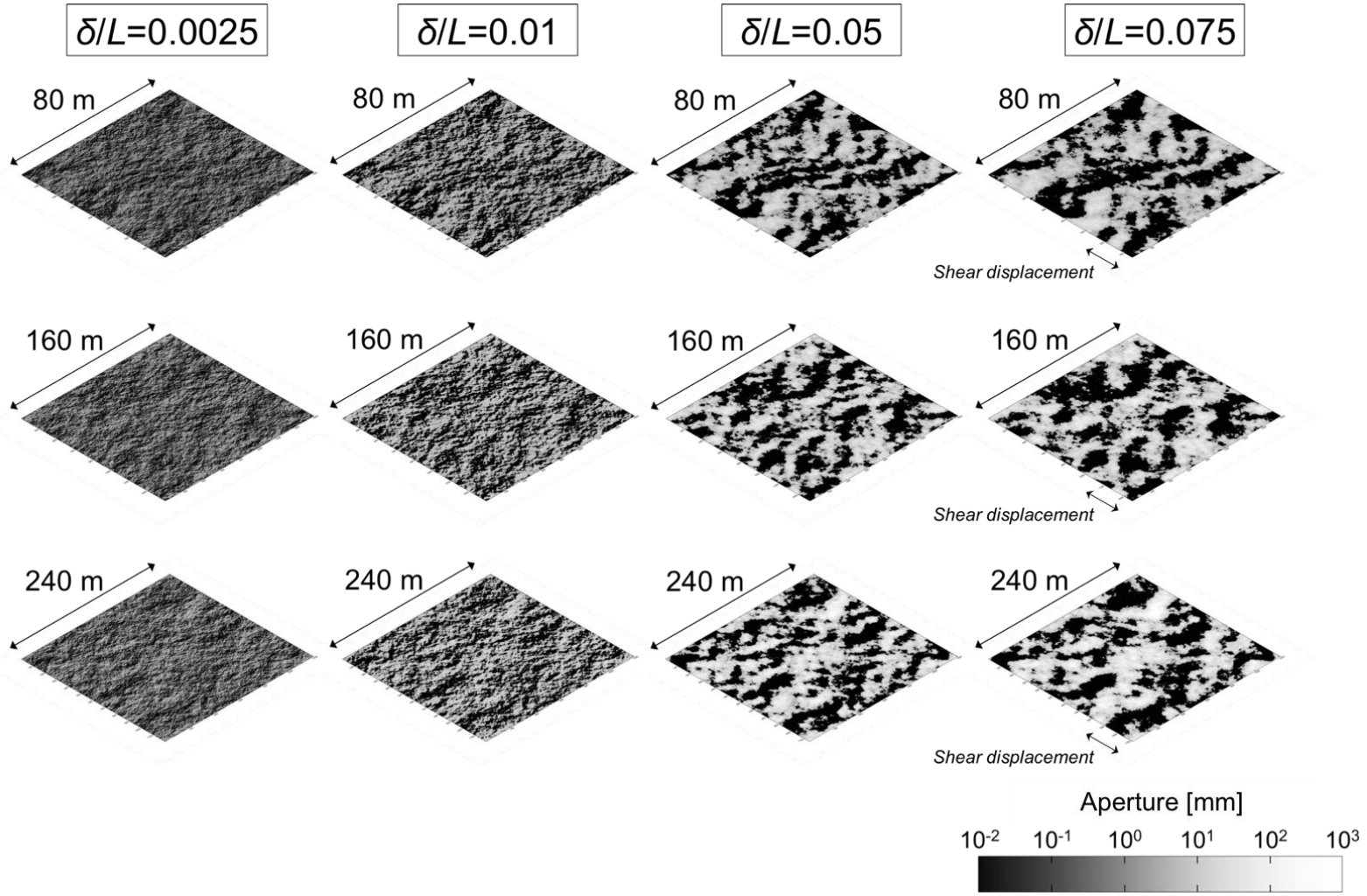

Figure 4-2. Representative results for the heterogeneous aperture distributions of numerically modeled fractures with various combinations of fracture scale and shear displacement under confining stress.

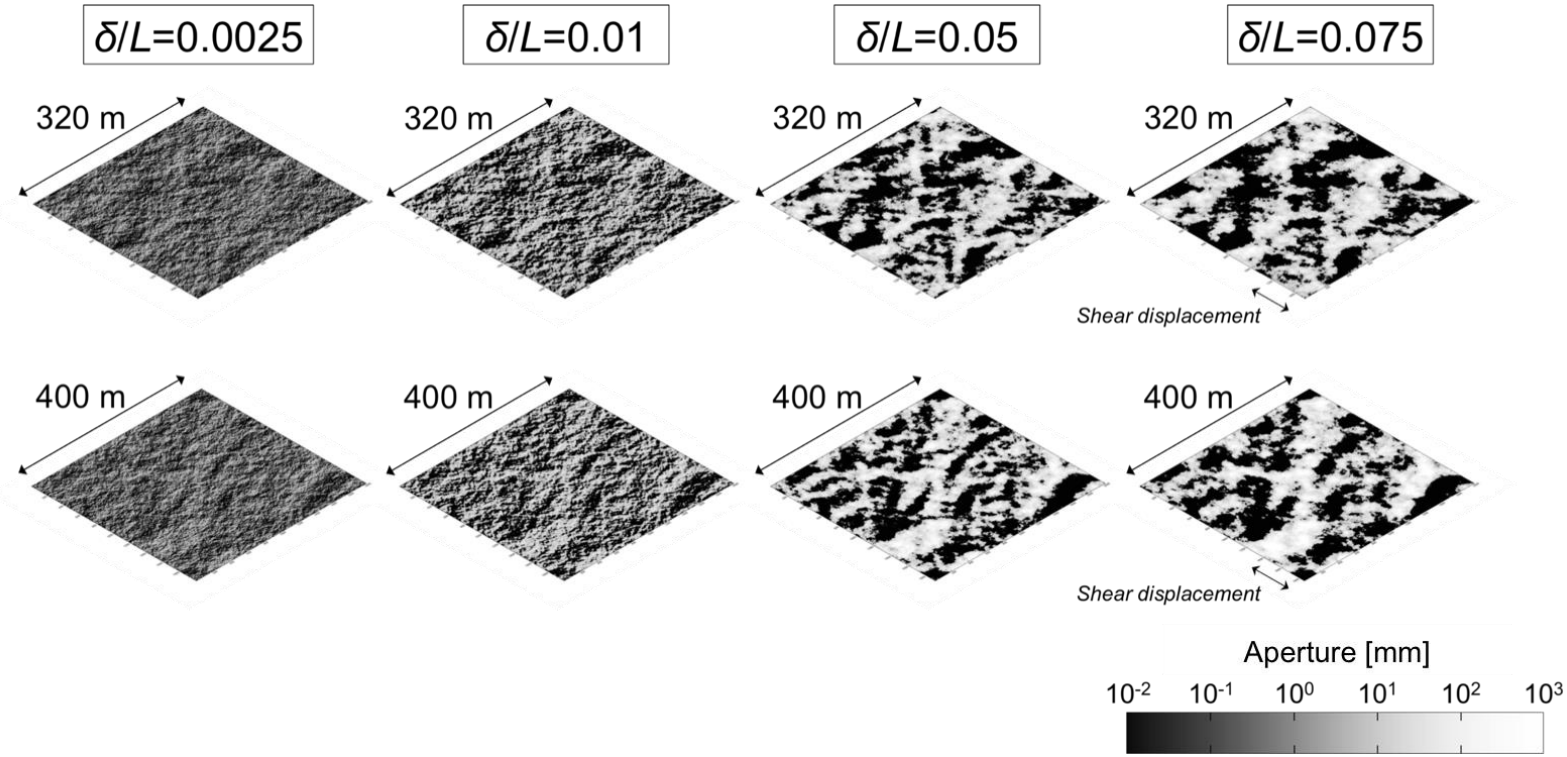

Figure 4-2. (*Continued*)

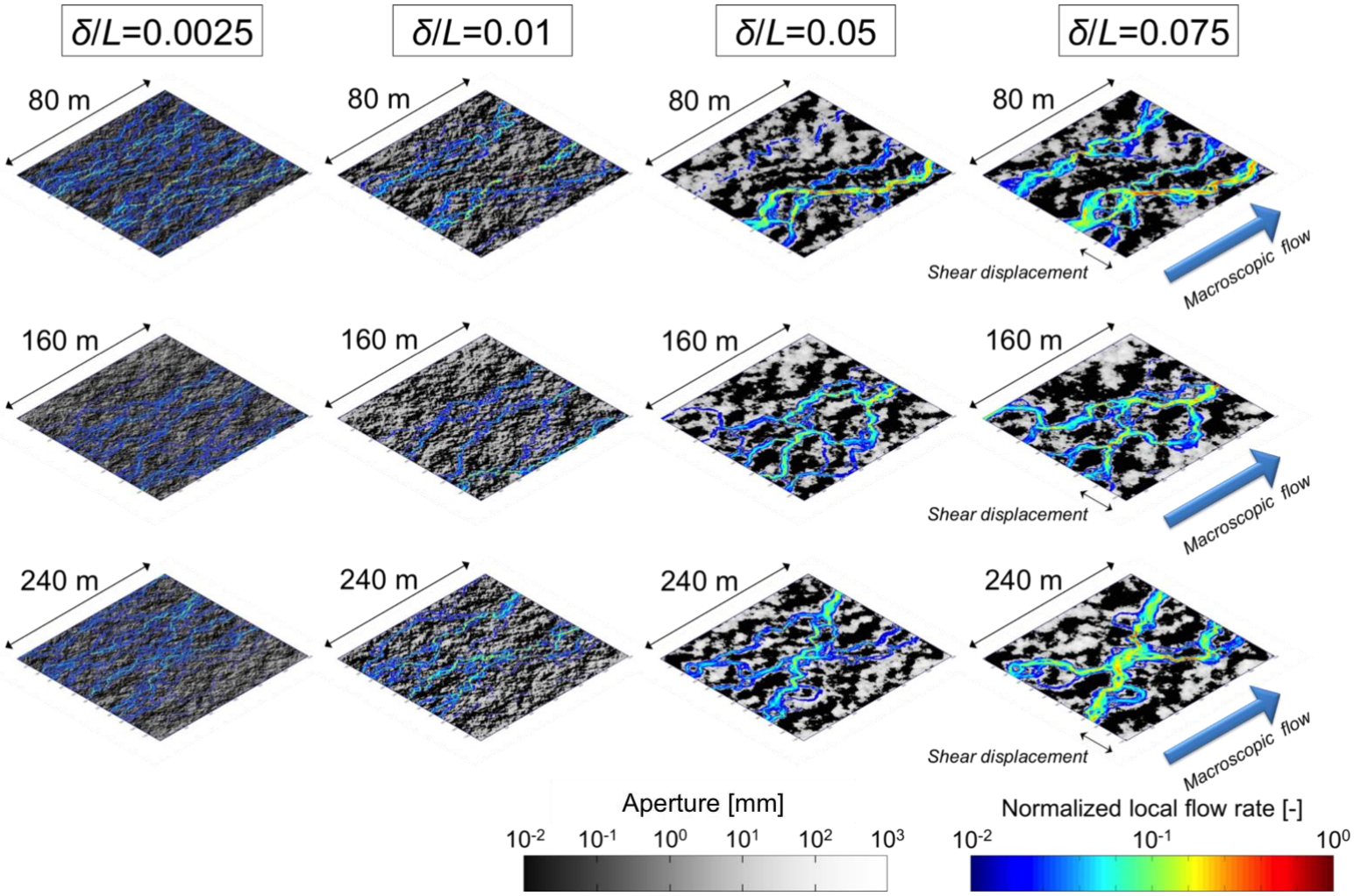

Figure 4-3. Representative results for the formation of preferential flow paths (i.e. channeling flow) within heterogeneous aperture distributions of numerically modeled fractures with various combinations of fracture scale and shear displacement under confining stress.

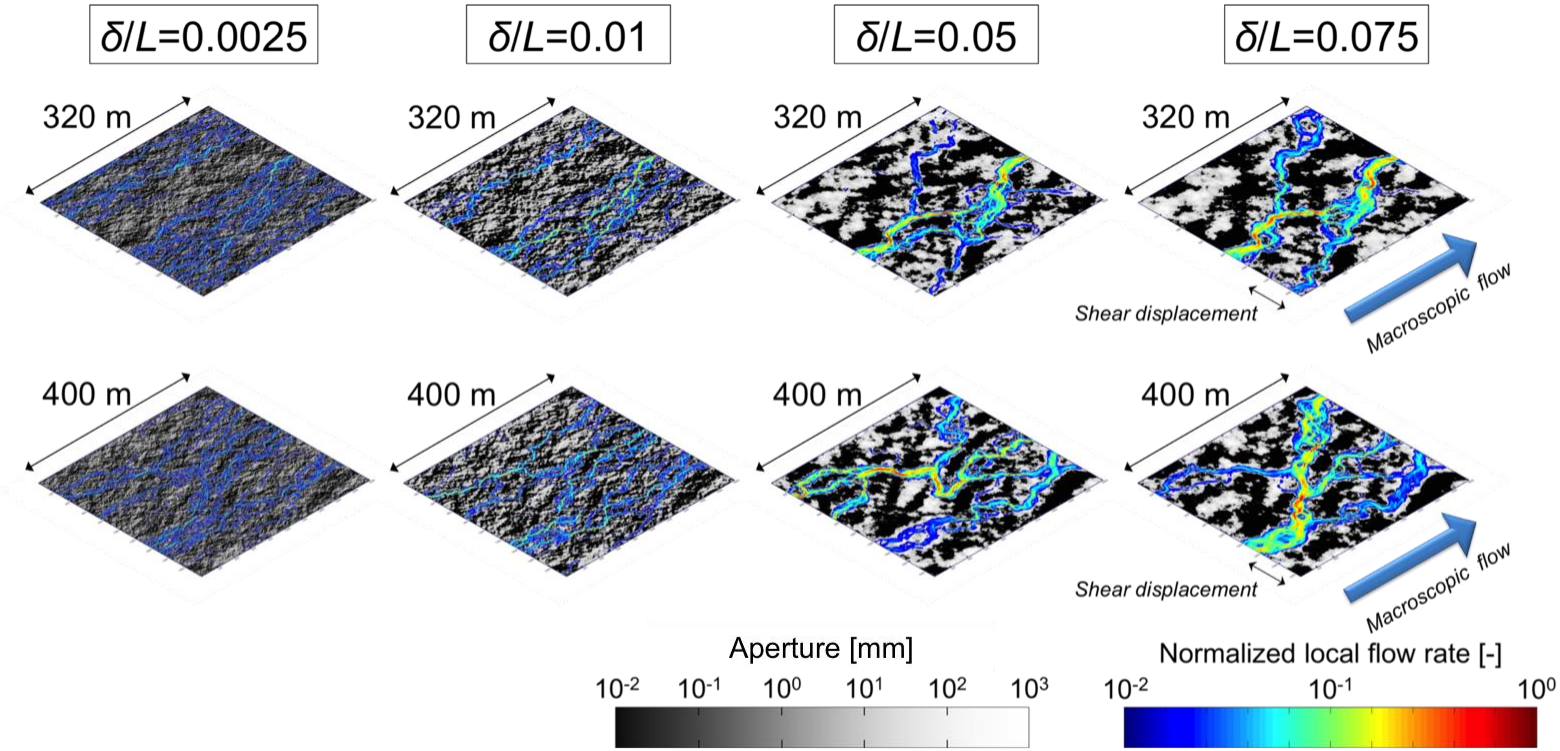

Figure 4-3. (*Continued*)

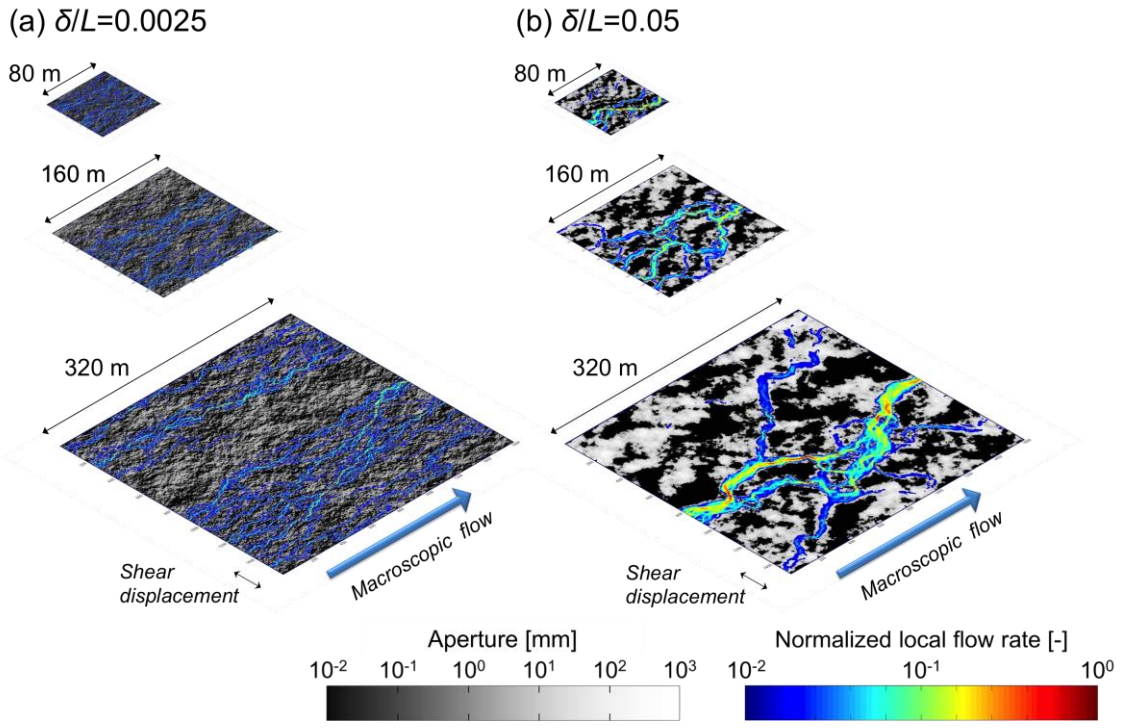

Figure 4-4. Scale dependent changes in the formation of preferential flow paths (i.e. channeling flow) within heterogeneous aperture distributions of rock fractures with (a) 0.25% shear displacement and (b) 5.0% shear displacement.

On the basis of these results, geometric and hydraulic characteristics of numerically modeled fractures are evaluated, and the results are summarized in Table 4-2. Note that the contact area of the numerically modeled fracture is set to 42% regardless of fracture scale or shear displacement in the present study.

First, the geometric characteristics of numerically modeled fractures are clarified. Figure 4-5 shows the change in the mean aperture with increasing shear displacement, δ/L, for the respective scale of fractures. Figure 4-6, in contrast, shows the change in the maximum aperture with increasing fracture scale for the respective shear displacement. The mean aperture and the maximum aperture increase with increasing shear displacement when the fracture scale is constant. The mean aperture and the maximum aperture also increase with increasing fracture scale when the shear displacement is constant. In Figure 4-6, the maximum aperture-fracture length relations of numerically modeled fractures are further compared with those of natural fractures (i.e. faults), which are reported in the literature [*Cowie and Scholz*, 1992; *Vermilye and*

Scholz, 1992; *Schlische et al.*, 1996]. According to the literature, the maximum aperture (m), e_{max}, and fracture length (m), L, is roughly related by the following formula:

$$e_{\max} = \alpha \cdot L, \tag{4-1}$$

where α is a pre-exponential factor which ranges from 0.001 to 0.1. It is clarified that the maximum aperture-fracture length relations of numerically modeled fractures are in good agreement with those of natural fractures. This fact indicates that the numerically created heterogeneous aperture distributions well represent the aperture distributions of natural subsurface fractures. The geometric standard deviation of apertures of subsurface rock fracture is approximately 2.9 regardless of fracture scale or shear displacement (see Table 4-2).

Then, the hydraulic characteristics of numerically modeled fractures are clarified. Figure 4-7a and 4-7b show the change in the fracture permeability and flow area with increasing shear displacement, δ/L, for the respective scale of fractures. The fracture permeability increases with increasing shear displacement when the fracture scale is constant. The fracture permeability also increases with increasing fracture scale when the shear displacement is constant. On the other hands, regardless of fracture scale, flow area first decreases and then moderately increases with increasing shear displacement. However, it is difficult to constrain the scale dependency in flow area for the fractures with constant shear displacement. As can be seen from Figure 4-7b, regardless of fracture scale or shear displacement, only the area of 5-25% of the entire fracture plane can contribute on the fluid flow, which is due to the occurrence of channeling flow within the fracture. This result also suggests that the noncontact areas with stagnant fluid correspond to 33-53% of the entire fracture plane, since the contact area is equivalent to 42%.

Table 4-2. Parameters characterizing the channeling flow within heterogeneous aperture distributions of numerically modeled fractures in field-scale.

Sampling interval [m]	Scale of fracture		Shear displacement (δ) [m]	δ/L [-]	Contact area [%]	Geometric mean [mm]	Geometric SD [-]	Maximum aperture [mm]	Fracture permeability [m^2]	Hydraulic aperture [mm]	Flow area [%]
	Width (w) [m]	Length (l) [m]									
0.1	79.9	80	0.1	0.00125	42	3.99	2.87	30.18	5.6×10^{-7}	2.58	22
	79.8	80	0.2	0.0025	42	6.70	2.89	51.97	1.1×10^{-6}	3.63	17
	79.6	80	0.4	0.005	42	10.68	2.90	78.66	2.3×10^{-6}	5.24	13
	79.2	80	0.8	0.01	42	16.62	2.91	129.55	5.7×10^{-6}	8.31	12
	78.4	80	1.6	0.02	42	25.20	2.91	174.56	1.2×10^{-5}	12.18	13
	76.0	80	4.0	0.05	42	41.01	2.88	240.50	4.7×10^{-5}	23.83	12
	74.0	80	6.0	0.075	42	49.68	2.90	288.07	6.7×10^{-5}	28.44	19
0.1	159.8	160	0.2	0.00125	42	7.35	2.89	62.82	1.1×10^{-6}	3.61	17
	159.6	160	0.4	0.0025	42	11.77	2.90	104.13	2.3×10^{-6}	5.24	11
	159.2	160	0.8	0.005	42	18.47	2.91	146.87	3.7×10^{-6}	6.71	10
	158.4	160	1.6	0.01	42	28.58	2.90	215.30	1.0×10^{-5}	11.11	9
	156.8	160	3.2	0.02	42	42.62	2.89	342.60	2.6×10^{-5}	17.60	11
	152.0	160	8.0	0.05	42	66.80	2.91	488.01	9.2×10^{-5}	33.16	14
	148.0	160	12.0	0.075	42	77.91	2.92	468.30	1.8×10^{-4}	46.59	15
0.2	239.8	240	0.2	0.00083	42	7.18	2.90	57.81	1.8×10^{-6}	4.71	22
	239.4	240	0.6	0.0025	42	15.93	2.91	128.93	5.6×10^{-6}	8.22	14
	238.8	240	1.2	0.005	42	25.17	2.91	203.10	1.2×10^{-5}	11.92	13
	237.6	240	2.4	0.01	42	38.76	2.92	296.87	2.7×10^{-5}	18.14	13
	235.2	240	4.8	0.02	42	58.20	2.91	403.35	5.6×10^{-5}	26.00	14
	228.0	240	12.0	0.05	42	95.88	2.89	769.76	2.3×10^{-4}	52.43	16
	222.0	240	18.0	0.075	42	116.51	2.90	850.84	2.8×10^{-4}	58.48	16
0.2	319.6	320	0.4	0.00125	42	11.14	2.90	99.90	2.9×10^{-6}	5.91	16
	319.2	320	0.8	0.0025	42	18.01	2.90	151.98	6.8×10^{-6}	9.01	14
	318.4	320	1.6	0.005	42	28.32	2.92	224.46	1.9×10^{-5}	15.10	12
	316.8	320	3.2	0.01	42	43.66	2.92	329.88	4.3×10^{-5}	22.67	11
	313.6	320	6.4	0.02	42	66.27	2.90	448.23	8.9×10^{-5}	32.76	9
	304.0	320	16.0	0.05	42	102.26	2.91	649.93	2.7×10^{-4}	56.47	12
	296.0	320	24.0	0.075	42	124.29	2.87	813.28	4.5×10^{-4}	73.55	13
0.2	399.6	400	0.4	0.001	42	11.47	2.90	95.85	3.2×10^{-6}	6.18	16
	399.0	400	1.0	0.0025	42	21.44	2.91	174.95	9.7×10^{-6}	10.79	13
	398.0	400	2.0	0.005	42	33.65	2.91	269.20	2.0×10^{-5}	15.58	11
	396.0	400	4.0	0.01	42	51.97	2.91	391.39	4.4×10^{-5}	23.06	14
	392.0	400	8.0	0.02	42	77.84	2.91	534.33	1.3×10^{-4}	39.98	16
	380.0	400	20.0	0.05	42	126.10	2.93	768.91	3.1×10^{-4}	60.77	16
	370.0	400	30.0	0.075	42	147.08	2.94	963.63	7.8×10-4	96.65	18

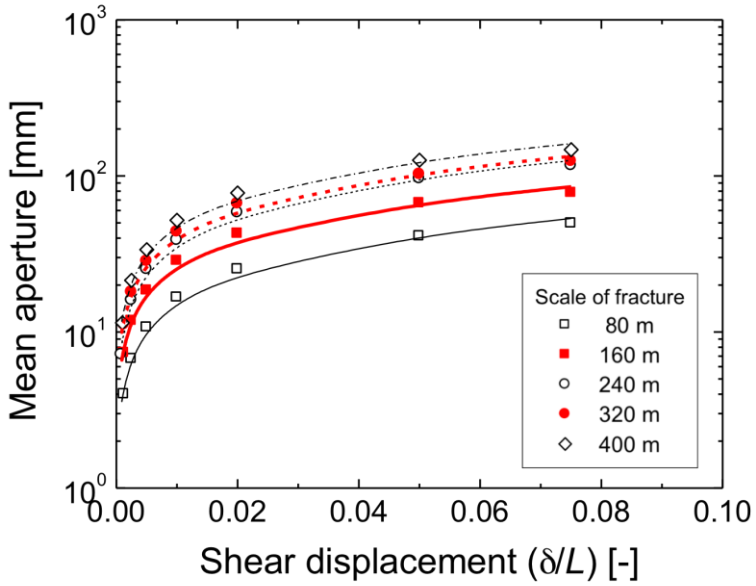

Figure 4-5. Mean apertures of numerically created heterogeneous aperture distributions of subsurface rock fractures with various combinations of fracture scale and shear displacement. Approximated curves by Eq. 4-2 are represented herein.

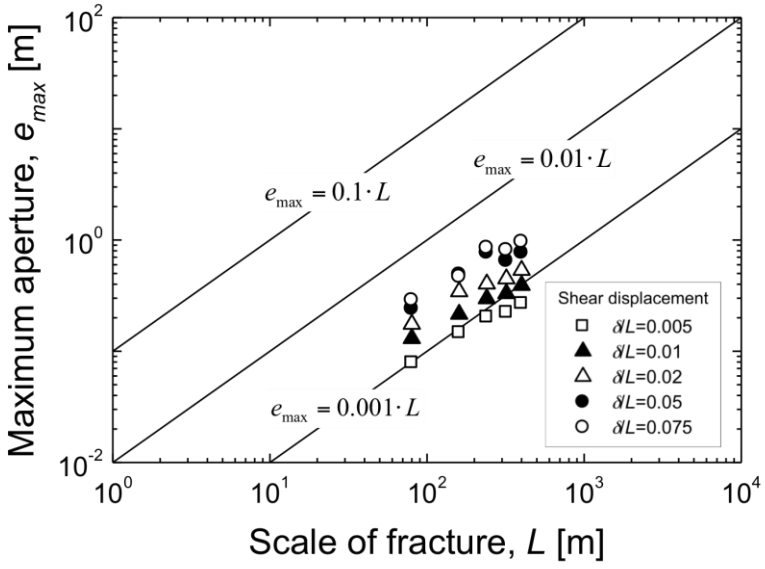

Figure 4-6. Comparison of the maximum aperture-fracture length relations between the predicted and the natural fractures. Linear curves shown in the figure correspond to the relations of the fault [*Cowie and Scholz*, 1992; *Vermilye and Scholz*, 1992; *Schultz et al.*, 2008].

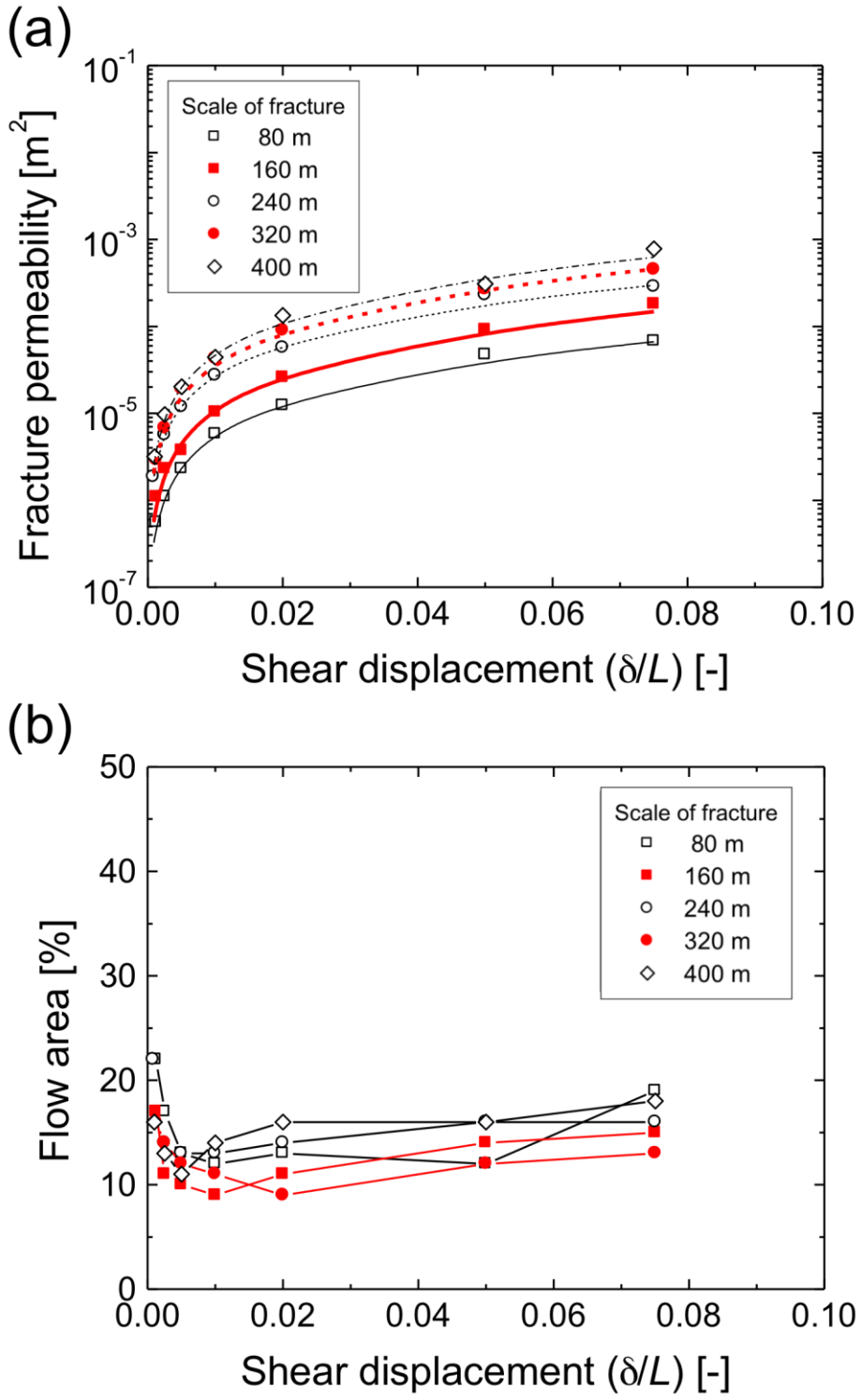

Figure 4-7. (a) Fracture permeability and (b) Flow area of numerically created heterogeneous aperture distributions of subsurface rock fractures with various combinations of fracture scale and shear displacement. Approximated curves by Eq. 4-3 are represented in Figure 4-7a.

4.3.2. Mean aperture and permeability of subsurface rock fracture formulated by fracture scale and shear displacement

On the basis of the above evaluations, geometric and hydraulic characteristics of subsurface rock fractures under confining stress are discussed as followings. Here, the confining stress from 30 MPa to 100 MPa, which corresponds to the stress of several thousands meters' depth, can be assumed in this study. Within the natural subsurface rock fractures, regardless of fracture scale or shear displacement, preferential flow paths are consistently formed (i.e. channeling flow). Due to the channeling flow, the flow area and the noncontact area with stagnant fluid within a rock fracture are approximately 5-25% and 33-53% of the entire fracture plane. In contrast, mean aperture and permeability of the fractures change systematically in response to both fracture scale and shear displacement (Figure 4-5, 4-7a). For the specified scale of fracture, the changes in mean aperture (mm), e_m, and fracture permeability (m^2), k, with shear displacement can be approximated by

$$e_m = \alpha_1 \cdot \left(\frac{\delta}{L}\right)^{\beta_1}, \tag{4-2}$$

$$k = \alpha_2 \cdot \left(\frac{\delta}{L}\right)^{\beta_2}, \tag{4-3}$$

where α_1 and α_2 are pre-exponential factors, and β_1 and β_2 are exponents. Approximated curves by Eqs. 4-2 and 4-3 are represented in Figures 4-5 and 4-7a, and α_1, α_2, β_1, and β_2 are calculated for each scale of fractures and are summarized in Table 4-3.

Table 4-3. Fitting parameters ofα_1, α_2, β_1, and β_2 determined for different scales of fractures.

Scale of fracture [m]	α_1 [mm]	β_1 [-]	α_2 [m^2]	β_2 [-]
80	2.62×10^{2}	0.61	1.5×10^{-3}	1.20
160	3.83×10^{2}	0.58	3.8×10^{-3}	1.25
240	6.18×10^{2}	0.62	5.9×10^{-3}	1.15
320	6.12×10^{2}	0.59	1.08×10^{-2}	1.22
400	7.49×10^{2}	0.59	1.55×10^{-2}	1.24

Based on Table 4-3, the changes in α_1, α_2, β_1, and β_2 with fracture scale are furthermore evaluated in Figure 4-7. It is revealed that α_1 and α_2 linearly increase with increasing fracture scale on a log-log plot whereas β_1 and β_2 are virtually scale independent. α_1 and α_2 are

respectively approximated by

$$\alpha_1 = (1.42 \times 10) \cdot L^{0.66} \tag{4-4}$$

$$\alpha_2 = (2.66 \times 10^{-6}) \cdot L^{1.43}. \tag{4-5}$$

Ensemble averages of β_1 and β_2 are, on the other hands, calculated to be 0.60 and 1.21.

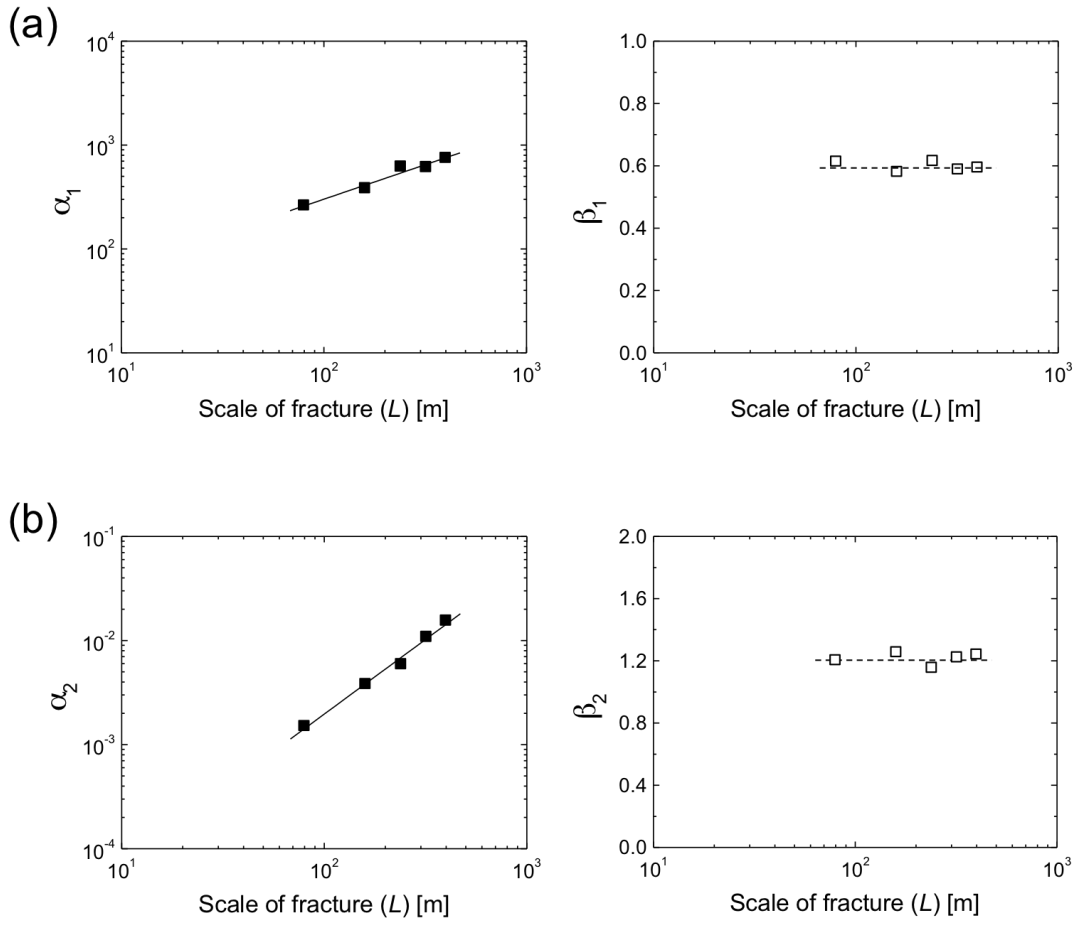

Figure 4-8. Changes in the fitting parameters, which constrain mean aperture (a) and permeability (b) of subsurface rock fractures.

By substituting Eq 4-4 into 4-2, mean aperture (mm), e_m, can be rearranged to yield

$$e_{mean} = (1.42 \times 10) \cdot L^{0.66} \cdot \left(\frac{\delta}{L}\right)^{0.60}. \tag{4-6}$$

In the same manner, by substituting Eq 4-5 into 4-3, fracture permeability (m^2), k, can be rearranged to yield

$$k = (2.66 \times 10^{1.43}) \cdot L^{1.43} \cdot \left(\frac{\delta}{L} \right)^{1.21} . \quad (4\text{-}7)$$

Thus, the mean aperture and the permeability of subsurface rock fracture are successfully formulated by two parameters, fracture scale and shear displacement. By applying these equations, fluid flow characteristics of subsurface rock fractures can be revealed for a wide range of conditions for fracture scale, shear displacement, and confining stress (30 – 100 MPa).

In order to highlight the changes of the mean aperture and the permeability with increasing shear displacement, constant values of the fracture scales are first employed. Fracture scales (m), L, of 0.1, 0.2, 0.4, 1.0, 2.0, 4.0, 10, 20, 40, 100, 200, 400, and 1000 are selected herein, and these values are substituted into Eqs. 4-6 and 4-7. As a result, the changes of the mean aperture and the permeability with increasing shear displacement are plotted in Figures 4-9a and 4-9b, where the fracture scale varies. The increases in e_m and k are drastic with increasing the shear displacement from 0 to 0.02, whereas these increases are gradual with increasing the shear displacement from 0.02 to 0.1. In the present study, the maximum value of shear displacement is set to 0.1.

Additionally, the mean aperture and permeability of the real rock fractures are plotted together in Figure 4-9a and 4-9b for comparison. The parameters for the fracture of 0.1×0.15 m^2 with 5 mm shear displacement (δ/L = 0.05) are plotted with solid square symbol, whereas the parameters for the fracture of 0.2×0.3 m^2 with 5 mm shear displacement (δ/L = 0.025) are plotted with open square symbol. For these rectangular-shaped fractures, the fracture scale, L, is represented by the short side length of fracture. Note that these parameters of real rock fractures are obtained in Chapter Ⅲ (see Table 3-1). It is clarified that the mean aperture and permeability predicted by Eqs 4-6 and 4-7 are in good agreement with those of the real laboratory scale fractures. Thus, the applicabilities of Eqs 4-6 and 4-7 are supported by these results.

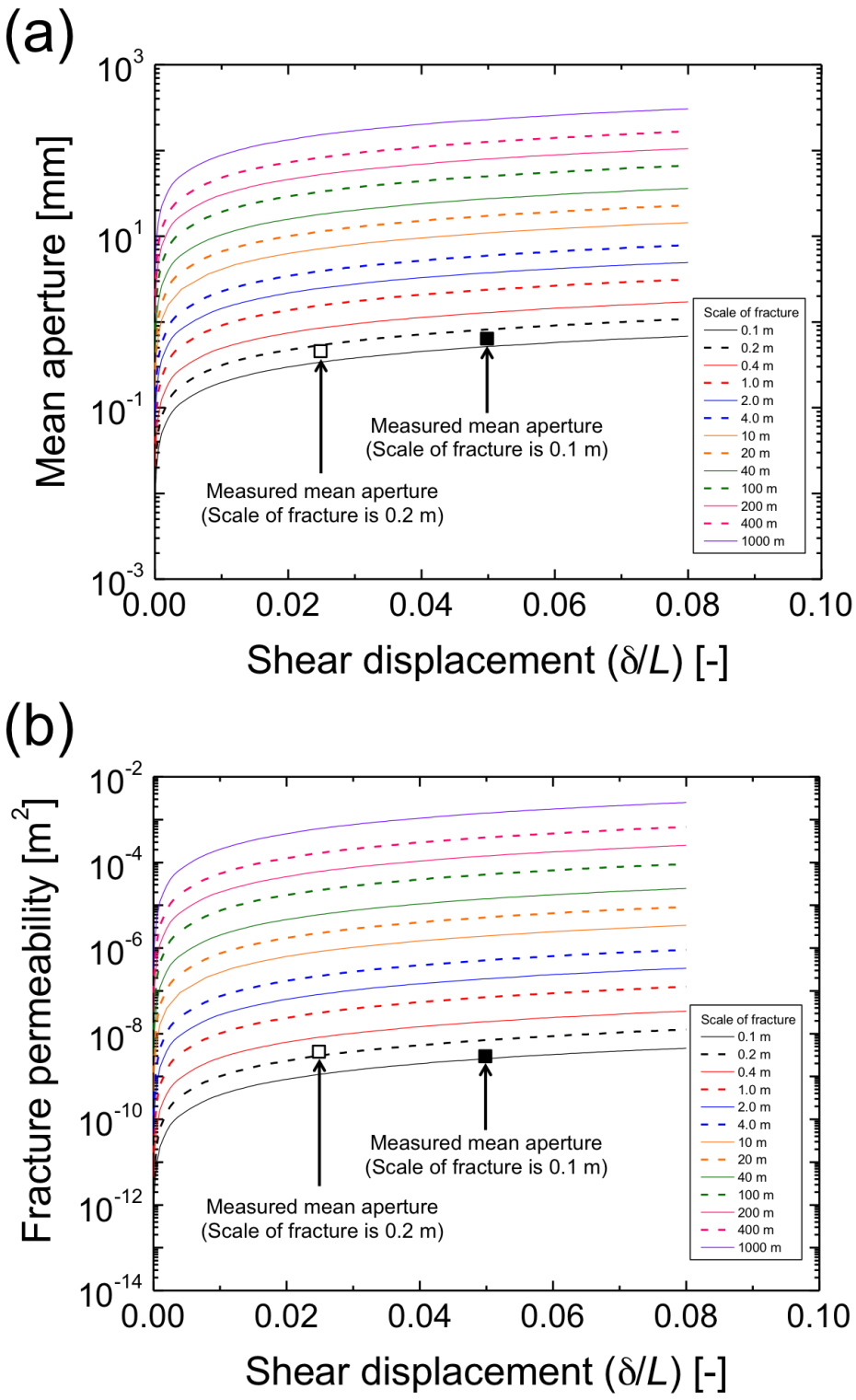

Figure 4-9. Changes in (a) mean aperture and (b) permeability of subsurface rock fractures with increasing shear displacement, where fracture scale varies.

Subsequently, to highlight the changes of the mean aperture and the permeability with increasing fracture scale, constant values of the shear displacement are employed. Here, it is widely acceptable that the shear displacement of natural fault linearly increases with increase in the fracture scale [*Kanamori and Anderson*, 1975; *Scholz*, 2002]. Shear displacement, δ/L, of 0.0005 (0.05%), 0.001 (0.1%), 0.005 (0.5%), 0.01 (1%), and 0.05 (5%) are selected in this study, and these values are substituted into Eqs. 4-6 and 4-7. As a result, the changes of the mean aperture and the permeability with increasing fracture scale are plotted in Figures 4-10a and 4-10b, where the shear displacement varies. When the constant shear displacement is assumed, e_m and k linearly increase with increasing fracture scale on a log-log plot.

In this study, the geometric and hydraulic characteristics of subsurface fractures are revealed for a wide range of conditions for fracture scale, shear displacement, and confining stress (i.e. universal modeling). In developing the universal modeling, although the production of gouges and the deformation of rock fracture surfaces during shear displacement may have some impact on the heterogeneous aperture distributions [*Scholz*, 2002; *Jaeger et al.*, 2007], the effects of these mechanisms are ignored in this study. Due to these mechanisms, it is expected that the mean aperture and permeability of the rock fracture are somewhat smaller than those predicted by Eqs 4-6 and 4-7. In the future work, it will be examined whether these effects should be introduced in the universal modeling modeling of fracture flow characteristics or not.

Finally, the applicability of the universal modeling of fracture flow characteristics is discussed. Owing to the universal modeling, we will specifically reach a new insight into the permeability evolutions of rock fractures (natural faults) caused by earthquakes. For instance, on the basis of Figure 4-9b, even if shear displacement of a fault with a fracture scale of 1,000 m increases from 0.01 (1%) to 0.03 (3%) as a result of repeating earthquake (or possible magnitude of earthquake), the permeability of the fracture doesn't change drastically and the change is expected to be one order of magnitude at the most. Thus, we may quantitatively predict how much the fracture permeability is evolved in the case that a specific magnitude of earthquake occurs in subsurface rock fracture of a specific scale.

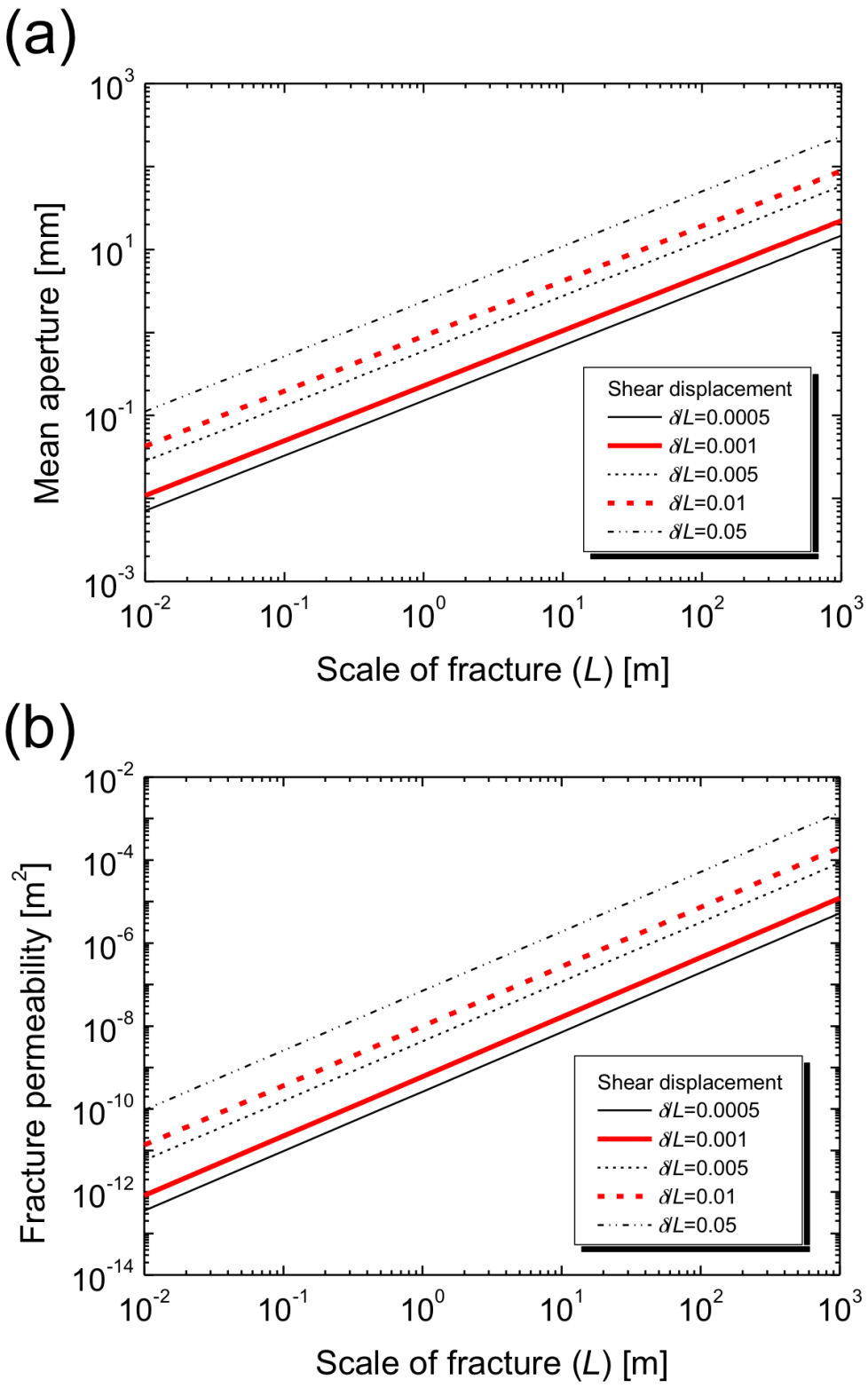

Figure 4-10. Changes in (a) mean aperture and (b) permeability of subsurface rock fractures with increasing fracture scale, where shear displacement varies.

4.4. Conclusion

Aperture distributions and fluid flows are numerically determined for rock fractures with various combination of fracture scale and shear displacement, and their geometric and hydraulic characteristics are evaluated systematically. Through the evaluations, fluid flow characteristics of subsurface rock fractures under confining stress (up to ~ 100 MPa) are revealed as followings; flow area within a fracture plane is limited to 5-25% regardless of fracture scale (m), l, or shear displacement (m), δ, since preferential flow paths are consistently formed within subsurface rock fractures (i.e. channeling flow). Moreover, mean aperture (mm), e_m, and permeability (m^2), k, of rock fractures are formulated as

$$e_{mean} = (1.42 \times 10) \cdot L^{0.66} \cdot \left(\frac{\delta}{L} \right)^{0.60}$$

$$k = (2.66 \times 10^{1.43}) \cdot L^{1.43} \cdot \left(\frac{\delta}{L} \right)^{1.21},$$

which can reproduce the mean apertures and permeabilities of real fractures, although the effects of gouge productions or deformation of fracture surfaces during shear displacement should be examined in the future work.

These achievements enable us to create realistic discrete fracture network (DFN) models of a fractured reservoir for GeoFlow simulation. Additionally, these results are also fundamentals to reach a new insight for the permeability evolutions of subsurface rock fractures (natural faults) caused by earthquakes. This also link to the evaluation of the impact of fracture stimulations in a fractured reservoir.

Chapter Ⅴ

Modeling of three dimensional channeling flow in a fractured reservoir with GeoFlow

5.1. Introduction

In Chapter Ⅳ, fluid flow characteristics of subsurface rock fractures are revealed for a wide range of conditions for fracture scale, shear displacement, and confining stress. Furthermore, the universal modeling of fluid flow characteristics through subsurface rock fractures are suggested, where mean aperture, permeability, and flow area of subsurface rock fractures are constrained by shear displacement and fracture scale.

Considering these achievements, realistic discrete fracture network (DFN) models, where heterogeneous aperture distributions are given for individual fractures under confining stress depending on their scale and shear displacement, can be created for an actual fractured reservoirs. In fluid flow analysis for such DFN models, the formation of three dimensional (3-D) preferential flow paths (i.e., 3-D channeling flow) is properly considered. Analyses of the 3-D channeling flow in fractured reservoir are realized by GeoFlow [*Ishibashi et al.*, 2012].

In this study, the Yufutsu oil/gas field (Hokkaido, Japan) is modeled. This field is suitable for discussing the characteristics and impact of 3-D channeling flow in a fractured reservoir. As described later herein, four wells were drilled in this field and approximately three orders of magnitude difference in productivity was observed between two of these four wells. Although the cause of the huge difference in well productivity has been examined by analyzing fluid flow for the highly reliable conventional DFN models, this observation has never been reproduced and the cause of this huge difference is still unexplained [*Tamagawa et al.*, 2010; *Tamagawa et al.*, 2012]. It is considered that the discrepancy between the observation and the model is caused by the fact that the occurrence of 3-D channeling flow in an actual fractured reservoir is ignored in the modeling, where the fractures were represented by pairs of parallel smooth plates with unique apertures.

Thus, in this chapter, realistic DFN models, where heterogeneous aperture distributions are given for individual fractures depending on their scale and shear displacement under confining stress, are created for the Yufutsu oil/gas field. Then, the characteristics and impact of 3-D

channeling flow in a fractured reservoir are discussed through simulating fluid flows within the reservoir by GeoFlow.

5.2. Reviews for three orders of magnitude difference in well productivity observed in a fractured reservoir (the Yufutsu oil/gas field)

As mentioned above, the Yufutsu oil/gas field is modeled in the present study. Through the research review for the Yufutsu oil/gas field, it is clarified that this field is suitable for discussing the characteristics and impact of 3-D channeling flow in a fractured reservoir.

The Yufutsu oil/gas field, which is fractured basement reservoir, is located in the southern Ishikari Plain, Hokkaido Island, Japan (Figure 5-1a). This field was discovered in 1989 and is one of the largest gas fields in Japan. Gas production started in 1996, and the cumulative gas production was approximately 60 bcf at the end of 2006. The permeability development of the reservoir is inferred to be controlled by the shear dilation mechanism for the mega-fractures, which have apertures of more than 5 cm [*Kumano et al.*, 2012].

The geological section of the Yufutsu oil/gas field is shown in Figure 5-1b. Bedrock for this field is Lower Cretaceous granitic plutons, which is covered by Paleogene and Neogene siliciclastic sediments of approximately 4,000 meters in thickness. Oil and gas are trapped within rock fractures (faults) at Lower Cretaceous granitic plutons and overlaying Eocene conglomerate layer. At present, this field is located in the frontal area of a thrust deformation front, which has propagated westward from the Hidaka Mountain Range. Due to this strong tectonic contraction, it is inferred that the structures of the Yufutsu field have been reactivated [*Kurita and Yokoi*, 2000; *Kuniyasu and Yamada*, 2004].

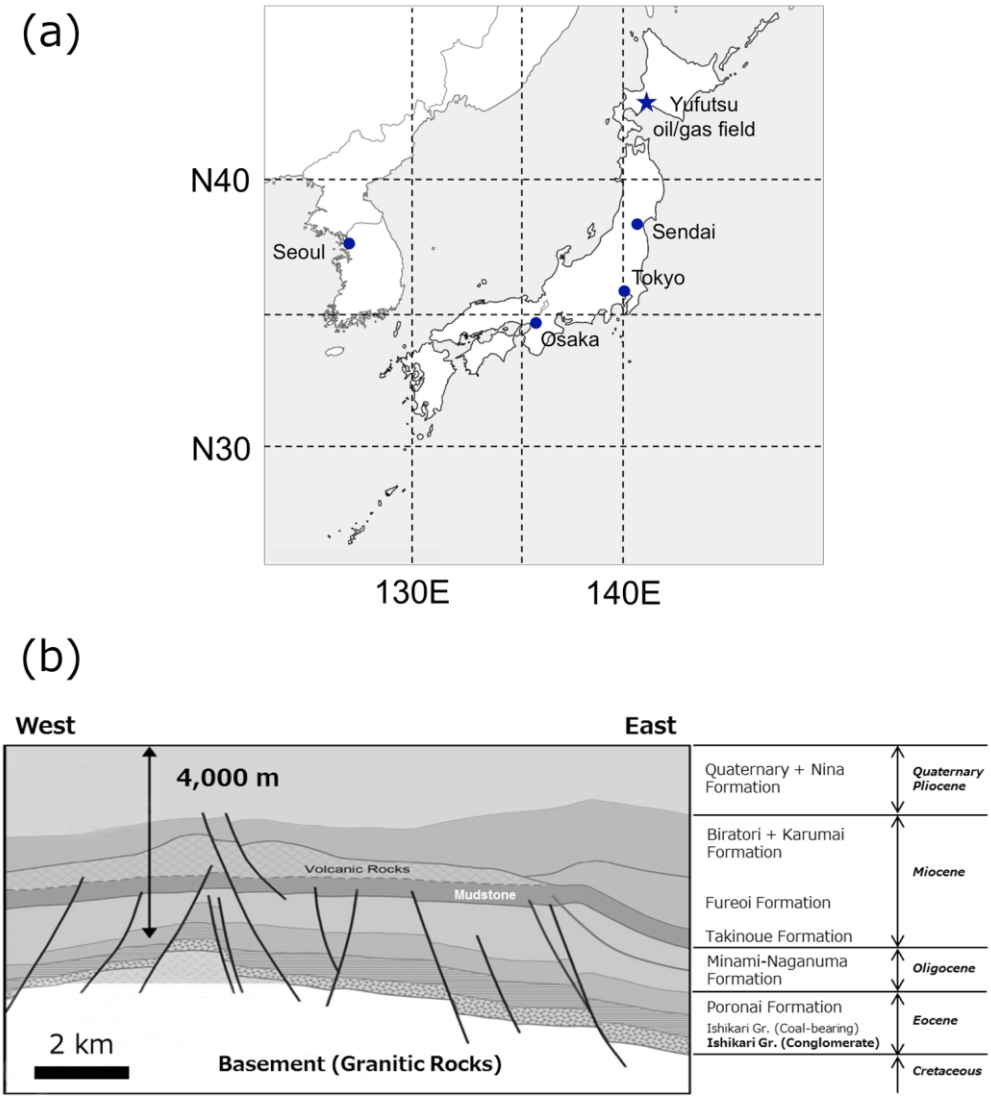

Figure 5-1. (a) Index map showing the location of Yufutsu oil/gas field, and (b) Geological cross section of the Yufutsu field. Gr = Group.

For an area of 2.4 km (East-West) × 2.6 km (North-South) within the central part of the Yufutsu field, four wells (Well A, B, C, and D) were drilled at a spacing of approximately several hundred meters (Figure 5-2a). Well A is a nearly vertical well with an inclination of 14°, and is the most productive well in the Yufutsu field. Well B is also a nearly vertical well with an inclination of 16°, but its productivity is significantly low. The difference in productivity between Well A and B is approximately three orders of magnitude. Well C is a deviated well with an inclination of 39°, and shows the second highest productivity in this field. Well D is also

a deviated well with an inclination of 46°, and shows no gas production. Such a large variation in well productivity indicates the fact that the fracture system is highly heterogeneous in the field.

In order to reveal the heterogeneous geometry of fracture system for the Yufutsu field, 3-D surface seismic data, which tell us a fracture distribution associated with faulting, have been acquired for the field. Figures 5-2b and 5-2c show examples for time slices of the seismic amplitude and the seismic variance, which coincide with the level of the central depth of the reservoir interval, respectively. Since the seismic data for the field are originally chaotic due to the reduction of the signal-to-noise ratio and the irregular distribution of seismic source and receiver arrays, the location of subtle faults within the data should be identified through manual fault interpretations or computational image processing algorithms. Figure 5-2d shows an example for the time slice of fault-extraction processed data, where the locations of faults are highlighted [*Tamagawa et al.*, 2010].

Additionally, various kinds of data have been collected for a long time for the same area in the Yufutus field. For instance, by analyzing mineral precipitations within the core, the insight in the history of fracture development is acquired [*Yanagimoto and Iijima*, 2003]. Wellbore imaging data are a principal source of observation for understanding the fracture system as well as the in-situ stress field. By analyzing the wellbore imaging data, it is clarified that the general current stress state of the Yufutsu field is a strike-slip-faulting stress regime, where the overall trend of the maximum principal stress direction is northeast-southwest. Microseismic event data are also acquired during a massive hydraulic injection for Well B, which are useful in mapping the fracture systems and/or fault zones spatially-extended around a wellbore. By analyzing the observed microseismic events, fracture system within an area of 700 m × 300 m around Well B is successfully delineated with estimated location errors of less than 20 m [*Tezuka and Tamagawa,* 2004]. Note that the hypocenter distributions for some of microseismic events are mapped with green dots in Figures 5-2b, 5-2c, and 5-2d.

In this way, comprehensive quality data sets (well productivity data, 3-D seismic data, core and wellbore imaging data, and microseismic data) have been compiled for the Yufutsu field, which have enabled *Tamagawa et al*. [2012] to develop a novel calibration scheme of

seismic-attributes derived from 3-D seismic data by coupling with microseismic data and in-situ stress data. Owing to the novel scheme, highly reliable distribution of fractures can be revealed and the active fractures under a strike-slip faulting stress regime (i.e. critically-stressed fractures), which satisfy the Mohr-Coulomb failure criterion and have very high permeability, are also delineated for the Yufutsu field.

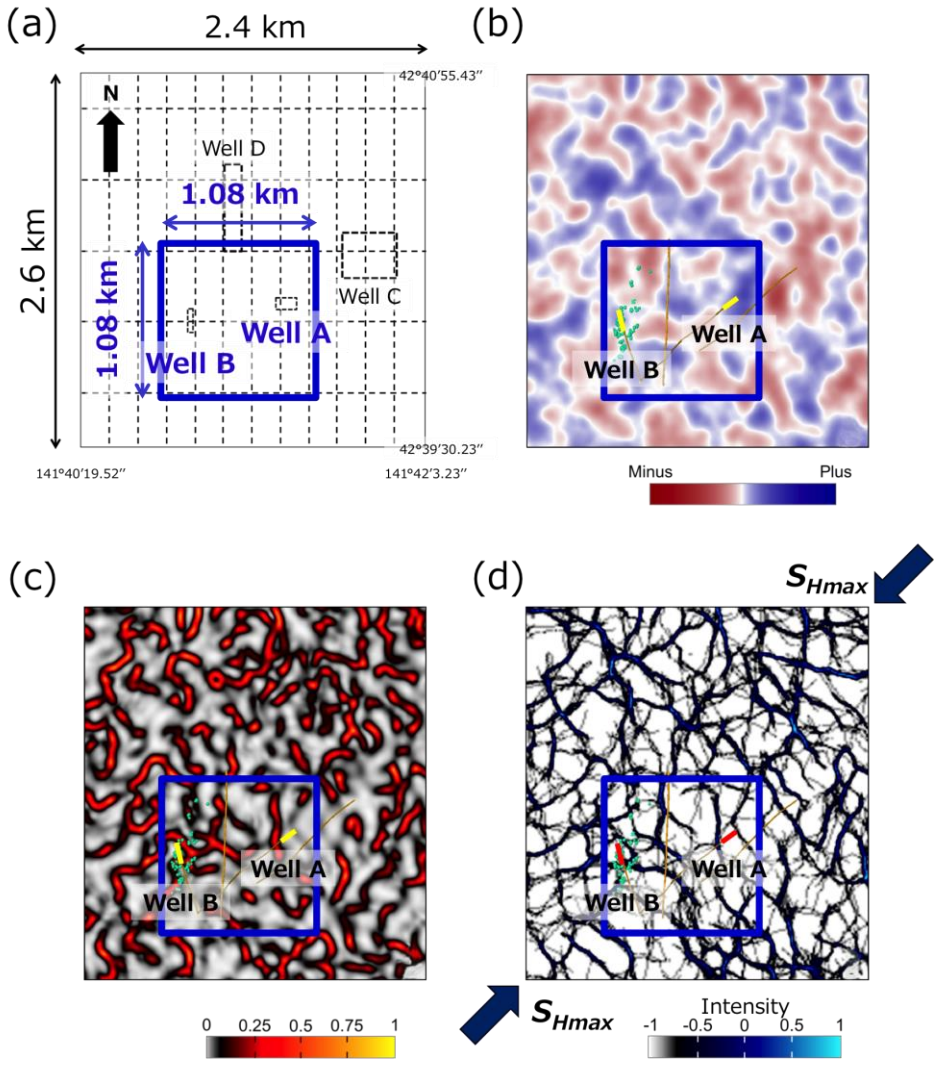

Figure 5-2. (a) Locations of four wells (Well A, B, C, and D), which are enclosed with thin dashed lines, in the Yufutsu oil/gas field. Study area of GeoFlow simulation in the present study is enclosed with bold line. Over the area, 3-D surface seismic data, which are shown as (b) seismic amplitude and (c) variance of seismic amplitude, are acquired. Furthermore, (d) fault-extraction processed data is also obtained based on the seismic data.

Based on these investigations, highly reliable DFN models for the fracture distributions, where permeabilities of critically-stressed fractures are much higher than those of noncritically-stressed fractures due to shear dilation mechanism, can be created for the prescribed regime of 2.4 km (East-West) × 2.6 km (North-South) × 1.5 km (Depth) of the Yufutsu field. However, although the fluid flow is analyzed for the DFN models, the huge difference in well productivity, which is indeed observed for the field, has never been reproduced and the cause of the huge difference remains unclear [*Tamagawa et al.*, 2010; *Tamagawa et al.*, 2012]. Here, the occurrence of 3-D channeling flow in a fractured reservoir is ignored in the past modeling, which can cause the discrepancy between the observation and the model. This fact inspires the following idea; the huge difference in well productivity can be reproduced if the occurrence of 3-D channeling flow is considered adequately. Thus, this field is suitable for discussing the characteristics and impact of 3-D channeling flow in a fractured reservoir.

5.3. Method

5.3.1. Modeling of a fractured reservoir

An area of 1,080 m (East-West) × 1,080 m (North-South) × 1,080 m (Depth) in the Yufutsu field, which is shown in Figure 5-2 with bold lines, is focused in the present study. This area includes Well A (high productivity) and Well B (low productivity), and the difference in productivity of these two wells is approximately three orders of magnitude. Therefore, the characteristics and impact of 3-D channeling flow in a fractured reservoir can be discussed through the GeoFlow simulations of this area.

In modeling discrete fracture network (DFN) for the Yufutsu field, the present study assumes that the fracture system is simply developed as follows. First, a number of fractures are generated within the rock mass by various reasons such as cooling of the rock mass, change in the stress field, and so on. Then, the fractured rock mass is placed in the current stress state of a strike-slip-faulting. According to the stress state, rock fractures with the specific directions, which satisfy the Mohr-Coulomb failure criterion, are sheared. For the fractures with shear displacement, it is assumed that shear displacement of a fracture linearly increases with

increasing fracture scale (i.e. a constant ratio of shear displacement to fracture length) [*Kanamori and Anderson*, 1975].

Discrete fracture networks are created on the specified area, where the permeability of rock matrix is set to 10^{-19} m^2, which is equivalent to the matrix permeability of granite [*Takahashi et al.*, 1990]. Rock fractures are represented by squares of 18 different scales (44, 62, 80, 98, 115, 133, 151, 168, 186, 204, 222, 239, 257, 275, 293, 310, 328, and 346 m on a side), and approximately 15,000 fractures are distributed in the analytical domain (see Appendix 5-A). The numbers of fractures can be determined for the respective scales of fractures, since the fracture length (m), l, which is defined as a side length of a square, and the cumulative frequency of fracture (m^{-3}), N, are related by (modified from *Matsuura et al.* [2003] and *Tamagawa et al.* [2010] by considering the difference in the shape of fracture)

$$N = 0.346 \times \left(\frac{l}{\sqrt{\pi}} \right)^{-3.15} . \tag{5-1}$$

The relationship between cumulative frequency of fracture and fracture length is plotted in Figure 5-3a. Center coordinates and orientations of the individual fractures are given so that they coincide with those determined in *Tamagawa et al.* [2010]. Then, 15 kinds of stochastic equivalent discrete fracture networks, where the center coordinates and orientations of the individual fractures are different, are prepared. This is because DFN models are recognized to be best treated in a stochastic framework by considering Monte Carlo analyses based on multiple realizations. One example of the created DFN for the Yufutsu field is shown in Figure 5-3b, where x-, y-, z-axes are mounted in east-west, north-south, deep-shallow directions, respectively. Such correspondences for the axes are common in the following figures. Furthermore, the ratio of volume containing fractures to the total volume of the analytical domain is approximately 25%.

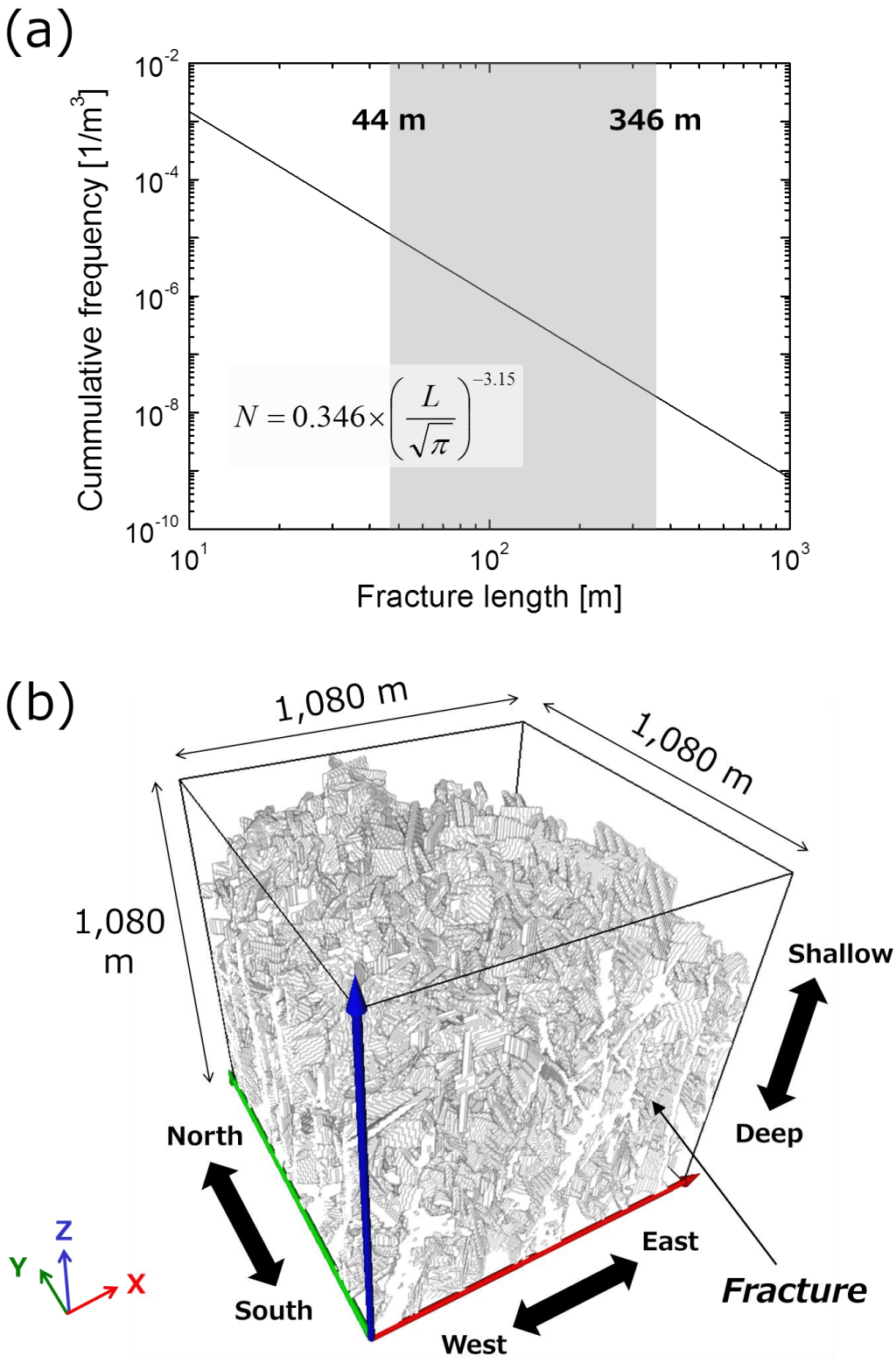

Figure 5-3. (a) Relationship between cumulative frequency of fractures and fracture length and (b) an example of created DFN for the Yufutsu oil/gas field.

In the present study, two different models, “GeoFlow model” and “Conventional DFN model”, are used for analyzing fluid flow in the fractured reservoir. Heterogeneous aperture distributions are considered in response to the fracture scale and shear displacement in GeoFlow model, whereas fractures are represented by pairs of parallel smooth plates with scale-dependent unique apertures in Conventional DFN model. Between these two models, fracture distributions (fracture scales, center coordinates, and orientations of the individual fractures) are the same. Moreover, permeabilities (or hydraulic apertures) of the corresponding fractures are also the same. Consequently, by comparing the result of GeoFlow model with the result of Conventional DFN model, the characteristics and impact of 3-D channeling flow can be discussed.

Specifically, the detail of creating GeoFlow model of the Yufutusu field is explained herein. In the GeoFlow model, heterogeneous aperture distributions for rock fractures are determined with the method developed in Chapter Ⅲ. In this method, a pair of fractal fracture surfaces is placed in contact so that the fracture has the scale-independent contact area. When this method is applied, surface geometries of the fractures are numerically created by using the parameters, such as fractal dimension and standard deviation for the surface height, calculated for the tensile fracture of granite of laboratory scale. As the grid spacing in the *X*- and *Y*-directions is set to 1 m for the surfaces, the dimension of fracture element, which is defined in Chapter Ⅱ, is 1 m × 1 m. To simulate the original preferential flow paths within a rock fracture adequately, the length of fracture element should be set smaller than fiftieth part of the fracture length, which is preliminary confirmed. Since this condition is satisfied in the present study, channeling flow in a rock fracture can be represented accurately.

In the GeoFlow model of the Yufutsu field, critically-stressed fractures, which are expected to experience multiple slips, can be distinguished from noncritically-stressed fractures by considering the current stress state, so heterogeneous aperture distributions are separately given for these fractures. In other words, the GeoFlow model consists of 36 kinds of fractures with various combinations of fracture scale and shear displacement. For the noncritically-stressed fractures, a ratio of shear displacement to fracture length (“shear displacement” hereafter) is set equal to 5×10^{-5} (0.005%), whose permeabilities are plotted with solid triangles in Figure 5-4. Moreover, mean apertures range from 0.4 mm to 1.8 mm for these fractures. Considering that

the noncritically-stressed fractures can have aperture of up to 50 mm [*Kumano et al.*, 2012], a relatively small value of 5×10^{-5} (0.005% of fracture length) is validated. In contrast, for the critically-stressed fractures, it is significantly difficult to determine a shear displacement uniquely. Therefore, the shear displacement for the critically-stressed fractures is treated as a fitting parameter, and the heterogeneous aperture distributions of fractures are determined in the case that the shear displacement is set to 1×10^{-3} (0.1%), 4×10^{-3} (0.4%), 2×10^{-2} (2%), and 4×10^{-2} (4%). Here, the directions of shear displacement are preliminary constrained by the overall trend of the maximum principal stress direction in the Yufutus field. For each settings of shear displacement, fracture permeabilities are plotted in Figure 5-4.

Furthermore, even though the fracture scale and shear displacement are specified, the heterogeneous aperture distributions of fracture varies depending on a series of uniform random number, R_1, which is defined in Eq (A8) in Chapter Ⅲ. However, the fluid flow characteristics of a fractured reservoir can be evaluated by using representative aperture distributions, since these characteristics don't vary depending on the aperture distributions of individual fractures. This fact is preliminary confirmed (Appendix 5-B).

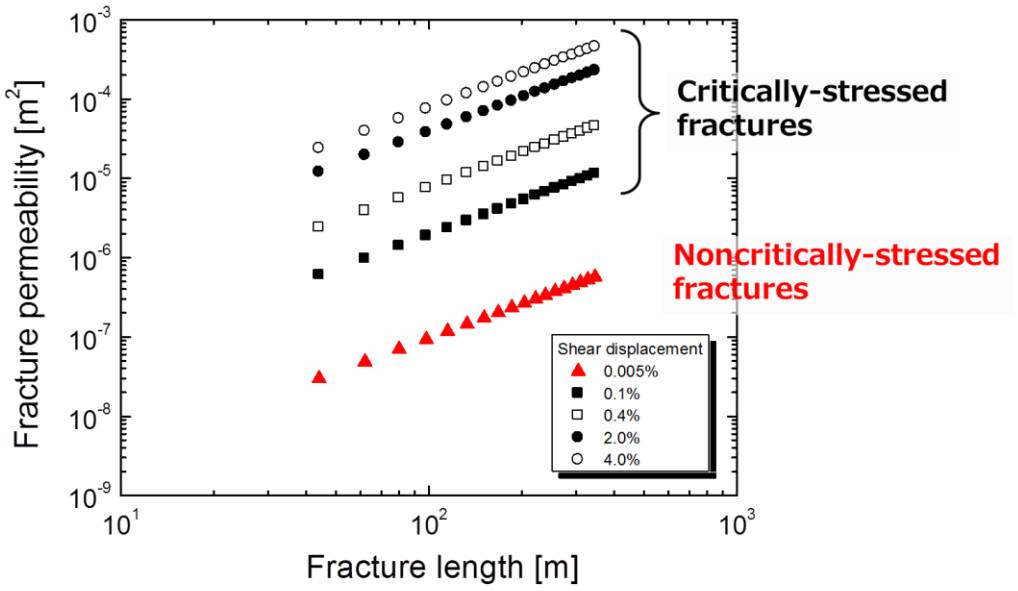

Figure 5-4. Relationship between fracture permeability and fracture length for both noncritically-stressed fractures and critically-stressed fractures.

A shear displacement for critically-stressed fractures is fist set to 4×10^{-3} (0.4%). This model imitates the model created by *Tamagawa et al.* [2010] in that permeabilities of critically-stressed fractures are 100 times higher than those of noncritically-stressed fracture when the scales of these fractures are the same. However, as described later herein, this model can never reproduce the three orders of magnitude difference in well productivity observed at the Yufutsu field. This is maybe due to the fact that the shear displacement of 4×10^{-3} (0.4%) is inadequate in the model. With this in mind, a shear displacement for critically-stressed fractures is varied from 1×10^{-3} (0.1%) to 4×10^{-2} (4%) to reproduce the observation.

In order to analyze fluid flow within a fractured reservoir, the discrete fracture networks are converted into the equivalent permeability continua, which is common for both GeoFlow model and Conventinal DFN model. The analytical domain of 1,080 m × 1,080 m × 1,080 m is first divided into a total of 5,832,000 matrix elements, which is defined in Chapter Ⅱ, with the dimension of 6 m × 6 m × 6 m. Then, equivalent permeabilities are calculated at all matrix element interfaces. The detail of the conversion processes is explained in Chapter Ⅱ, and one example of permeability map for the equivalent permeability continua of the Yufutsu field is shown in Figure 5-5, where highly permeable zone is shown with colors. It is preliminary confirmed that fluid flow through a specific fracture simulated by 2-D Reynolds equation is adequately reproduced in 3-D GeoFlow simulation with preserving the characteristics of the original aperture distribution, when the length of matrix element is smaller than 6-times the length of fracture element. Considering that the lengths of fracture element and matrix element are 1 m and 6 m respectively, 3-D channeling flow within a fractured reservoir can modeled successfully in the present study. Parameter set for the fluid flow simulations of the Yufutsu oil/gas field is summarized in Table 5-1.

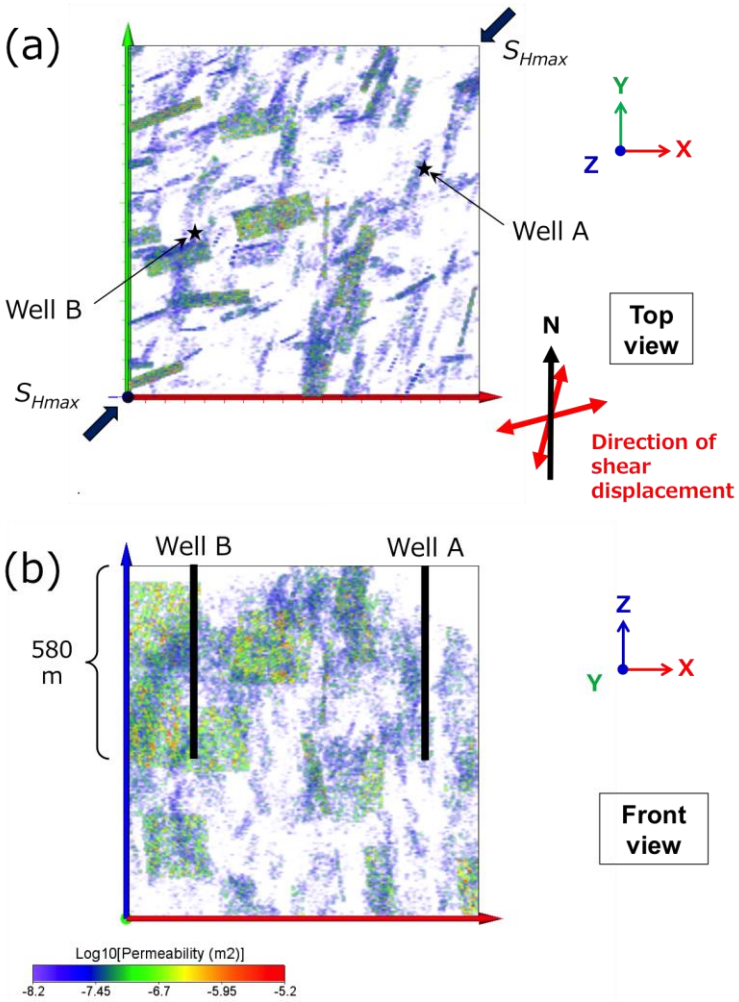

Figure 5-5. An example of permeability map for the equivalent permeability continuum of the Yufutsu oil/gas field evaluated in GeoFlow model. ((a) Top view and (b) Front view)

Table 5-1. Parameter set for the fluid flow simulations of the Yufutsu oil/gas field.

Analytical domain	1,080 m × 1,080 m × 1,080 m
Minimum fracture	44 m × 44 m
Maximum fracture	346 m × 346 m
Number of fracture	Approximately 15,000
Fracture element	1 m × 1 m
Matrix element	6 m × 6 m × 6 m
Number of matrix element	180 × 180 × 180 (=5,832,000)
Shear displacement of noncritically-stressed fractures	0.005% of fracture length
Shear displacement of critically-stressed fractures	0.1-4.0% of fracture length

5.3.2. Analysis of fluid flow in a fractured reservoir with GeoFlow

For the equivalent permeability continuum, steady-state laminar flow of a viscous, incompressible fluid can be simulated under unidirectional flow geometry (Figure 5-6a) and radial flow geometry (Figure 5-6b). For both simulations, upper and lower sides, which are not shown in Figure 5-6, are non-flow boundaries where the pressure gradient is zero. Fluid macroscopically flows in the direction of the x-axis in Figure 5-6a, and it is also possible to simulate macroscopic fluid flows in the directions of the y-axis and the z-axis by setting the similar boundary conditions. Results of unidirectional flow simulations will reveal the distributions of flow paths in a state of nature. In contrast, results of radial flow simulations will reveal the distribution of flow paths in a state of oil/gas production, and fluid macroscopically flows from sidewall boundaries to Well A and Well B in Figure 5-6b. In this study, differential pressure, ΔP, is set to constant value of 0.1 MPa for the both flow geometries. For both Well A and Well B, the depth of well is 580 m (see Figure 5-6b), which is also determined so that the actual settings of the Yufutsu oil/gas field can be imitated.

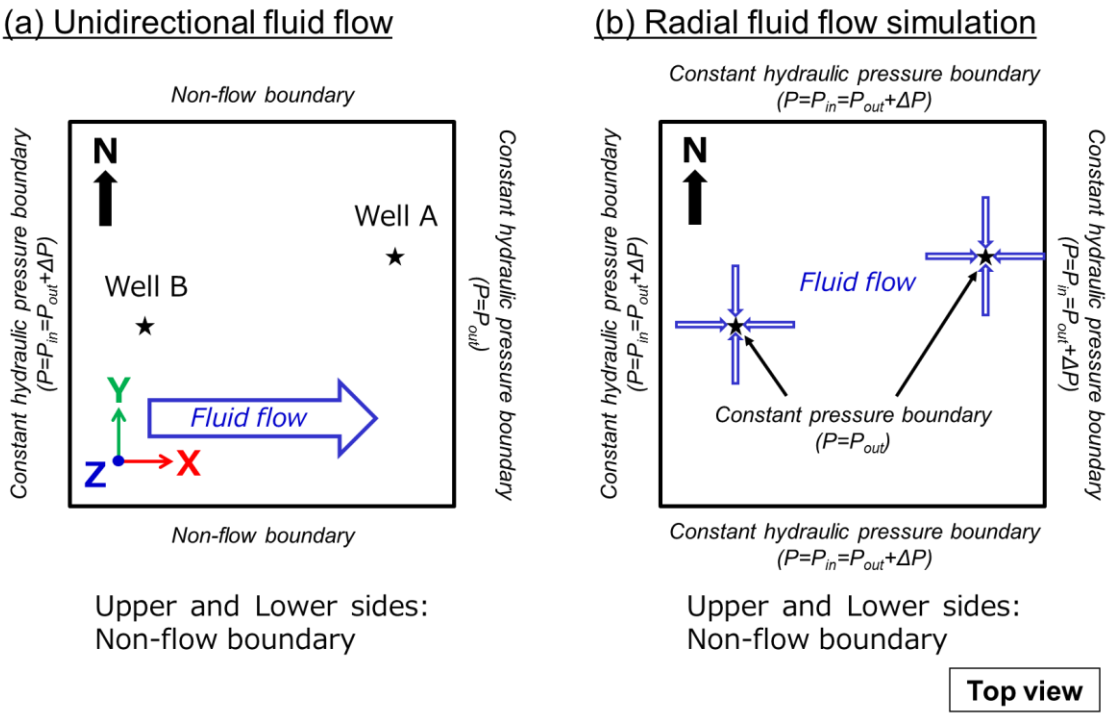

Figure 5-6. Boundary conditions for (a) unidirectional fluid flow simulation and (b) radial fluid flow simulation.

For the case of the shear displacement of 4×10^{-3} (0.4%) for critically-stressed fractures, unidirectional fluid flow simulations in the directions of the x-, y-, and z-axes are conducted with GeoFlow model. To clarify the fluid flow characteristics of the fractured reservoir, permeability of the reservoir and the flowing fluid existing volume, which is defined as the ratio of the volume where 95% of total flow exists to the volume where fractures exist within the analytical domain, are calculated in the unidirectional fluid flow simulations. In contrast, for the same case of shear displacement, radial fluid flow simulations are conducted with both GeoFlow model and Conventional DFN model, and these results are compared. In the radial fluid flow simulations, the flow path distributions are evaluated, and the productivities of Well A and Well B, and the fluid existing volume are also calculated.

Subsequently, for the case of the shear displacement of 1×10^{-3} (0.1%), 2×10^{-2} (2%), and 4×10^{-2} (4%) for critically-stressed fractures, radial fluid flow simulations are conducted with both GeoFlow model and Conventional DFN model, where the flow path distribution, the productivities of Well A and Well B, and the fluid existing volume are evaluated. Particularly, for the case that the shear displacement is 2×10^{-2} (2%), the flow paths distributions of unidirectional fluid flow are evaluated in the directions of the x-, y-, and z-axes.

Based on the simulation results described above, the characteristics and impact of 3-D channeling flow in a fractured reservoir is examined and discussed.

5.4. Results and Discussion

5.4.1. Reproduction of three orders of magnitude difference in well productivity observed in the Yufutsu oil/gas field by GeoFlow simulations

The results of the fluid flow simulations reveal that three orders of magnitude difference in well productivity observed in the Yufutsu oil/gas field can be reproduced only with GeoFlow model. Since the principal difference between GeoFlow model and Conventional DFN model is whether the occurrence of 3-D channeling flow is considered or not, it can be concluded that one of the most likely causes for the significant difference in well productivity is 3-D channeling flow. The detail of the simulation results is explained in the followings.

In evaluating the fluid flow characteristics of a fractured reservoir by using DFN modeling

techniques, it is desirable that the parameters for fluid flow characteristics, which are calculated for multiple realizations, are ensemble averaged. This is because the parameters for fluid flow characteristics vary significantly in response to the distribution of rock fractures, even though the fracture distributions are stochastically equivalent. Additionally, to visualize permeability maps and flow path distributions, local permeabilities and local flow rates, which are calculated for the respective elements of the equivalent permeability continuum of DFN, should be ensemble averaged as well.

First, the results of unidirectional fluid flow simulations for the fractured reservoir with the 15 kinds of GeoFlow models are shown in Figure 5-7, where the shear displacement of critically-stressed fractures is equal to 4×10^{-3} (0.4%). The permeabilities of reservoir and the flowing fluid existing volumes for x-, y-, and z-directions are summarized in Table 5-2. For the respective directions, it is confirmed that the permeability (Figure 5-7a) and the flowing fluid existing volume (Figure 5-7b) vary significantly depending on the fracture distributions. Ensemble averages of the permeabilities for x-, y-, and z-directions are 7.3×10^{-14} m^2, 5.0×10^{-13} m^2, and 3.5×10^{-13} m^2, whereas ensemble averages of the flowing fluid existing volumes for x-, y-, and z-directions are 7.6%, 6.1%, and 7.8%. These values are also summarized in Table 5-2, and are shown in Figures 5-7a and 5-7b with the different type of broken lines. Then, fluid flow characteristics of the Yufutsu oil/gas field are discussed. As described above, the anisotropy of the permeabilities of reservoir is revealed, which is maybe caused by the fact that the directions of shear displacement are preliminary constrained by the overall trend of the maximum principal stress direction (see Figure 5-5). In contrast, the difference in flowing fluid existing volumes is very small, which indicates that there is few anisotropy in flowing fluid existing volume. It is quantitatively clarified that the extremely limited parts within the fracture existing volume contribute on the fluid flow and approximately 50% of fracture existing volume is dominated by stagnant fluid in a state of nature.

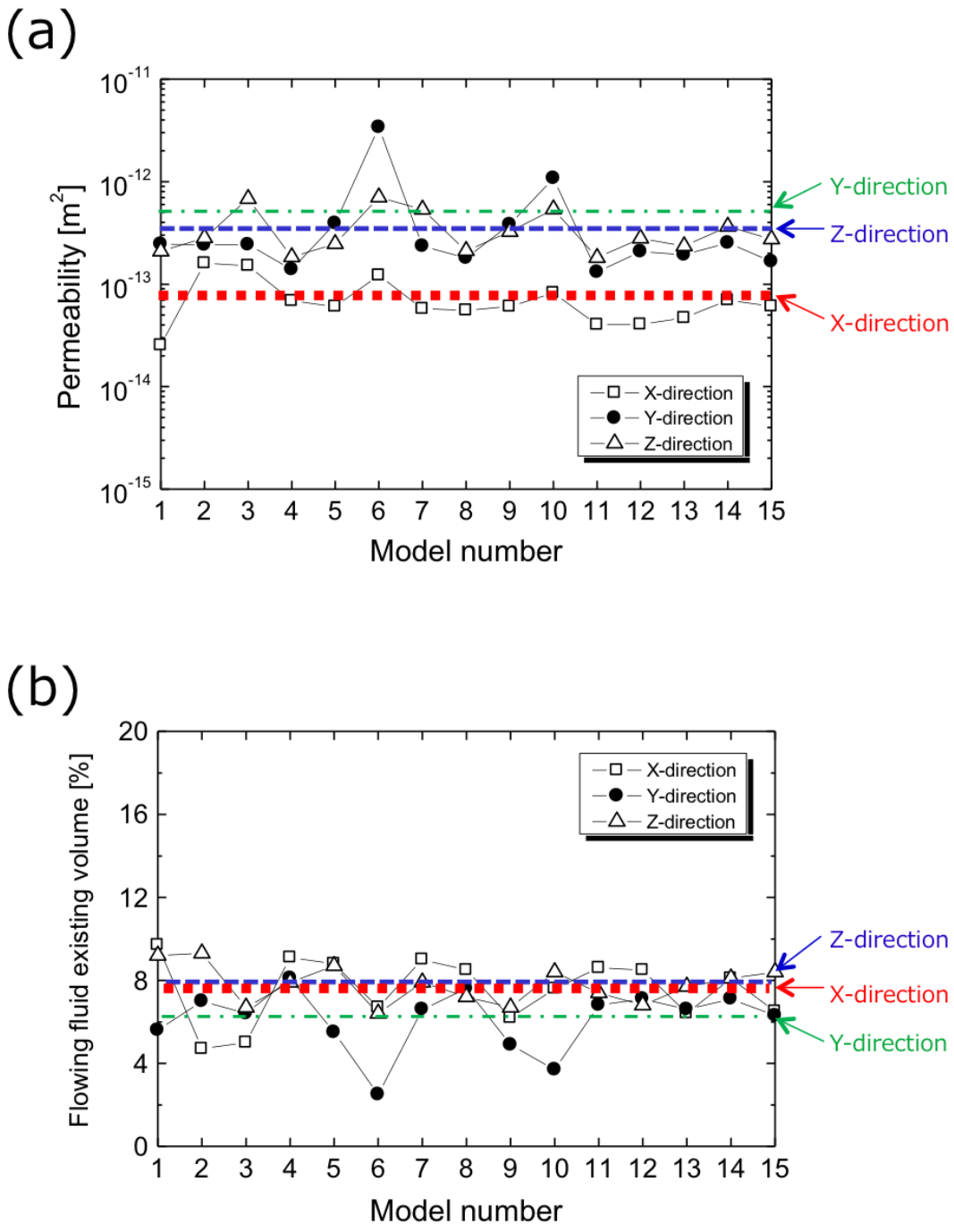

Figure 5-7. (a) Permeabilities of the fractured reservoir evaluated with GeoFlow models and (b) flowing fluid existing volumes for x-, y-, and z-directions. Distributions of fractures are stochastically equivalent for these 15 models, and the ensemble averages for each direction are shown with the different type of broken lines.

Table 5-2. Permeabilities of the fractured reservoir evaluated with GeoFlow models and flowing fluid existing volumes in the direction of x-, y-, and z-axis. The ensemble average values for permeability and fluid existing volume are also shown herein.

Model number	X-direction		Y-direction		Z-direction	
	Permeability [m^2]	Flowing fluid existing volume [%]	Permeability [m^2]	Flowing fluid existing volume [%]	Permeability [m^2]	Flowing fluid existing volume [%]
Network 01	2.53×10^{-14}	9.7	2.46×10^{-13}	5.6	2.09×10^{-13}	9.2
Network 02	1.60×10^{-13}	4.7	2.42×10^{-13}	7.0	2.82×10^{-13}	9.3
Network 03	1.51×10^{-13}	5.0	2.43×10^{-13}	6.4	6.82×10^{-13}	6.7
Network 04	6.87×10^{-14}	9.1	1.39×10^{-13}	8.1	1.84×10^{-13}	7.9
Network 05	6.06×10^{-14}	8.8	3.91×10^{-13}	5.5	2.47×10^{-13}	8.7
Network 06	1.22×10^{-13}	6.7	3.40×10^{-12}	2.5	7.04×10^{-13}	6.4
Network 07	5.74×10^{-14}	9.0	2.35×10^{-13}	6.6	5.34×10^{-13}	7.9
Network 08	5.57×10^{-14}	8.5	1.80×10^{-13}	7.6	2.11×10^{-13}	7.2
Network 09	6.04×10^{-14}	6.2	3.81×10^{-13}	4.9	3.24×10^{-13}	6.7
Network 10	8.22×10^{-14}	7.6	1.08×10^{-12}	3.7	5.37×10^{-13}	8.4
Network 11	4.03×10^{-14}	8.6	1.31×10^{-13}	6.8	1.81×10^{-13}	7.4
Network 12	4.05×10^{-14}	8.5	2.08×10^{-13}	7.1	2.79×10^{-13}	6.8
Network 13	4.67×10^{-14}	6.4	1.93×10^{-13}	6.6	2.35×10^{-13}	7.7
Network 14	6.99×10^{-14}	8.1	2.52×10^{-13}	7.1	3.65×10^{-13}	8.1
Network 15	6.09×10^{-14}	6.5	1.66×10^{-13}	6.3	2.75×10^{-13}	8.4
Average	7.3×10^{-14}	7.6	5.0×10^{-13}	6.1	3.5×10^{-13}	7.8

For the GeoFlow model of the fractured reservoir, where the shear displacement of critically-stressed fractures is 4×10^{-3} (0.4%), the permeability map is evaluated as shown in Figure 5-8a. The overall trend of the maximum principal stress direction, the directions of shear displacements for critically-stressed fractures, and the locations of Well A and Well B are also indicated in the same figure. For the locations of both Well A and Well B, it is preliminary confirmed that these wells intersect more than one critically-stressed fracture. The permeability map evaluated with GeoFlow model is compared with the permeability map evaluated with Conventional DFN model (Figure 5-8b). In these figures, highly permeable zones, which are almost corresponding to the critically stressed fractures, are shown with different colors depending on the permeability values. Due to the fact that the individual fractures have heterogeneous aperture distributions in response to fracture scales and shear displacements, highly permeable zones distribute as dots in the GeoFlow model. On the other hands, since the individual fractures are modeled by pairs of parallel smooth plates with scale-dependent unique apertures, highly permeable zones correspond to the entire fracture plane of critically-stressed fractures of relatively large scales in the Conventional DFN model. These results make us sure that 3-D channeling flow in the fractured reservoir can be simulated only in the GeoFlow model.

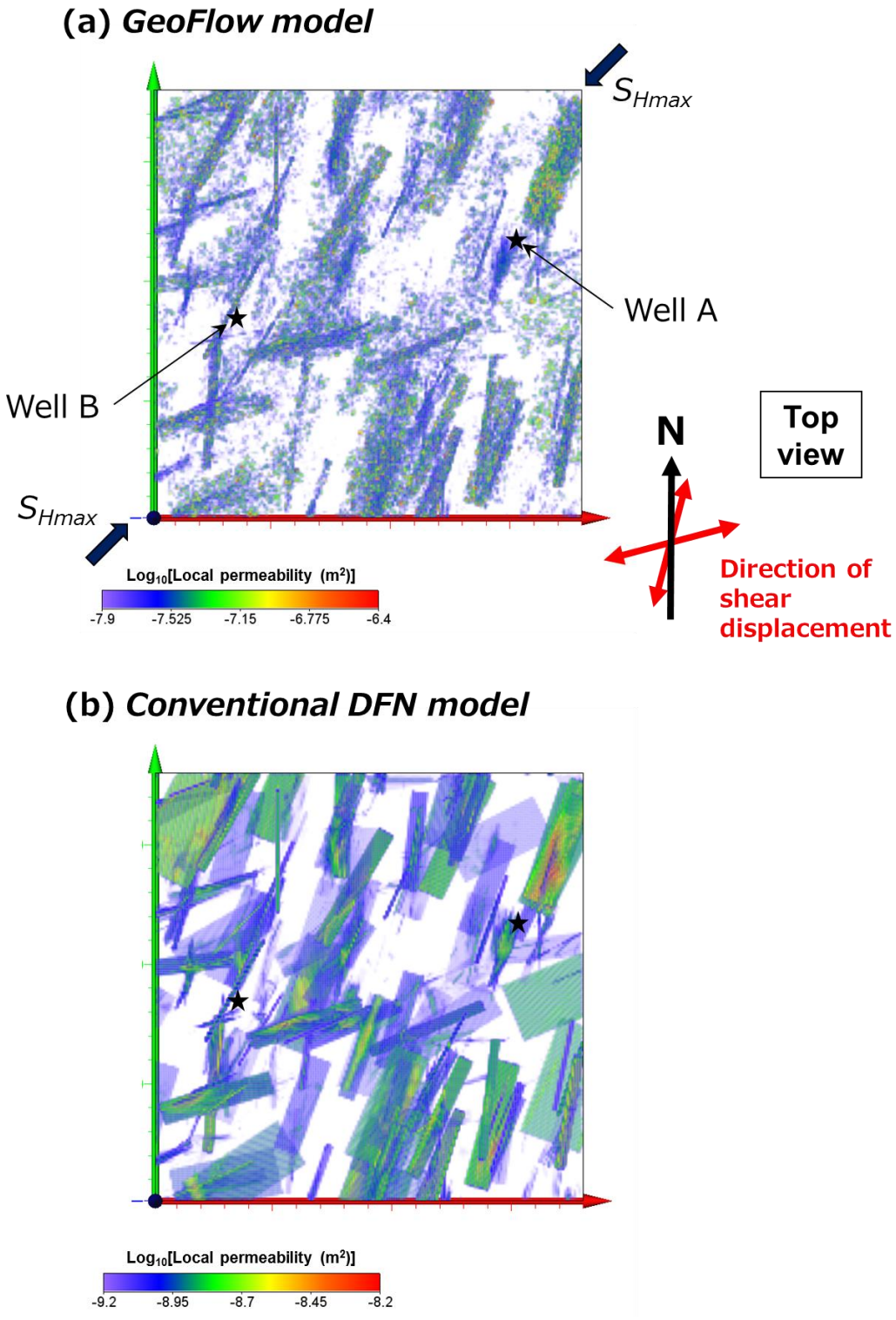

Figure 5-8. Permeability maps for the Yufutsu field evaluated with (a) GeoFlow model and (b) Conventional DFN model. Highly permeable zone in critically-stressed fractures are shown with colors. Note that the shear displacement of critically-stressed fractures is 4×10^{-3} (0.4%).

When the flow path distributions are visualized, the ensemble averaged local flow rates are furthermore normalized by their maximum value. The flow path distributions are shown with different colors in response to the normalized values. Particularly, when the results of the radial fluid flow simulations are shown in the following, the summation of the normalized values for the elements corresponding to the visualized flow path is 95% of the summation for the entire analytical domain.

The results of the radial fluid flow simulations for the fractured reservoir are shown in Figure 5-9 as flow path distributions, where the shear displacement of critically-stressed fractures is equal to 4×10^{-3} (0.4%). Figure 5-9a is the flow path distributions evaluated with GeoFlow model, whereas Figure 5-9b is the flow path distributions evaluated with Conventional DFN model. For these models, it is common that flow paths are formed for the highly permeable zones within critically-stressed fractures (see Figure 5-8), and the flow paths are towards Well A and Well B. The Flow paths towards Well A are mainly from north, south, and east side boundaries, whereas the flow paths towards Well B are mainly from west side boundary. Although the appearances of flow path distributions are alike between GeoFlow model and Conventional DFN model, 3-D channeling flow in a fractured reservoir can be considered only in the GeoFlow model.

In the GeoFlow model, the productivities of Well A and Well B are 9.32 m^3/sec and 0.13 m^3/sec, and the fluid existing volume is 6.0%. Productivity of Well A is 71 times higher than that of Well B. In contrast, in the Conventional DFN model, the productivities of Well A and Well B are 1.69 m^3/sec and 0.075 m^3/sec, and the fluid existing volume is 8.4%. Productivity of Well A is 23 times higher than that of Well B. The reason why the productivity of Well A is higher than that of Well B is explained in the next section. Both models can reproduce the observation of the Yufutsu oil/gas field in that the productivity of Well A is higher than that of Well B, but neither the GeoFlow model nor the Conventional DFN model can reproduce the three orders of magnitude difference in productivity between Well A and Well B. Here, it is quantitatively clarified that the localization of flow paths of the GeoFlow model is more remarkable than that of the Conventional DFN model, and that the difference in the well productivity of the GeoFlow model is larger than that of the Conventional DFN model, which

are explicitly due to the occurrence of 3-D channeling flow in the reservoir. However, since the difference in the well productivity evaluated by the GeoFlow model is still far from the observed fact, it is difficult to tell that GeoFlow model has much more advantages than the Conventional DFN model herein.

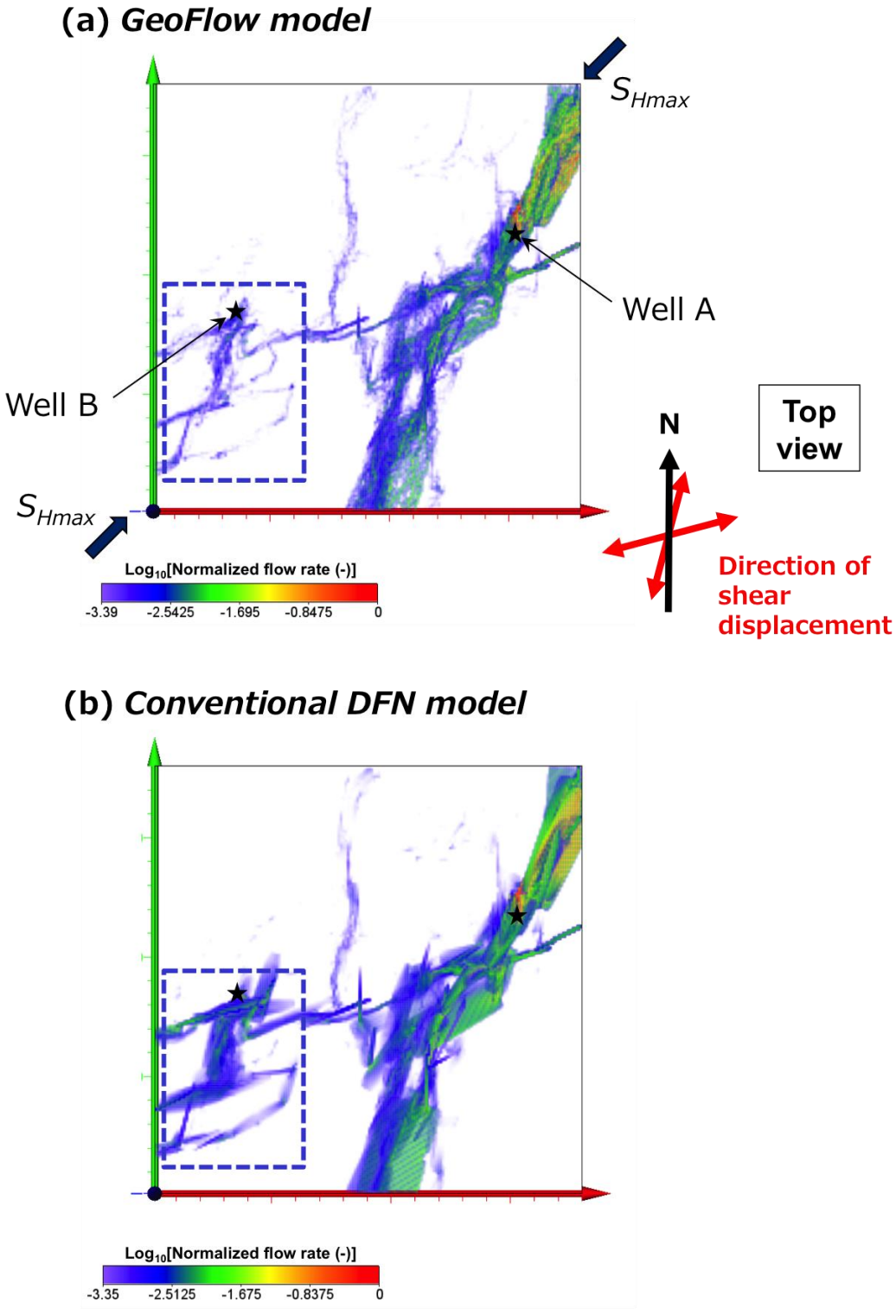

Figure 5-9. Flow path distributions for the Yufutsu field evaluated with (a) GeoFlow model and (b) Conventional DFN model. The shear displacement of critically-stressed fractures is 4×10^{-3} (0.4%).

It is considered that the discrepancy between the simulation results and the observation is caused by the fact that the shear displacement of 4×10^{-3} (0.4%) for critically-stressed fractures, which is assumed in the models, is not adequate. To reproduce the observed fact, a shear displacement of critically-stressed fractures should be calibrated. Therefore, the radial fluid flow simulations of the fractured reservoir are conducted for the case that the shear displacement of critically-stressed fractures is 1×10^{-3} (0.1%), 2×10^{-2} (2%), and 4×10^{-2} (4%). The simulation results for the respective cases are shown in Figure 5-10, 5-11, and 5-12 as flow path distributions. Figures 5-10a, 5-11a, and 5-12a are the flow path distributions evaluated with GeoFlow models, whereas Figures 5-10b, 5-11b, and 5-12b are the flow path distributions evaluated with Conventional DFN models. These results are coupled with the result for Figures 5-9a and 5-9b in the following explanations and discussion.

When the shear displacement of critically-stressed fractures is 2×10^{-2} (2%) and 4×10^{-2} (4%), the appearances of flow path distributions are completely different between GeoFlow model and Conventional DFN model (Figures 5-11 and 5-12), which is due to the fact that 3-D channeling flow in a fractured reservoir is considered only in the GeoFlow models. With respect to the flow paths towards Well A, these paths are consistently formed regardless of the shear displacement, which is common for both GeoFlow models and Conventional DFN models. On the other hands, with respect to the flow paths towards Well B, which located within the area enclosed by the bold break line in Figures 5-9, 5-10, 5-11, and 5-12, their responses to the shear displacement are different between these models. For GeoFlow models, these paths are vanished completely when the shear displacement is over 2%. For Conventional DFN models, in contrast, these paths are consistently formed regardless of the shear displacement. The presence or absence of the flow paths towards Well B within the reservoir is critically important for reproducing the three orders of magnitude difference in well productivity observed at the Yufutusu field.

Then, the flowing fluid existing volumes evaluated with the GeoFlow models and the Conventional DFN models are summarized in Table 5-3. Based on this table, the responses of the flowing fluid existing volume to the shear displacement are examined in Figure 5-13. This figure quantitatively reveal that the fluid existing volume decreases with increasing shear

displacement. This fact indicates that the degree of the flow paths localization increases with increasing shear displacement, which is certainly seen in Figures 5-9, 5-10, 5-11, and 5-12. The Conventional DFN models can predict this characteristic, but overestimate the fluid existing volume. This overestimation of the fluid existing volume is also caused by the fact that the occurrence of 3-D channeling flow is ignored in the Conventional DFN models.

Table 5-3. Dependencies of the flowing fluid existing volume on the shear displacement of critically-stressed fractures for GeoFlow model and Conventional DFN model.

Shear displacement of critically-stressed fractures [%]	Flowing fluid existing volume evaluated by GeoFlow model [%]	Flowing fluid existing volume evaluated by conventional DFN model [%]
0.1	23.9	30.2
0.4	6.0	8.4
2.0	2.4	4.0
4.0	1.1	3.2

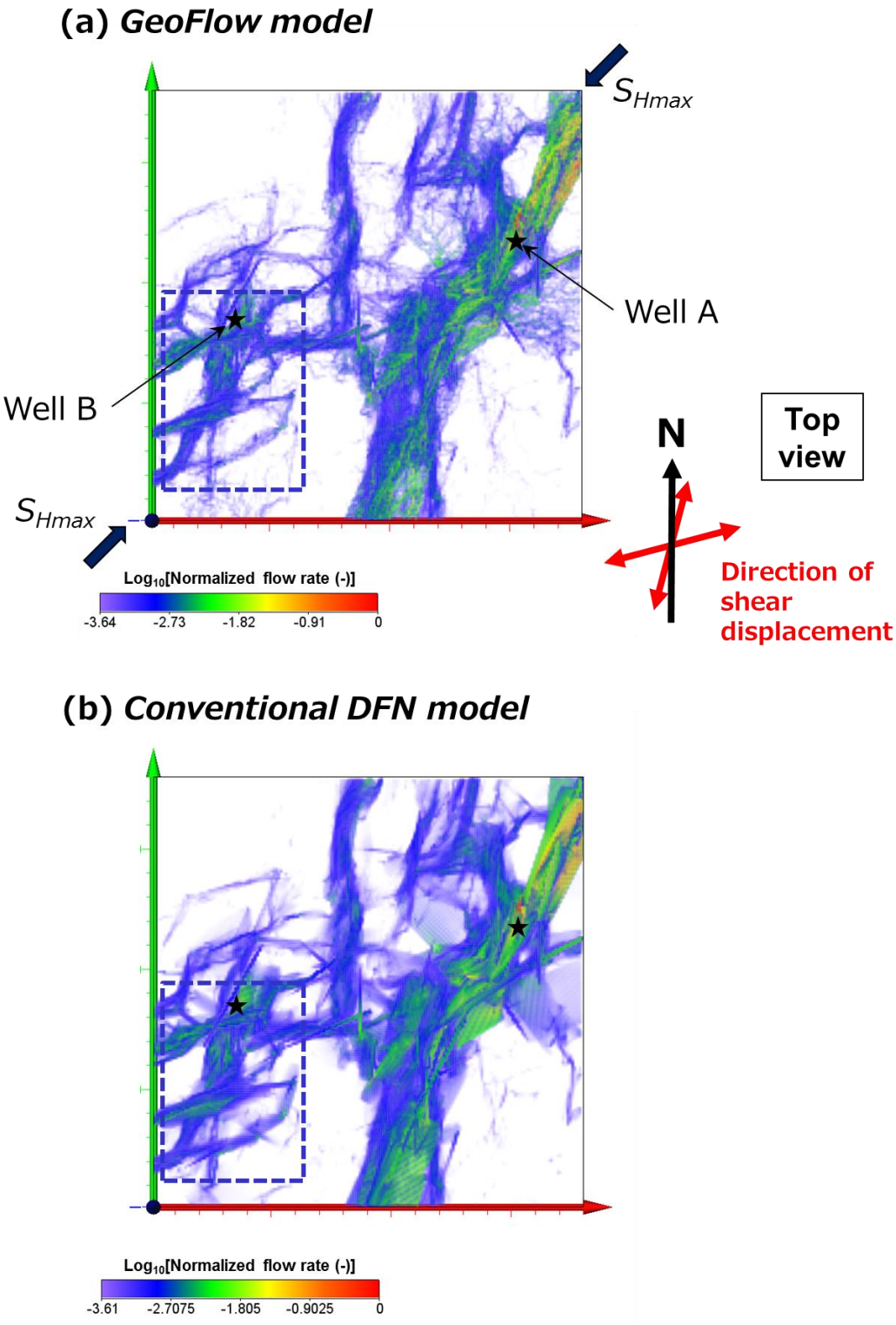

Figure 5-10. Flow path distributions for the Yufutsu field evaluated with (a) GeoFlow model and (b) Conventional DFN model. The shear displacement of critically-stressed fractures is 1×10^{-3} (0.1%).

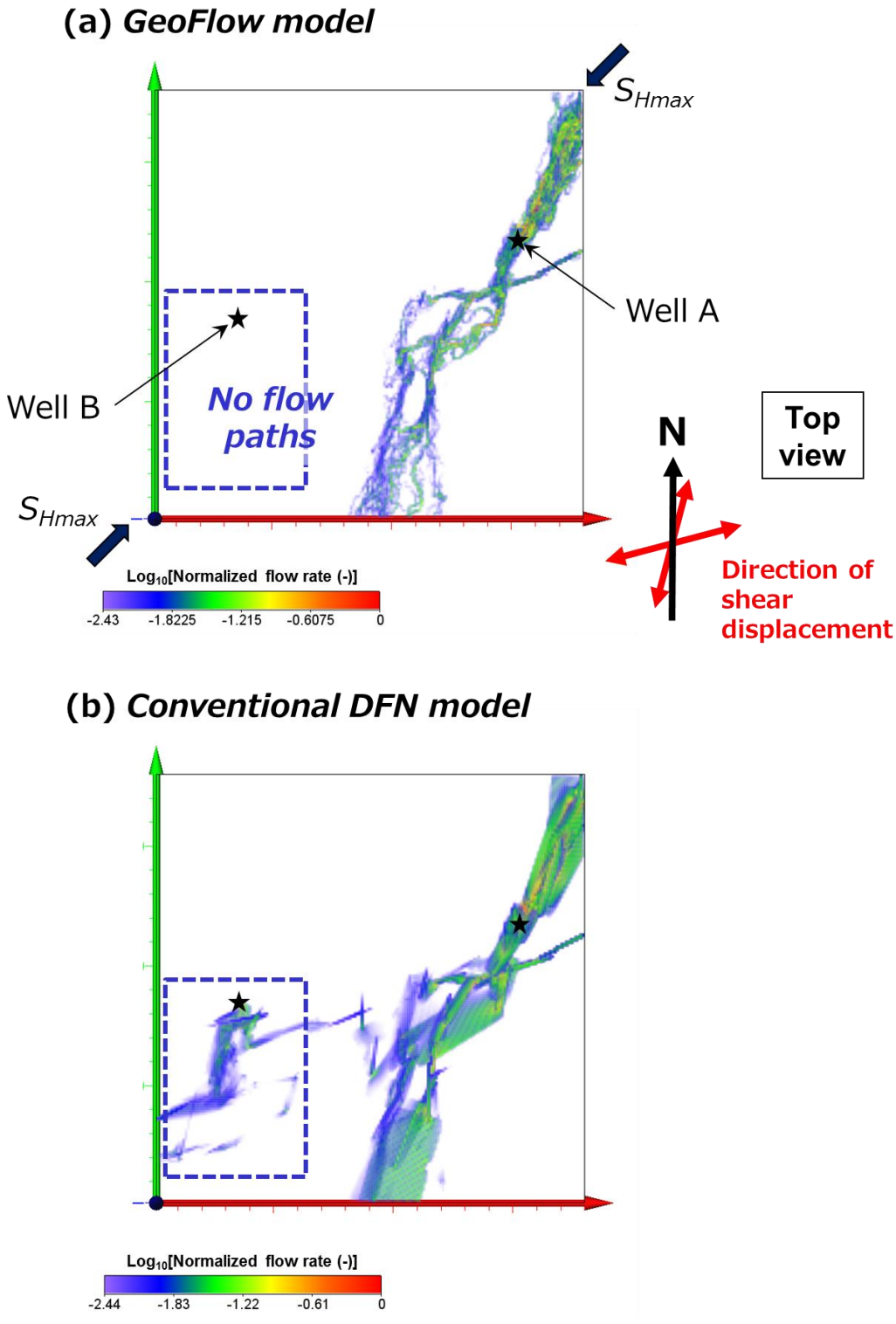

Figure 5-11. Flow path distributions for the Yufutsu field evaluated with (a) GeoFlow model and (b) Conventional DFN model. The shear displacement of critically-stressed fractures is 2×10^{-2} (2%).

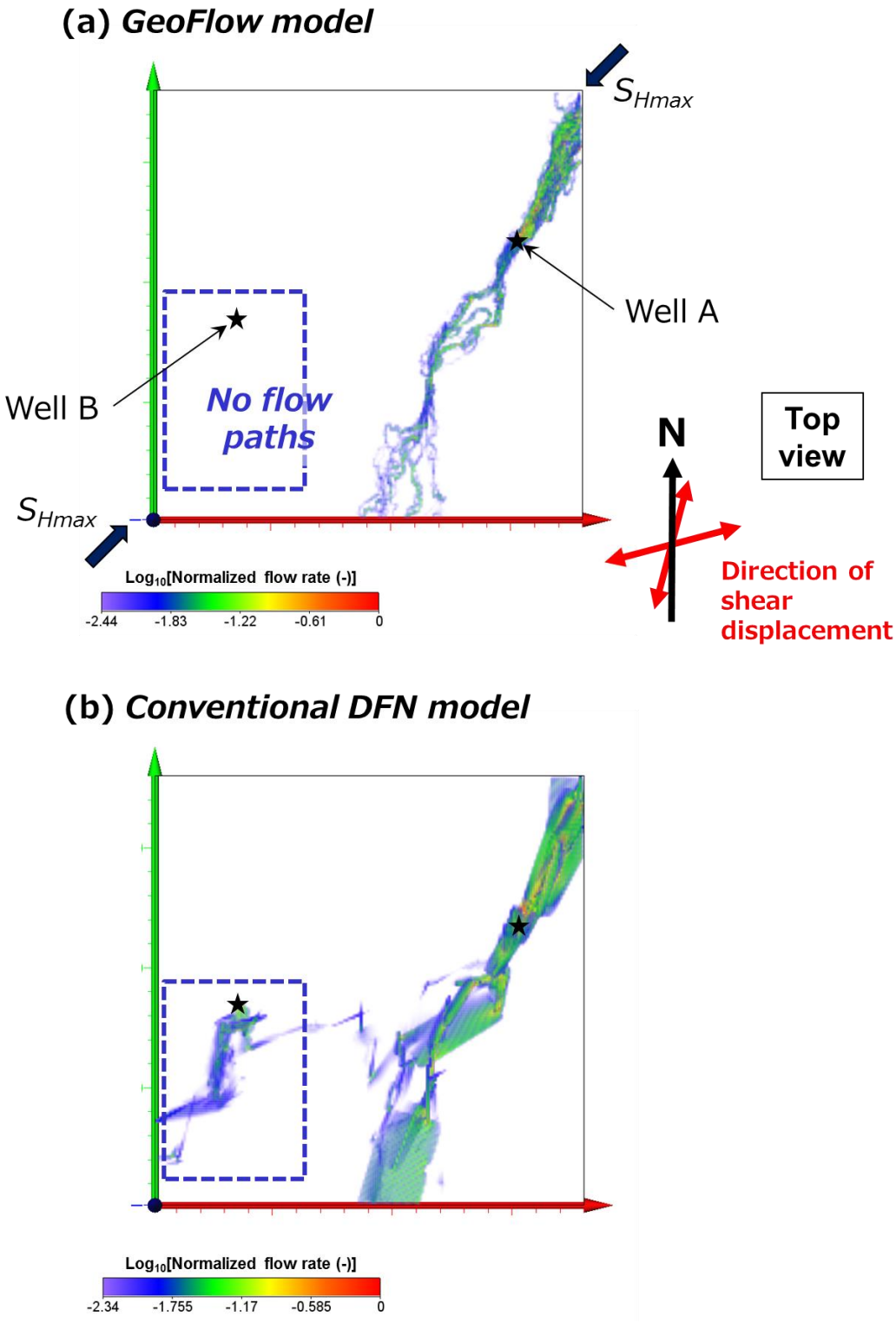

Figure 5-12. Flow path distributions for the Yufutsu field evaluated with (a) GeoFlow model and (b) Conventional DFN model. The shear displacement of critically-stressed fractures is 4×10^{-2} (4%).

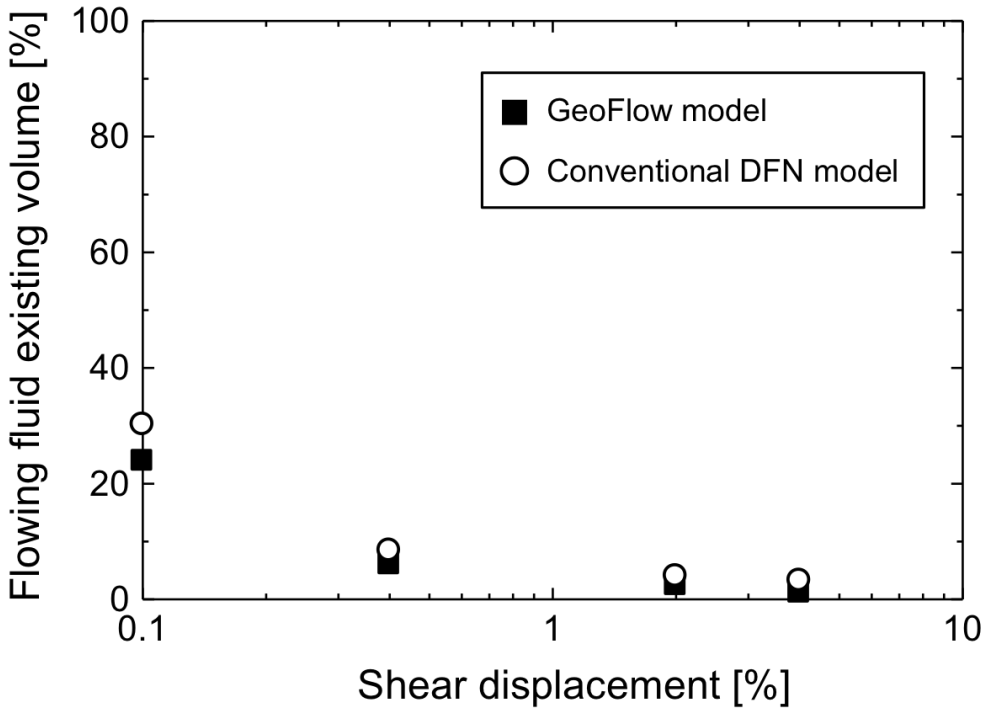

Figure 5-13. Dependencies of the fluid existing volume on the shear displacement of critically-stressed fractures evaluated with GeoFlow model (solid square symbols) and Conventional DFN model (open circle symbols).

Subsequently, the productivities of Well A and Well B, and the ratio of productivity of Well A to that of Well B ("Ratio of productivities" hereafter) evaluated with the GeoFlow models and the Conventional DFN models are summarized in Table 5-4. On the basis of this table, the changes of the well productivities with the shear displacement are shown in Figures 5-14a (GeoFlow model) and 5-14b (Conventional DFN model). Moreover, the changes of the Ratio of productivities with shear displacement are shown in Figure 5-15.

In the GeoFlow model, with increasing shear displacement, the productivity of Well A increases significantly whereas the productivity of Well B increases very gradually. The ratio of productivities, as a result, linearly increases with increasing shear displacement on a log-log plot, when the shear displacement is less than ~ 5×10^{-2} (5%). As can be seen in Figure 5-15, the Ratio

of productivities of 1,000, which correspond to the observation at the Yufutsu oil/gas field, can be successfully reproduced at the shear displacement of 1.7×10^{-2} (1.7%). Here, the flow paths towards Well A are formed whereas the flow paths towards Well B are almost all vanished, which clarifies the significant dominancy of the flow paths towards Well A in the Yufutsu field. On the other hands, in the Conventional DFN model, the productivities of both Well A and Well B increase significantly with increasing shear displacement. Since the flow paths towards Well A and Well B are consistently formed regardless of the shear displacement, the increasing trends in the productivities with increasing shear displacement are similar between Well A and Well B. Consequently, the change in the Ratio of productivities with shear displacement is very small and the no clear relation between them are observed, where the Ratio of productivities is consistently less than 40 (Figure 5-15). This results means that the Conventional DFN model can't reproduce the fluid flow within a fractured reservoir (i.e. the Yufutus oil/gas field), which is also reported in *Tamagawa et al.* [2010]. Specifically, the discrepancy between the GeoFlow model and the Conventional DFN model is significant when the shear displacement is relatively large. Thus, it is revealed that the reality of fluid flow within a fractured reservoir is 3-D channeling flow, which we can consider only by analyzing with GeoFlow or the similar concept of DFN model simulators. Note that there are some concerns that we will come to the wrong conclusions for the development and utilization of a fractured reservoir, if the occurrence of 3-D channeling within the reservoir is not considered.

In this section, the validity of the shear displacement of 1.7×10^{-2} (1.7%), which is assumed for the critically-stressed fractures in the aforementioned GeoFlow model, are finally discussed. For the discussion, the maximum aperture-fracture length relations for natural faults are reconsidered. As shown in Figure 3-11 in Chapter Ⅲ, maximum aperture of the faults linearly increase with increasing fracture length on a log-log plot with a slope of unity. This characteristic and the absolute value for the maximum aperture can be reproduced adequately when the shear displacement of 1×10^{-2} (1%) is given to the rock fractures. In other words, it is possible to assume that natural faults have the shear displacement of around 1×10^{-2} (1%). With this in mind, the shear displacement of 1.7×10^{-2} (1.7%) is not so far from the nature and is conceivable.

Table 5-4. Dependencies of the productivities of Well A and Well B on the shear displacement of critically-stressed fractures for GeoFlow model and Conventional DFN model.

Shear displacement of critically stressed fractures [%]	GeoFlow model			Conventional DFN model		
	Productivity [m^3/s]		Ratio of productivity [-]	Productivity [m^3/s]		Ratio of productivity [-]
	Well A	Well B		Well A	Well B	
0.1	1.02	7.63×10^{-2}	13.3	1.87×10^{-1}	1.96×10^{-2}	9.54
0.4	9.32	1.32×10^{-1}	70.6	1.69	7.51×10^{-2}	22.5
2.0	2.30×10^{2}	1.47×10^{-1}	1.56×10^{3}	17.4	4.96×10^{-1}	35.1
4.0	5.02×10^{2}	1.35×10^{-1}	3.72×10^{3}	49.2	1.61	30.6

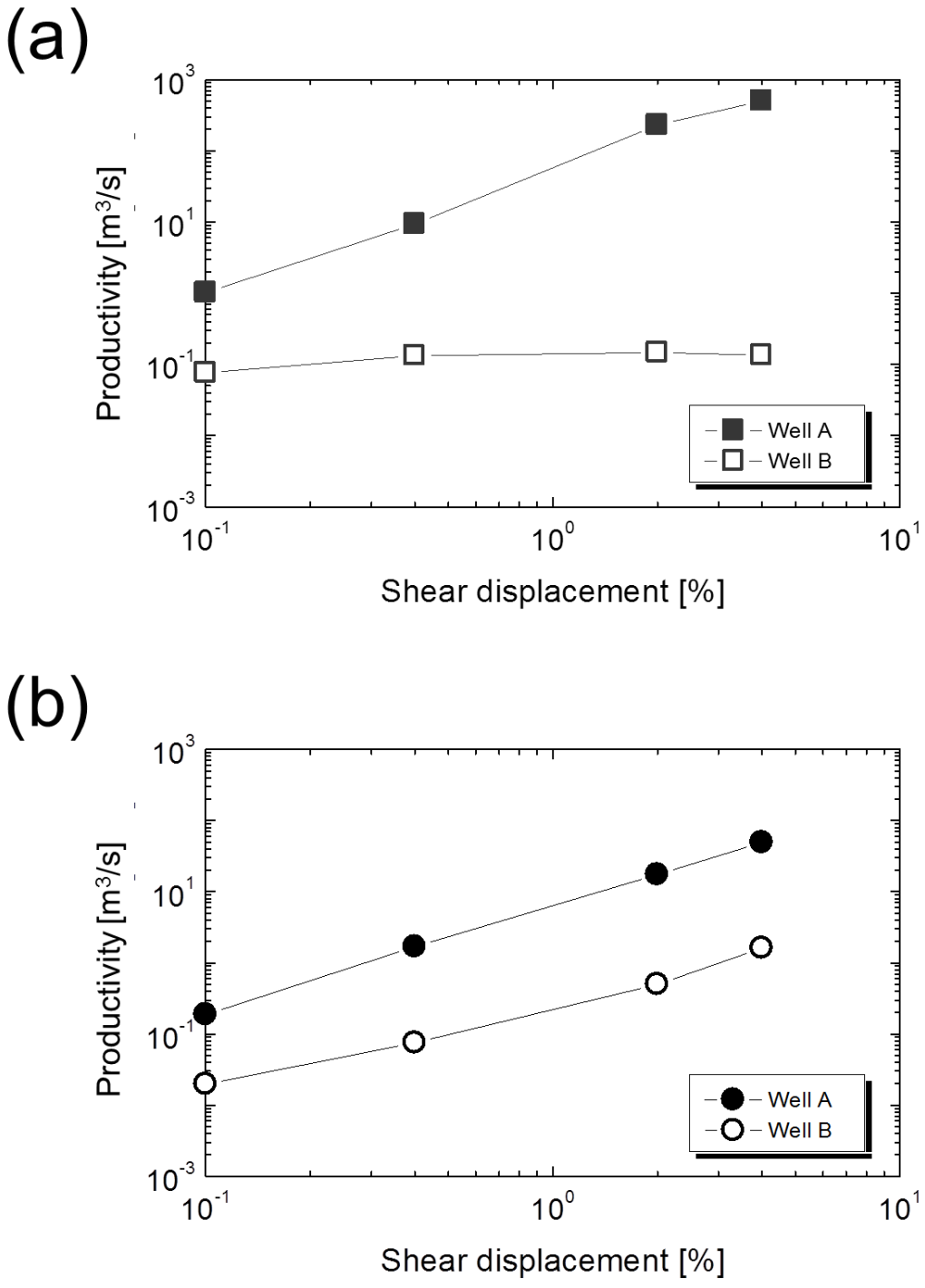

Figure 5-14. Dependencies of the productivities of Well A and Well B on the shear displacement of critically-stressed fractures evaluated with (a) GeoFlow model and (b) Conventional DFN model.

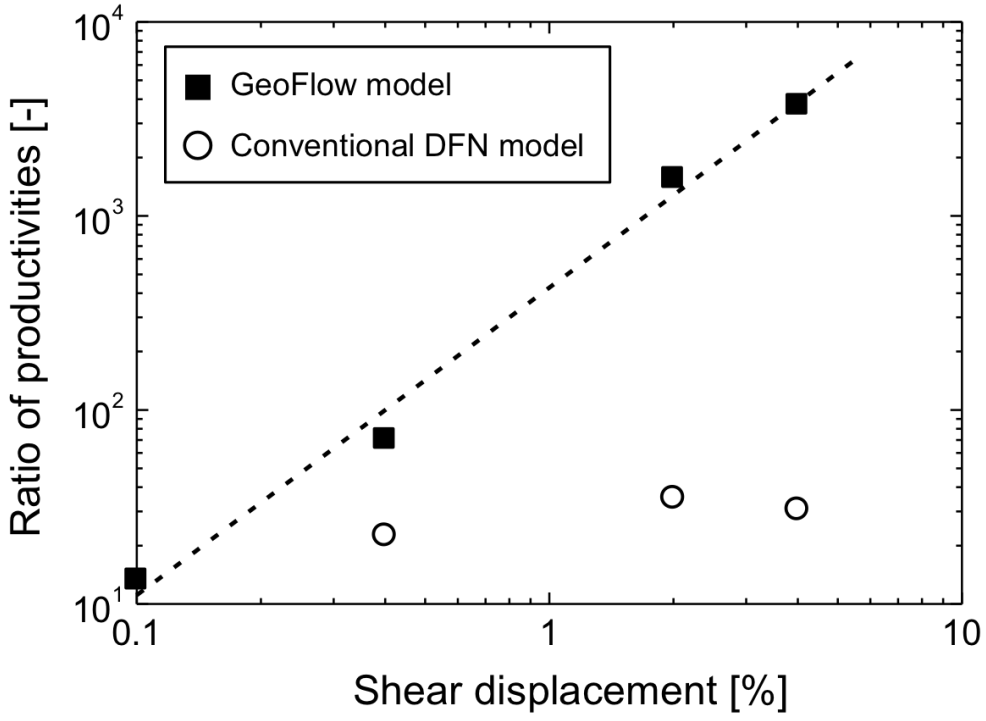

Figure 5-15. Dependencies of the ratio of productivity of Well A to that of Well B on the shear displacement of critically-stressed fractures evaluated with GeoFlow model (solid square symbols) and Conventional DFN model (open circle symbols). Dashed line represents the approximated linear curve for the relationship evaluated with GeoFlow model.

5.4.2. Clarification of the mechanism causing the huge difference in well productivity

Three orders of magnitude difference in well productivity observed in the fractured reservoir (i.e. the Yufutsu oil/gas field) is successfully reproduced with GeoFlow model, where the shear displacement of 1.7×10^{-2} (1.7%) is assumed for critically-stressed fractures. The significant difference in well productivity hasn't been reproduced to date and this study is the first success. Therefore, it is essential to clarify the mechanism causing the significant difference in well productivity herein.

In order to discuss the mechanism, the results of fluid flow simulations with GeoFlow model, where the shear displacement of critically-stressed fractures is 2×10^{-2} (2%), are

considered. This is because the Ratio of productivities is 1.56×10^3 (1,560) for this GeoFlow model, which is the closest to the observation at the Yufutsu field in the four kind of GeoFlow models used in the previous section.

The flow paths distributions of unidirectional fluid flow evaluated in the directions of the x-, y-, and z-axes are respectively shown in Figure 5-16a, 5-16b, and 5-16c. These figures represent the distribution of flow paths within the fractured reservoir in a state of nature. Since it is considered that the distribution of flow paths in a state of oil/gas production (i.e. Figure 5-11a) is closely relate to the distribution of flow paths in a state of nature (Figure 5-16a, 5-16b, and 5-16c), these flow paths are first compared herein.

Through the comparisons, it is revealed that Well A is set for the area where natural flow paths in x- and y-directions exist originally. Due to this fact, it is also found that both degrees of fracture connectivity in x- and y-directions are good. Additionally, since the natural flow path in z-direction overlaps substantially with the natural flow path in y-direction for the area, fluid flow in z-direction can contribute on the oil/gas production at Well A. In this manner, since all of fluid flows for x-, y-, and z-direction can contribute on the oil/gas production at Well A, the productivity of Well A is significantly high. In contrast, it is revealed that Well B is set for the area where only the natural flow paths in x-direction exists originally, although Well B deviates from the flow paths. Considering this fact, it can be concluded that both degrees of fracture connectivity in x- and y-directions are not so good for the area. Moreover, it is difficult of fluid flow in z-direction to contribute on the oil/gas production at Well B, because the natural flow path in z-direction deviates from Well B and is isolated from the natural flow path in x-direction. Thus, only the fluid flow for x-direction can contributes on the on the oil/gas production at Well B and, as a result, the productivity of Well B is low.

The flow paths distributions of unidirectional fluid flow evaluated in the directions of the x-, y-, and z-axes are superimposed in Figure 5-16d, and the super imposed flow path distribution is compared with the flow paths distribution in a state of oil/gas production (Figure 5-11a). With respect to the flow paths towards Well A, appearances of flow paths are alike between Figure 5-11a and Figure 5-16d. With respect to the flow paths towards Well B, due to the fact that Well B deviates from the natural flow path in x- and z-direction (5-16d), no such

flow path is formed in a state of oil/gas production (Figure 5-11a). These correspondences implicated that the optimum locations of wells can be predicted for a fractured reservoir if 3-D channeling flows in a state of nature are evaluated precisely within the reservoir, which are realized only by using GeoFlow or similar concept of DFN model simulators.

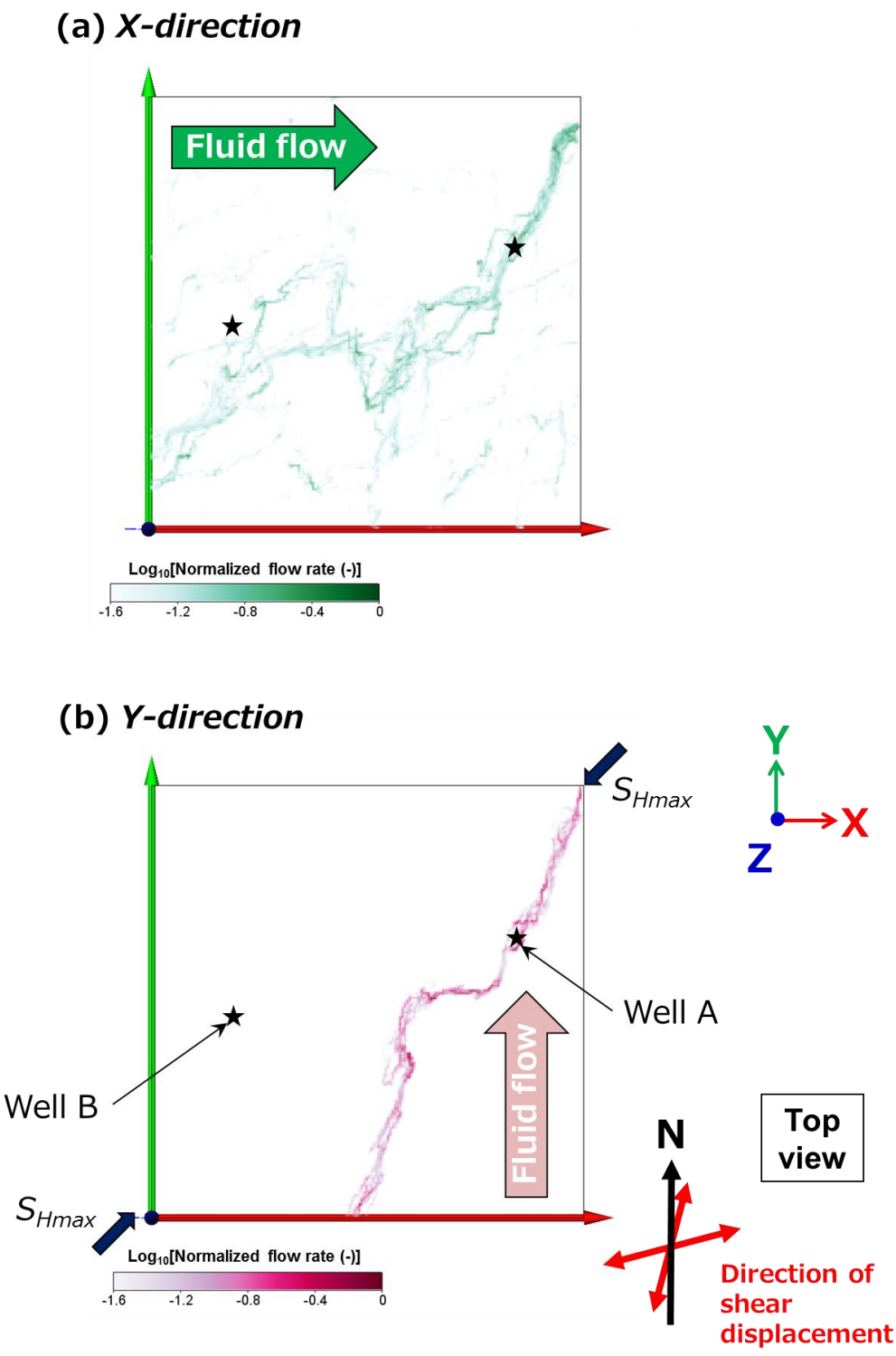

Figure 5-16. Flow path distributions of the Yufutsu field in a state of nature for (a) x-direction, (b) y-direction, and (c) z-direction. Furthermore, (d) superimposed flow path distribution for the three directions is also shown. The shear displacement of critically-stressed fractures is 2×10^{-2}.

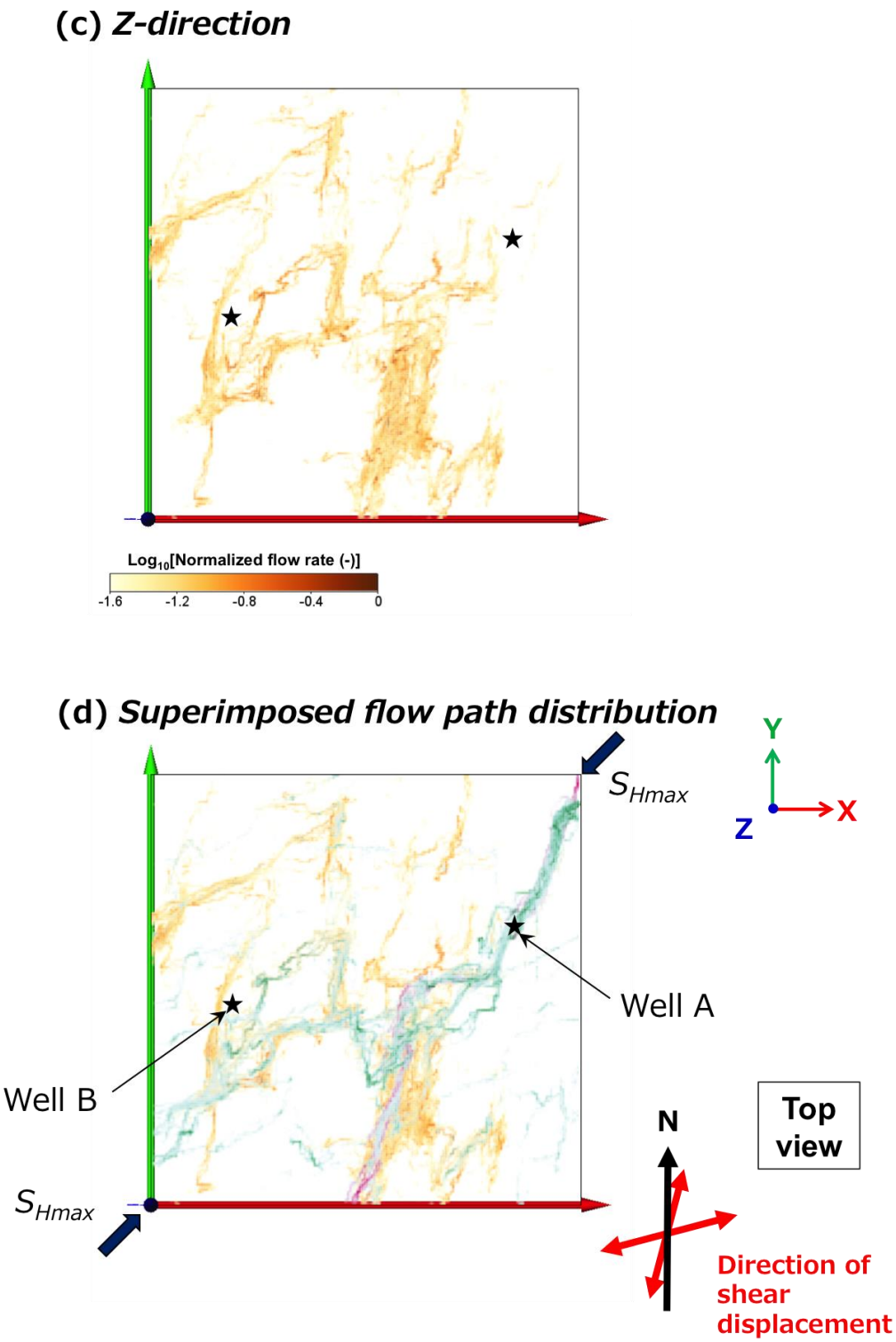

Figure 5-16. (*Continued*)

The reason why the productivity of Well A is higher than that of Well B is clarified in the above. However, the reason of the three orders of magnitude difference in well productivity is still not revealed. To discuss the mechanism causing the significant difference, the result of radial flow simulation with GeoFlow model (Figure 5-11a) is compared with the result evaluated with Conventional DFN model (Figure 5-11b) in detail. As previously mentioned, the significant difference between Figure 5-11a and Figure 5-11b is whether the flow paths towards Well B are formed or not, which reflects the impact of 3-D channeling flow in the fractured reservoir. Considering the fact that the degree of fracture connectivity in all of x-, y-, and z-direction is not so good around Well B, it is expected that the impact of 3-D channeling flow is enormous specifically within the area of low fracture connectivity.

The conceptual diagram of the network of critically-stressed fractures around Well B is shown in Figure 5-17a, where the directions of shear displacement are constrained as shown by arrows. When a rock fracture has a shear displacement, there is an anisotropy in the fluid flow characteristics of the fracture. In other word, the permeability for the parallel flow to the shear displacement ($k_{//}$) is different from the permeability for the perpendicular flow to the shear displacement ($k_{\perp}$). As shown in Figure 5-17b, the grouped contacting asperities are generally arrayed in the perpendicular direction to the shear displacement. Since these contacting asperities become barrier for the parallel flow to the shear displacement, $k_{//}$ is from one to three orders of magnitude less than $k_{\perp}$ [*Nemoto et al.*, 2009]. It is also noted that the parallels flow to the shear displacement is more tortuous than the perpendicular flow to the shear displacement herein. With these in mind, the reality of the fluid flow towards Well B is considered as the following. Although the fracture permeability for the fluid flow in the depth direction is high, this fluid flow doesn't contribute on the production of Well B. This is because the degree of connectivity of critically-stressed fractures is originally low in the depth direction. In contrast, 3-D preferential flow paths are less likely to be formed in the x-direction (i.e. from west side boundary), since the contacting asperities arrayed in the depth direction block the fluid flow in the x-direction. In this manner, as the 3-D preferential flow paths aren't maintained around Well B, the productivity of Well B is significantly low, which results in the three orders of magnitude difference in well productivity. In the case of the Conventional DFN model, the

flow paths towards Well B are, on the other hands, consistently maintained since there is no resistance such as contacting asperities. As a result, the productivity of Well B is overestimated and the three orders of magnitude difference in well productivity is never reproduced.

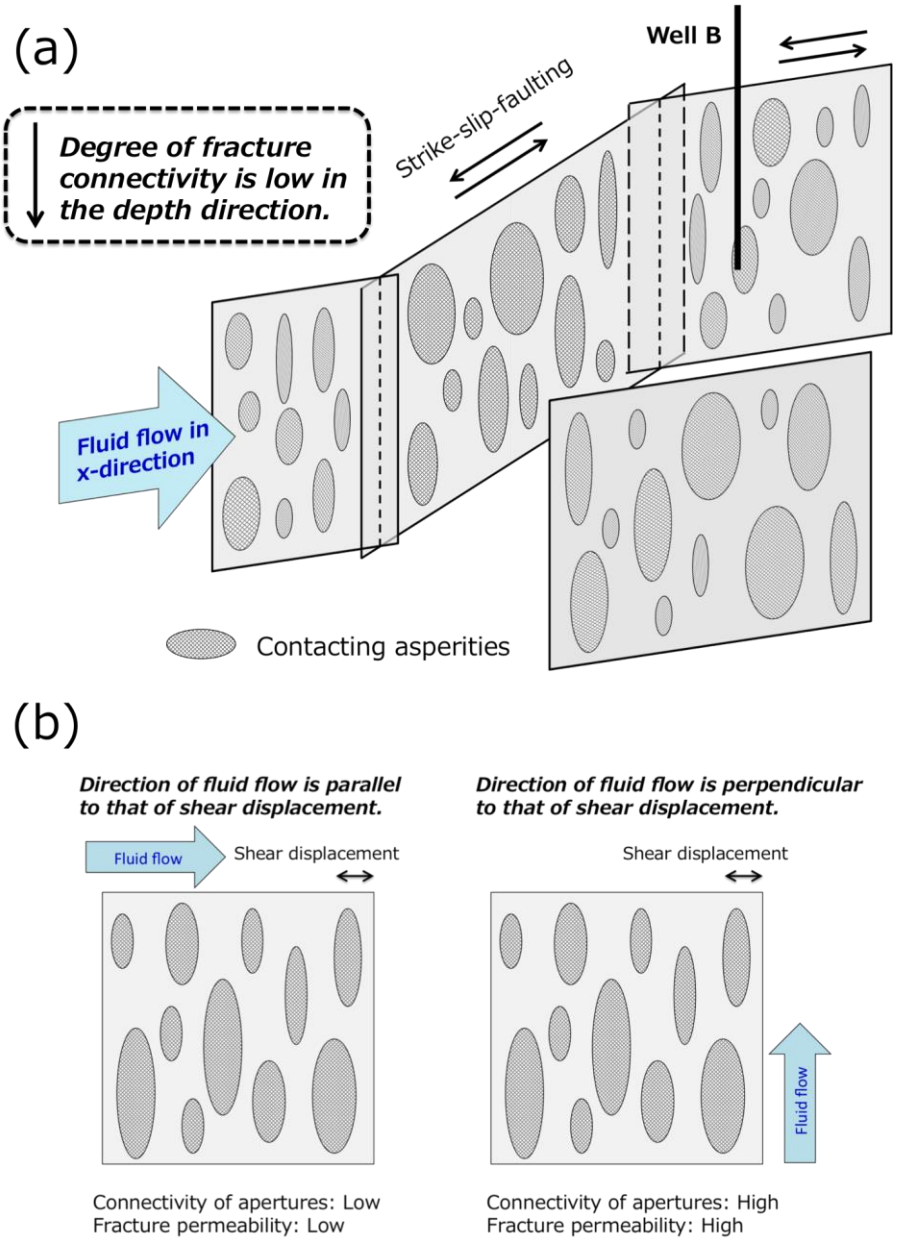

Figure 5-17. (a) Conceptual diagram of the network of critically-stressed fractures around Well B in the Yufutsu oil/gas field, and (b) Schematic illustration for the anisotropy of fluid flow characteristics of a single rock fracture with shear displacement.

Finally, the general impact of 3-D channeling flow in a fractured reservoir is summarized. In a fractured reservoir, 3-D channeling flow consistently occurs, which makes the flow paths quite definitive. In the domain where the degree of fracture connectivity is explicitly high, 3-D preferential flow paths are consistently maintained. Consequently, significantly large productivity is always expected if a well is located for such areas. However, in the domain where the fracture connectivity is relatively limited, it is difficult of the flow paths to be maintained consistently and there is some possibility that the flow paths are vanished due to the occurrence of 3-D channeling flow. When the flow paths aren't formed, good well productivity is never expected. Moreover, even if the hydraulic fracturing is operated in this area, the improvement of the well productivity is not expected since the flow paths aren't developed anew. To consider such an impact of 3-D channeling flow in a fractured reservoir adequately, fluid flows within the reservoir are necessary to be analyzed by GeoFlow or similar concept of DFN model simulatrors.

5.5. Conclusions

Fluid flow in a fractured reservoir (i.e. the Yufutsu oil/gas field) is simulated with GeoFlow model, where heterogeneous aperture distributions are considered for each fractures depending on their scale and shear displacement under confining stress. Through a series of the fluid flow simulations, it is revealed that the reality of fluid flow within a fractured reservoir is 3-D channeling flow, which should be considered for predicting the optimum well locations for a fractured reservoir. Specifically, the impact of 3-D channeling flow is expected to be significant in the domain where the degree of fracture connectivity is relatively limited. Moreover, there are some concerns that we will come to the wrong conclusions for utilization of a fractured reservoir, if the occurrence of 3-D channeling flow within the reservoir is ignored.

As is shown in this study, as long as highly-reliable discrete fracture networks are created for a fractured reservoir on the basis of 3-D seismic data, crustal stress data, and so on, we can now map the realistic flow path distribution (i.e. 3-D channeling flow) with GeoFlow. If such a method is applied to fractured reservoirs of various fields and their results are accumulated, our understandings for 3-D channeling flow in fractured reservoirs are significantly advanced.

Appendix 5-A. Representation of the shapes of rock fractures

In the present study, the shapes of rock fractures are represented by not circles but squares, which should be validated herein. For this validation, two different discrete network models, where rock fractures are modeled by pairs of parallel smooth plates with unique apertures, are prepared; one DFN model is consisted of square rock fractures of 18 different scales (44, 62, 80, 98, 115, 133, 151, 168, 186, 204, 222, 239, 257, 275, 293, 310, 328, and 346 m on a side), which corresponds to the Conventional DFN model, and the other DFN model is consisted of circle rock fractures of 18 different scales (25, 35, 45, 55, 65, 75, 85, 95, 105, 115, 125, 135, 145, 155, 165, 175, 185, and 195 m in radius). The center coordinates and orientations of the individual fractures, which are given so that they coincide with those of *Tamagawa et al.* [2010], are the same between these two models. Radius of a circle fracture is determined so that the area of a circle fracture is equal to that of a corresponding square fracture (Figure A-1), and the shear displacement of 4×10^{-3} (0.4%) is assumed for the critically-stressed fractures. Here, 3 kind of stochastic equivalent discrete fracture networks, which correspond to the aforementioned model number of Network 08, 10, and 14, are used for a series of examinations.

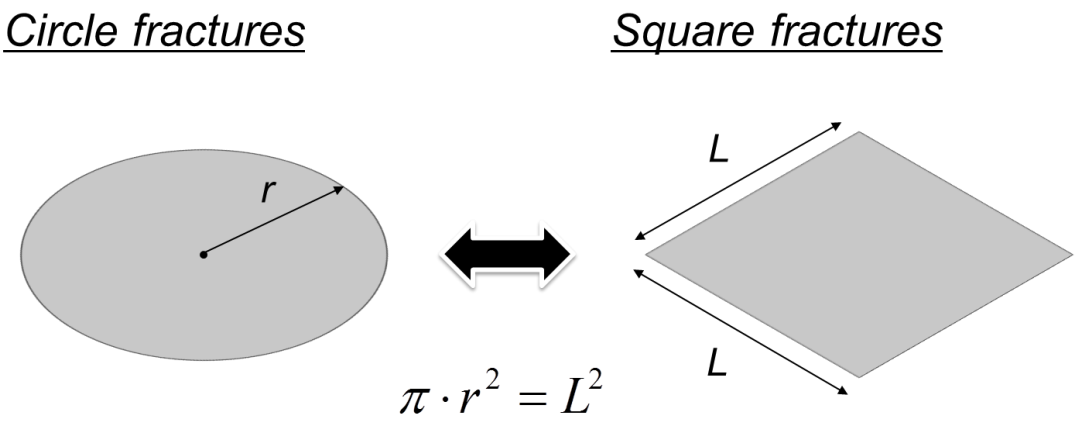

Figure A-1. Conceptual illustration of conversion for the fracture shape.

For both square-shaped fracture network and circle-shaped fracture network, unidirectional fluid flow simulations in the direction of x-axis are conducted. Boundary condition for the unidirectional fluid flow simulation is shown in Figure 5-6a, and the differential pressure, ΔP, is

set to 0.1 MPa. As a result of the fluid flow simulations, the permeability maps and flow path distributions evaluated for 3 kinds of fracture networks are shown in Figure A-2, A-3, and A-4, where appearances of flow path distributions evaluated for the square-shaped fracture networks are similar to those evaluated for the circle-shaped fracture networks. These results indicate that the fluid flow characteristics of fracture networks can be evaluated qualitatively by using whether the square-shaped fracture network or the circle-shaped fracture network.

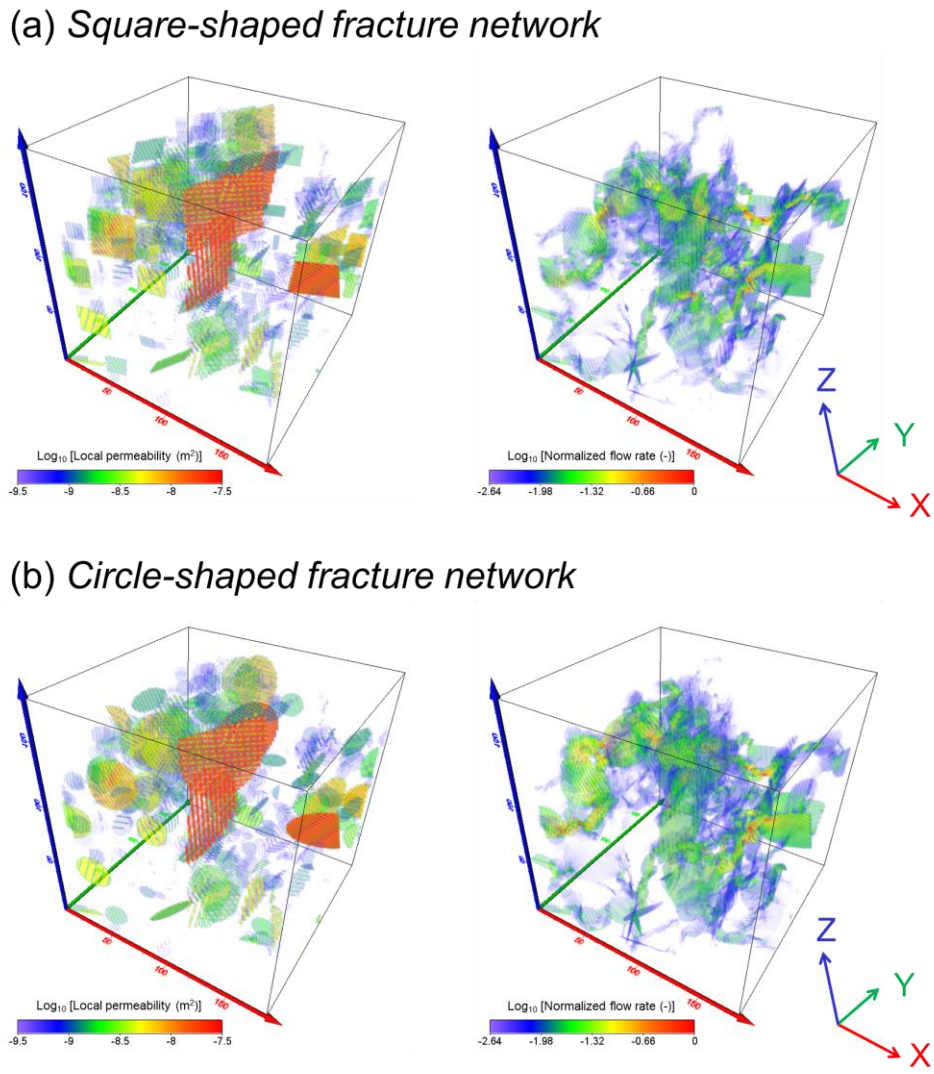

Figure A-2. Permeability maps and flow path distributions evaluated for (a) squared-shaped fracture network and (b) circle-shaped fracture network. Model number of the stochastic equivalent discrete fracture network is Network 08.

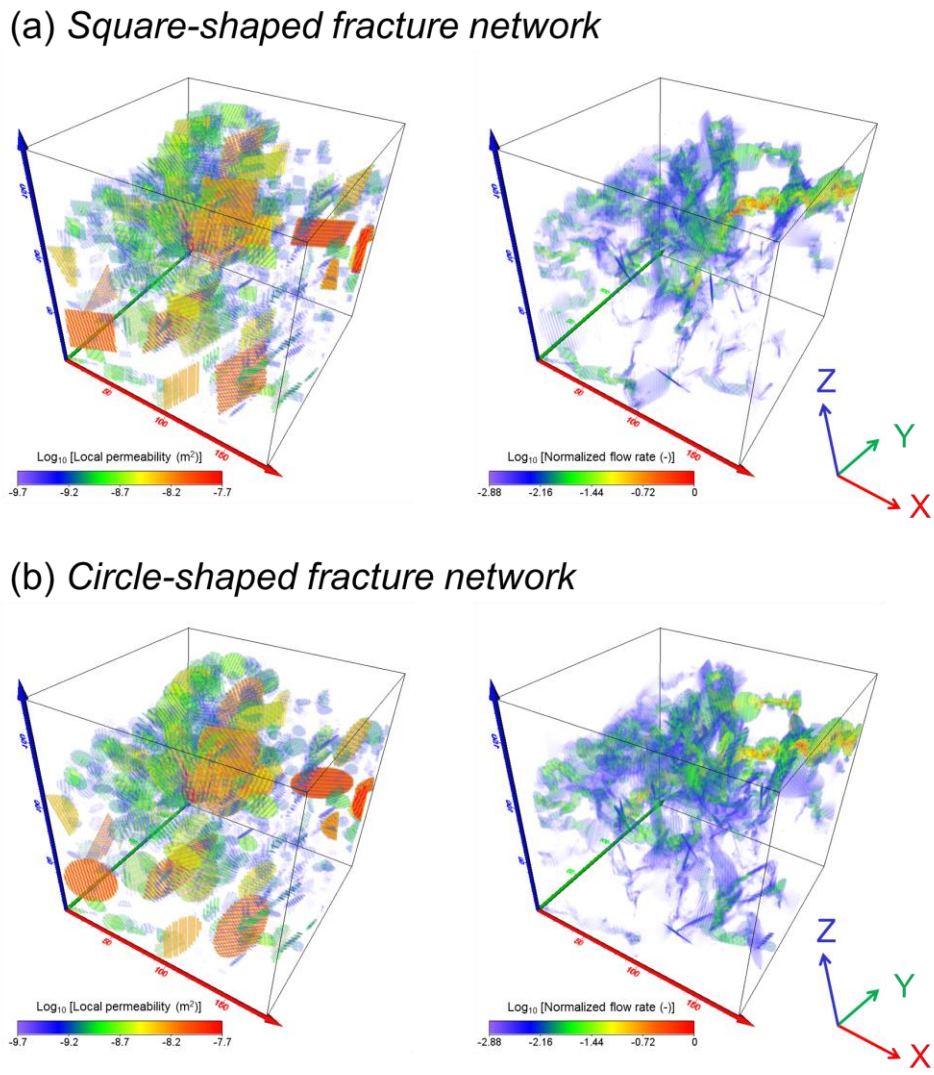

Figure A-3. Permeability maps and flow path distributions evaluated for (a) squared-shaped fracture network and (b) circle-shaped fracture network. Model number of the stochastic equivalent discrete fracture network is Network 10.

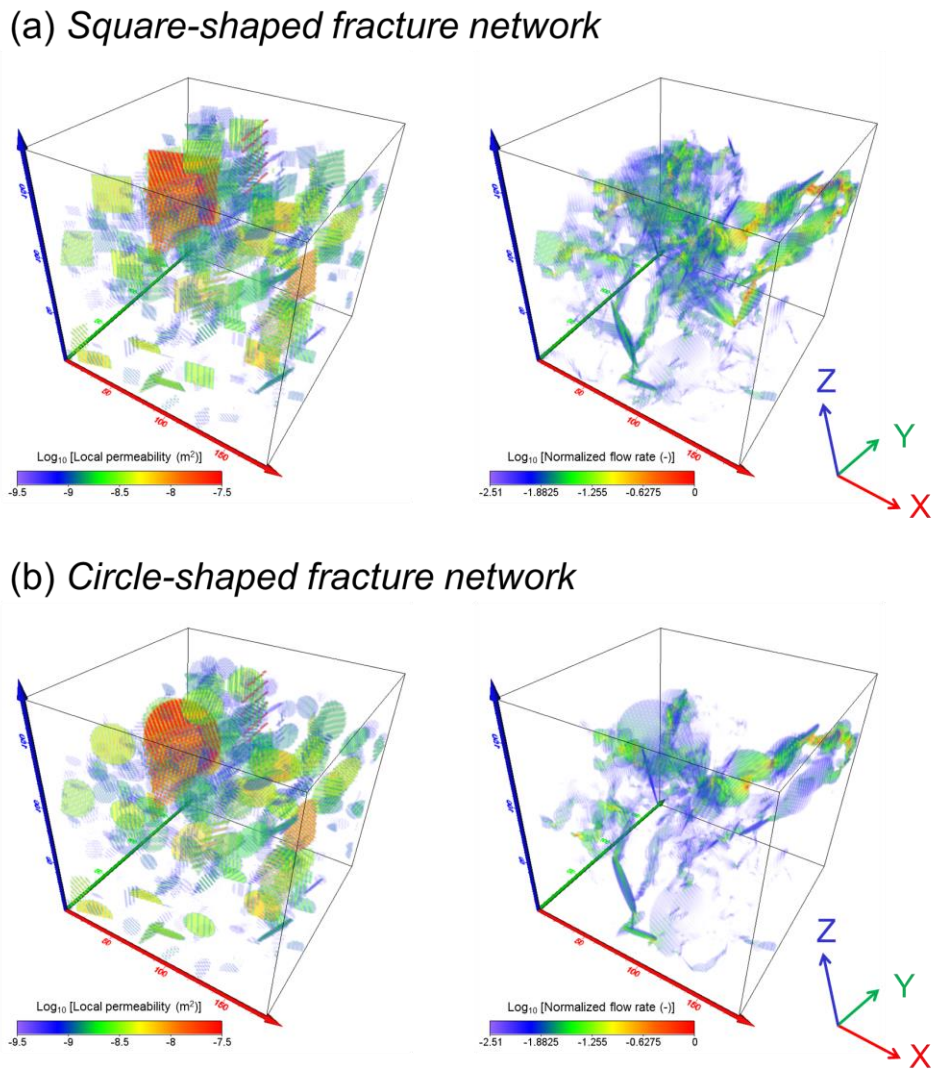

Figure A-4. Permeability maps and flow path distributions evaluated for (a) squared-shaped fracture network and (b) circle-shaped fracture network. Model number of the stochastic equivalent discrete fracture network is Network 14.

In order to quantitatively compare the fluid flow characteristics of these fracture networks, the permeability of the fracture network and the flowing fluid existing volume are evaluated for each simulation and summarized in Table A-1. It is indicated that, for the respective model, the permeability of the fracture network and the flowing fluid existing volume calculated for the square-shaped fracture network are quite similar to those calculated for the circle-shaped fracture network. These results suggest that the fluid flow characteristics of fracture networks

can be also evaluated quantitatively by using whether the square-shaped fracture network or the circle-shaped fracture network. Thus, it is revealed that the shape of rock fracture can be represented by both square and circle in evaluating the fluid flow characteristics of a rock fracture network. In other words, the validity of the present study, where the rock fractures are represented by squares of various scales, is clarified.

Table A-1. Permeabilities of the fracture networks and flowing fluid existing volumes evaluated for squared-shaped fracture network and circle-shaped fracture network.

Model number	Shape of fractures	Permeability [m^2]	Flowing fluid existing volume [%]
Network 08	Square	1.14×10^{-14}	11.9
	Circle	1.08×10^{-14}	11.9
Network 10	Square	1.67×10^{-14}	10.0
	Circle	1.24×10^{-14}	12.6
Network 14	Square	1.72×10^{-14}	10.2
	Circle	1.50×10^{-14}	10.3

Appendix 5-B. Change in the fluid flow characteristics of a fracture network depending on the aperture distributions of individual fractures.

In the present study, when the fracture scale and the shear displacement are specified for a fracture, heterogeneous aperture distribution of the fracture is determined uniquely. However, the heterogeneous aperture distribution indeed varies depending on a series of uniform random number, R_1, which is defined in Eq (A8) in Chapter Ⅲ, even though the fracture scale and the shear displacement are specified. Therefore, it is essential to clarify whether the fluid flow characteristics of a fracture network can be evaluated by using a specific series of aperture distributions or not.

For this clarification, the fracture network which has the same fracture distribution (center coordinates, orientations, and scales of the individual fractures) with that of the aforementioned Network 08 is used herein. In this study, the shear displacement of 4×10^{-3} (0.4%) is assumed for the critically-stressed fractures. Then, 5 sets of stochastic equivalent heterogeneous aperture distributions of rock fractures of various scales are numerically determined (Aperture

distribution 01, Aperture distribution 02, Aperture distribution 03, Aperture distribution 04, and Aperture distribution 05). By considering each set of aperture distributions for the rock fracture network, 5 kinds of discrete fracture networks are created. For the respective fracture networks, unidirectional fluid flow simulations in the direction of x-axis are conducted. Boundary condition for the unidirectional fluid flow simulation is shown in Figure 5-6a, and the differential pressure, ΔP, is set to 0.1 MPa.

As a result of the fluid flow simulations, the permeability maps and flow path distributions evaluated for 5 kinds of fracture networks are shown in Figure A-5. With respect to the permeability maps, it can be found that the distribution of highly-permeable zone within the fracture network varies on a detail depending on the heterogeneous aperture distributions of individual fractures. In contrast, appearances of flow path distributions evaluated for the 5 kinds of fracture networks are remarkably alike in each other. These results indicate that the fluid flow characteristics of fracture networks can be evaluated qualitatively by using representative aperture distributions.

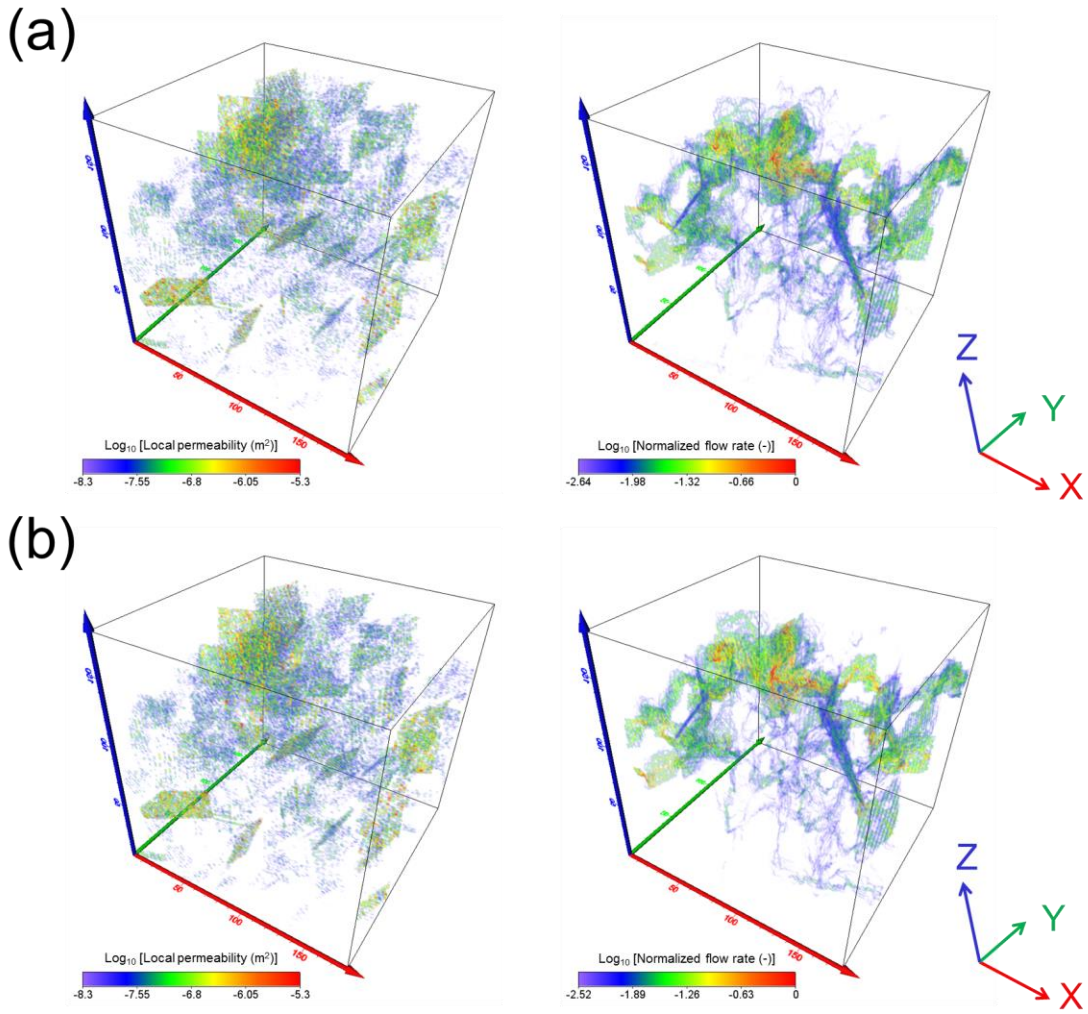

Figure A-5. Permeability maps and flow path distributions evaluated for the fracture network (aforementioned Network 08) where the model number of heterogeneous aperture distributions is (a) Aperture distribution 01, (b) Aperture distribution 02, (c) Aperture distribution 03, (d) Aperture distribution 04, and (e) Aperture distribution 05.

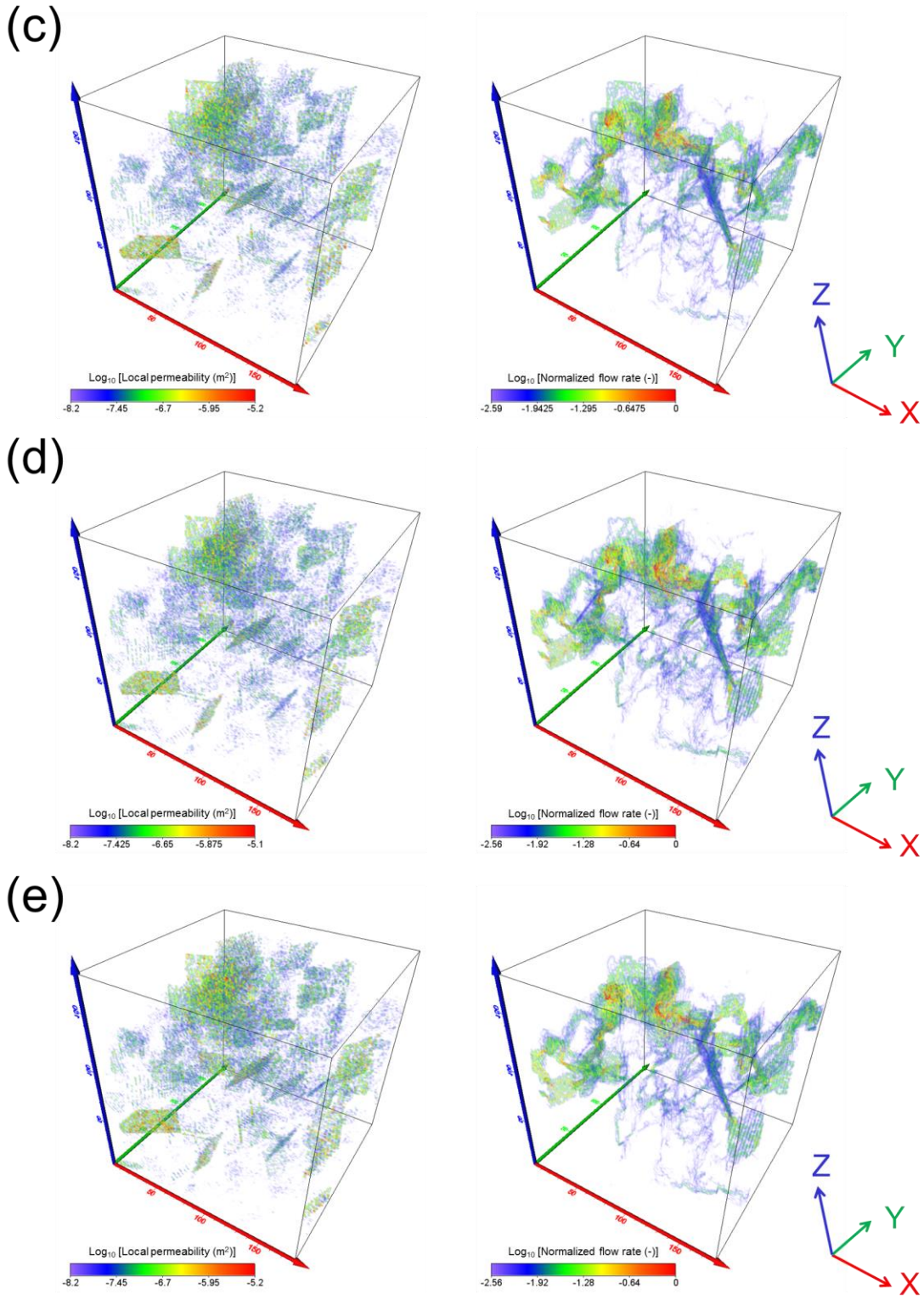

Figure A-5. (*Continued*)

In order to quantitatively compare the fluid flow characteristics of these fracture networks, the permeability of the fracture network and the flowing fluid existing volume are evaluated for each simulation as well and summarized in Table A-2. This table indicates that the permeability of the fracture network and the flowing fluid existing volume calculated for the fracture networks with different aperture distributions are almost all constant regardless of the aperture distributions of individual fractures. These results suggest that the fluid flow characteristics of fracture networks can be evaluated quantitatively by using representative aperture distributions. Thus, the validity of the present study, where the representative heterogeneous aperture distributions of rock fractures are used in evaluating the fluid flow characteristics of a rock fracture network, is also demonstrated.

Table A-2. Permeabilities of the fracture networks and flowing fluid existing volumes evaluated for fracture networks with different sets of aperture distributions.

Model number	Permeability [m^2]	Flowing fluid existing volume [%]
Aperture distribution 01	5.41×10^{-14}	9.1
Aperture distribution 02	5.13×10^{-14}	8.9
Aperture distribution 03	5.57×10^{-14}	8.5
Aperture distribution 04	5.53×10^{-14}	9.2
Aperture distribution 05	5.66×10^{-14}	8.8

Chapter Ⅵ

Conclusions

In the present study, a novel method to analyze and predict three dimensional (3-D) channeling flow in actual fractured reservoirs is developed, where both experimental and numerical approaches are coupled. By using the novel method, the characteristics and impacts of the 3-D channeling flow in fractured reservoirs are revealed.

In Chapter Ⅱ, a fluid flow experiment on a cylindrical granite sample containing two intersecting fractures are conducted. The experimental result demonstrates that 3-D channeling flow must be considered to interpret fluid flow even in the simplest fracture network. To simulate 3-D channeling flow within rock fracture networks, a novel discrete fracture network (DFN) model simulator, GeoFlow, is developed, where rock fractures are modeled by pairs of rough fracture surfaces having heterogeneous aperture distributions. As GeoFlow successfully reproduced the experimental result, which is characterized by considerably uneven fluid flows, the significant potential of GeoFlow to predict 3-D channeling flow in a fracture network is revealed.

In Chapter Ⅲ, insight into the scale dependencies of the aperture distribution and the resulting fluid flow characteristics for rock fractures is obtained under confining stress (up to 30 MPa) on the basis of laboratory investigations for granite fractures with various scales. As a significant result, it is revealed that the contact area in the fracture plane is independent of scale. By combining this characteristics with the fractal nature of the fracture surface, a method for predicting fracture aperture distributions beyond laboratory scale is developed. In this method, the aperture distribution of a fracture of any size can be predicted by simply placing the two fractal fracture surfaces in contact so that the fracture has the scale-independent contact area. The validity of the proposed method was revealed through the reproduction of the results in a laboratory investigation and the maximum aperture-fracture length relations, which have been reported in the literature, for natural fractures (i.e., joints and faults).

In Chapter Ⅳ, aperture distributions and fluid flows are numerically determined for rock fractures with various combination of fracture scale and shear displacement by using the prediction method of fracture aperture distributions beyond laboratory scale, which is developed

in Chapter Ⅲ. Through evaluating the aperture distributions and fluid flows, fluid flow characteristics of subsurface rock fractures under confining stress (up to ~ 100 MPa) are revealed as followings; flow area within a fracture plane is limited to 5-25% regardless of fracture scale (m), l, or shear displacement (m), δ, since preferential flow paths are consistently formed within subsurface rock fractures (i.e. channeling flow). Furthermore, mean aperture (mm), e_m, and permeability (m^2), k, of rock fractures are respectively formulated as $e_{mean} = (1.42 \times 10) \cdot L^{0.66} \cdot (\delta / L)^{0.60}$ and $k = (2.66 \times 10^{-6}) \cdot L^{1.43} \cdot (\delta / L)^{1.21}$, which can reproduce the mean apertures and permeabilities of real fractures. These universal modeling enable us to construct DFNs of a fractured reservoir for GeoFlow simulation.

In Chapter Ⅴ, realistic DFN models, where heterogeneous aperture distributions are given for individual fractures depending on their scale and shear displacement under confining stress, are created for an actual fractured reservoir (i.e. the Yufutsu oil/gas field) and fluid flows in the reservoir are simulated. Through a series of the fluid flow simulations, it is revealed that the reality of fluid flow within a fractured reservoir is 3-D channeling flow, which should be considered for predicting the optimum well locations for a fractured reservoir. Specifically, three order of magnitude difference in the productivities between the neighboring two wells, which is indeed observed in the Yufutsu field, is reproduced successfully for the first time by considering the occurrence of the 3-D channeling flow. Furthermore, it is revealed that we can now map the realistic flow path distribution (i.e. 3-D channeling flow) with GeoFlow, as long as highly-reliable discrete fracture networks are created for a fractured reservoir on the basis of 3-D seismic data, crustal stress data, and so on.

Thus, a novel method to analyze and predict 3-D channeling flow in actual fractured reservoirs is established and our understandings of fluid flow characteristics (i.e. 3-D channeling flow characteristics) in fractured reservoirs are significantly promoted due to the method. Considering the practicality of our suggested method, it is desirable that the method will be applied to fractured reservoirs of various fields hereafter. If such results are accumulated, our understandings for 3-D channeling flow in fractured reservoirs are further advanced. Moreover, as a result, we will be able to predict the location of highly-productive well with significantly high reliability. In the future, it is also desirable that the following relationships are

clarified; (1) 3-D channeling flow and heat extraction, (2) 3-D channeling flow and multi-phase flow and transport process, and (3) 3-D channeling flow and mechanisms of induced seismicity in fractured reservoirs.

References

Abe, H., D. V. Duchane, R. H. Parker, Michio Kuriyagawa (1999a), Present status and remaining problems of HDR/HDR system design, *Geothermics., 28*, 573-590.

Abe, H., H. Niitsuma, and H. Murphy (1999b), Summary of discussions, structured academic review of HDR/HWR reservoirs, *Geothermics., 28*, 671-679.

Abelin, H., I. Neretnieks, S. Tunbrant, and L. Moreno (1985), Migration in a single fracture: Experimental results and evaluation, final report, Stripa Project, Stockholm, Sweden, May 1985.

Agatsuma, T., S. Yokoi, and M. Inaba (2000), Fracture analysis of Yufutsu gas field, *J. Jpn. Assoc. Petrol. Technol., 61(1),* 45-50.

Asanuma, H., H. Muraoka, N. Tsuchiya, and H. Ito (2012), The concept of the Japan Beyond-Brittle Project (JBBP) to develop EGS reservoir in ductile zones, *Geothermal Resources Council Transactions, 36,* 359-364.

Auradou, H., G. Drazer, A. Boshan, J. P. Hulin, and J. Koplik (2006), Flow channeling in a single fracture induced by shear displacement, *Geothermics., 35,* 576-588.

Auradou, H., G. Drazer, J. P. Hulin, and J. Koplik (2005), Permeability anisotropy induced by the shear displacement of rough fracture walls, *Water Resour. Res., 41, W09423*, doi:10.1029/2005WR003938.

Ando, K., A. Kostner, and S. P. Neuman (2003), Stochastic continuum modeling of flow and transport in crystalline rock mass: Fanay-Augeres, France, revisited, *Hydrogeol. J., 11(5), 521-535*, doi:10.1007/s10040-003-0286-0.

Berkowitz, B. (2002), Characterizing flow and transport in fractured geological media: A review, *Adv. Water Resour., 25*, 861-884.

Brown, S. R., R. L. Kranz, and B. P. Bonner (1986), Correlation between the surfaces of natural rock joints, *Geophys. Res. Lett., 13(13),* 1430-1433.

Brown, S. R. (1987a), A note on the description of surface roughness using fractal dimension, *Geophys. Res. Lett., 14,* 1095-1098.

Brown, S. R. (1987b), Fluid flow thorough rock joints: The effect of surface roughness, *J. Geophys. Res., 92(B2),* 1337-1347.

Brown, S. R. (1989), Transport of fluid and electric current through a single fracture, *J. Geophys. Res., 100(B7)*, 9429-9438.

Brown, S. R. (1995), Simple mathematical model of a rough fracture, *J. Geophys. Res., 100(B4)*, 5941-5952.

Brown, S. R., H. W. Stockman, and S. J. Reeves (1995), Applicability of Reynolds equation for modeling fluid flow between rough surfaces, *Geophys. Res. Lett., 22(18)*, 2537-2540.

Brown, S., A. Caprihan, and R. Hardly (1998), Experimental observation of fluid flow channels in a single fracture, *J. Geophys. Res., 103(B3)*, 5125-5132.

Brush, D. J., and N. R. Thomson (2003), Fluid flow in synthetic rough-walled fractures: Navier-Stokes, Stokes, and local cubic law assumptions, *Water Resour. Res., 39(4)*, 1085, doi:10.1029/2002WR001346.

Caine, J. S., J. P. Evans, C. B. Forster (1996), Fault zone architecture and permeability structure, *Geology, 24(11)*, 1025-1028.

Candela, T., F. Renard, Y. Klinger, K. Mair, J. Schmittbuhl, and E. E. Brodsky (2012), Roughness of fault surfaces over nine decades of length scales, *J. Geophys. Res., 117(B08409)*, doi:10.1029/2011JB009041.

Chen, Z., S. P. Narayan, Z. Yang, and S. S. Rahman (2000), An experimental investigation of hydraulic behavior of fractures and joints in granitic rock, *Int. J. Rock Mech. Min. Sci., 37*, 1061-1071.

Cowie, P. A. and C. H. Scholz (1992), Displacement-length scaling relationship for faults: data synthesis and discussion, *J. Struct. Geol., 14(10)*, 1149-1156.

Curewitz, D., and J. A. Karson (1997), Structural settings of hydrothermal outflow: Fracture permeability maintained by fault propagation and interaction, *J. Volcanol. Geotherm. Res., 79*, 149-168.

Cvetkovic, V. and A. Frampton (2010), Transport and retention from single to multiple fractures in crystalline rock at Äspö (Sweden): 2. Fracture network simulations and generic retention model, *Water Resour. Res., 46, W05506*, doi:10.1029/2009WR008030.

Cvetkovic, V., S. Painter, N. Outters, and J. O. Selroos (2004), Stochastic simulation of radionuclide migration in discretely fractured rock near the Äspö hard rock laboratory,

Water Resour. Res., 40, W02404, doi:10.1029/2003WR002655.

Dreuzy, J. R., Y. Méheust, and G. Pichot (2012), Influence of fracture scale heterogeneity on the flow properties of three-dimensional discrete fracture networks (DFN), *J. Geophys. Res., 117(B11207)*, doi:10.1029/2012JB009461.

Durham, W. B. (1997), Laboratory observations of the hydraulic behavior of a permeable fracture from 3800 m depth in the KTB pilot hole, *J. Geophys. Res., 102(B8)*, 18,405-18,416.

Durham, W. B., and B. P. Bonner (1994), Self-propping and fluid flow in slightly offset joints at high effective pressures, *J. Geophys. Res., 99(B5)*, 9391-9399.

Durham, W. B., W. L. Bourcier, and E. A. Burton (2001), Direct observation of reactive flow in a single fracture, *Water Resour. Res., 37(1)*, 1-12.

Elkhoury, J. E., P. Ameli, and R. L. Detwiler (2013), Dissolution and deformation in fractured carbonates caused by flow of CO_2-rich brine under reservoir conditions, *Int . J. Greenh. Gas Con., 16S1*, S203-S215.

Esaki, T., S. Du, Y. Mitani, K. Ikusada, and L. Jing (1999), Development of a shear-flow test apparatus and determination of coupled properties for a single rock joint, *Int. J. Rock Mech. Min. Sci., 36(5)*, 641-650.

Faoro, I., A. Niemeijer, C. Marone, and D. Elsworth (2009), Influence of shear and deviatoric stress on the evolution of permeability in fractured rock, *J. Geophys. Res., 114(B01201)*, doi:10.1029/2007JB005372.

Frampton, A., and V. Cvetkovic (2010), Influence of field-scale fracture transmissivities in crystalline rock using flow log measurements, *Water Resour. Res., 46, W11502*, doi:10.1029/2009WR008367.

Ge, S. (1997), A governing equation for fluid flow in rock fractures, *Water Resour. Res., 33(1)*, 53-61.

Glover, P. W. J., K. Matsuki, R. Hikima, and K. Hayashi (1997), Fluid flow in fractally rough synthetic fractures, *Geophys. Res. Lett., 24(14)*, 1830-1806.

Glover, P. W. J., K. Matsuki, R. Hikima, and K. Hayashi (1998), Synthetic rough fractures in rocks, *J. Geophys. Res., 103(B5)*, 9609-9620.

Huang, S. (2012), Geothermal energy in China, *Nature Clim. Change., 2*, 557-560, doi:10.1038/nclimate1598

Iding, M., and P. Ringrose (2010), Evaluating the impact of fractures on the performance of the In Salah CO_2 storage site, *Int. J. Greenhouse Gas Control, 4*, 242-248, doi:10.1016/j.ijggc.2009.10.016.

Illman, W. A., X. Liu, S. Takeuchi, T.-C. J. Yeh, K. Ando, and H. Saegusa (2009), Hydraulic tomography in fractured granite: Mizunami Underground Research site, Japam, *Water Resour. Res., 45*, W01406, doi:10.1029/2007WR006715.

Ishibashi, T., N. Watanabe, N. Hirano, A. Okamoto, and N. Tsuchiya (2012), GeoFlow: A novel model simulator for prediction of the 3-D channeling flow in a rock fracture network, *Water Resour. Res., 48, W07601*, doi:10.1029/2011WR011226.

Ishibashi, T., T. P. McGuire, N. Watanabe, N. Tsuchiya, and D. Elsworth (2013), Permeability evolution in carbonate fractures: Competing roles of confining stress and fluid pH, *Water Resour. Res., 49*, 1-15, doi:10.1002/wrcr.20253.

Isoe, Y., and R. Onogi (2001), Prediction of the fracture development and fracture network modeling for basement reservoir, off shore Southern Vietnam, *J. Jpn. Assoc. Petrol. Technol., 66(1)*, 15-25.

Ito, Y., K. Obara, K. Shiomi, S. Sekine, H. Hirose (2007), Slow earthquakes coincident with episodic tremors and slow slip events, *Science, 315*, 503, DOI:10.1126/science.1134454

Jaeger, J. C., N. G. W. Cook, and R. W. Zimmerman (2007), Fundamentals of rock mechanics., Wiley-Blackwell.

Jing, Z., J. W. Richards, K. Watanabe, and T. Hashida (2000), A three-dimensional stochastic rock mechanics model of engineered geothermal systems in fractured crystalline rock, *J. Geophys. Res., 105(B10),* 23663-23679.

Johnson, J., S. Brown, and H. Stockman (2006), Fluid flow and mixing in rough-walled fracture intersections, *J. Geophys. Res., 111(B12206),* doi:10.1029/2005JB004087.

Kanamori, H. and D. L. Anderson (1975), Theoretical basis of some empirical relations in seismology, *Bull. Seism. Soc. Am., 65(5),* 1073-1095.

Klimczak, C., R. A. Schultz, R. Parashar ,and D. M. Reeves (2010), Cubic law with

aperture-length correlation: implications for network scale fluid flow, *Hydrogeol J., 18(4),* 851-862.

Kumano, Y., T. Tamagawa and K. Tezuka (2012), Characterization of productive fractures based on geomechanical study at Yufutsu fractured reservoir, *J. Jpn. Assoc. Petrol. Technol., 77(1),* 50-60.

Kuniyasu, M., and Y. Yamada (2004), Structural styles of deep zones in southern central Hokkaido, northern Japan, *J. Jpn. Assoc. Petrol. Technol., 69(2),* 131-144.

Kurita, Y., and S. Yokoi (2000), Cenozoic tectonic settings and a current exploration concept in southern central Hokkaido, northern Japan, *J. Jpn. Assoc. Petrol. Technol., 65(2),* 58-70.

Konzuk, J. S., and B. H. Kueper (2004), Evaluation of cubic law based models describing single-phase flow through a rough-walled fracture, *Water Resour. Res., 40,* W02402, doi:10.1029/2003WR002356.

Koyama, T., I. Neretnieks, and L. Jing (2008), A numerical study on differences in using Navier-Stokes and Reynolds equations for modeling the fluid flow and particle transport in single rock fractures with shear, *Int. J. Rock Mech. Min. Sci., 45,* 1082-1101.

Kumar, S., and G. S. Bodvarsson (1990), Fractal study and simulation of fracture roughness, *Geophys. Res. Lett., 17(6),* 701-704.

Long, J. C. S., J. S. Remer, C. R. Wilson, and P. A. Witherspoon (1982), Porous media equivalents for networks of discontinuous fractures, *Water Resour. Res., 18(3),* 645-658.

Manga, M., I. Beresnev, E. E. Brodsky, J. E. Elkhoury, D. Elsworth, S. E. Ingebritsen, D. C. Mays, and C-Y. Wang (2012), Change in permeability caused by transient stresses: Field observations, experiments, and mechanisms, *Rev. Geophys., 50, 2,* doi:10.1029/2011RG000382.

Matsuki, K., Y. Chida, K. Sakaguchi, and P. W. J. Glover (2006), Size effect on aperture and permeability of a fracture as estimated in large synthetic fractures, *Int. J. Rock Mech. Min. Sci., 43(5),* 726-755.

Matsuura, T., K. Tezuka, and T. Tamagawa (2003), Naturally fractured reservoir modeling using static and dynamic data, *J. Jpn. Assoc. Petrol. Technol., 68(6),* 479-488.

Min, K. B., J. Rutqvist, C.-F. Tsang, and L. Jinga (2004), Stress-dependent permeability of

fractured rock masses: a numerical study, *Int. J. Rock Mech. Min. Sci., 41,* 1191-1210.

Morris, J. P., L. J. Pyrak-Nolte, N. J. Giordano, J.-T. Cheng, J. Tran, and A. Lumsdaine (1999), Fracture geometry and relative permeabilities: Application to multiphase flow through coal, Paper 9943 presented at the 1999 Coalbed Methane Symposium, Tuscaloosa (United States), May.

Nakaya, S., and K. Nakamura, Percolation conditions in fractured hard rocks: A numerical approach using the three-dimensional binary fractal fracture network (3D-BFFN) model, *J. Geophys. Res., 112,* B12203, doi:10.1029/2006JB004670.

Nemoto, K., N. Watanabe, N. Hirano, and N. Tsuchiya (2009), Direct measurement of contact area and stress dependence of anisotropic flow through rock fracture with heterogeneous aperture distribution, *Earth Planet. Sci. Lett., 281,* 81-87.

Neuman, S. P. (2005), Trends, prospects and challenges in quantifying flow and transport through fractured rocks, *Hydrogeol. J., 13(1),* 124-147, doi:10.1007/s10040-004-0397-2.

Niitsuma, H., M. Fehler, R. Jones, S. Wilson, J. Albright, A. Green, R. Baria, K. Hayashi, H. Kaieda, K. Tezuka, A. Jupe, T. Wallroth, F. Cornet, H. Asanuma, H. Moriya, K. Nagano, W. S. Phillips, J. Rutledge, L. House, A. Beauce, *et al.* (1999), Current status of seismic and borehole measurements for HDR/HWR development, *Geothermics., 28,* 475-490.

Oron, A. P., and B. Berkowitz (1998), Flow in rock fractures: The local cubic law assumption reexamined, *Water Resour. Res., 34(11),* 2811-2825.

Plouraboué, F., P. Kurowski, J. M. Boffa, J. P. Hulin, and S. Roux (2000), Experimental study of the transport properties of rough self-affine fractures, *J. Contam. Hydrol., 46(3),* 295-318.

Power, W. L., T. E. Tullis, S. R. Brown, G. N. Boitnott, and C. H. Scholz (1987), Roughness of natural fault surfaces, *Geophys. Res. Lett., 14(1),* 29-32, doi:10.1029/GL014i001p00029.

Power, W. L., and W. B. Durham (1997), Topography of natural and artificial fractures in granitic rocks: Implications for studies of rock friction and fluid migration, *Int. J. Rock Mech. Min. Sci., 34(6),* 979-989.

Pyrak-Nolte, L. J., and J. P. Morris (2000), Single fractures under normal stress: The relation between fracture specific stiffness and fluid flow, *Int. J. Rock Mech. Min. Sci., 37(1-2),* 245-262.

Pyrak-Nolte, L. J., N. G. W. Cook, and D. D. Nolte (1988), Fluid percolation through single fractures, *Geophys. Res. Lett., 15(11),* 1247-1250.

Raven, K. G., and J. E. Gale (1985), Water flow in natural rock fracture as a function of stress and sample size, *Int. J. Rock Mech. Min. Sci., 22(4),* 251-261.

Renald, F., T. Candela, and E. Bouchaud (2013), Constant dimensionality of fault roughness from the scale of micro-fractures to the scale of continents, *Geophys. Res. Lett., 40,* doi:10.1029/2012GL054143.

Peitgen, H. O., and D. Saupe (1988), The science of fractal images., Springer, New York.

Sausse, J. (2002), Hydromechanical properties and alteration of natural fracture surfaces in the Soultz granite (Bas-Rhin, France), *Tectonophysics, 348(1),* 169-185.

Schlische, R. W., S. S. Young, R. V. Ackermann, and A. Gupta (1996), Geometry and scaling relations of a population of very small rift-related normal faults, *Geology, 24(8),* 683-686.

Scholz, C. H. (2002), The mechanics of the earthquakes and faulting., Cambridge Univ Press, Cambridge.

Schultz, R. A., R. Soliva, H. Fossen, C. H. Okubo, D. M. Reeves (2008), Dependence of displacement-length scaling relations for fractures and deformation bands on the volumetric changes across them, *J. Struct. Geol., 30,* 1405-1411.

Shiomoto, Y., T. Aoyama, and H. Seki (2006), Model development for fractured crystalline rock reservoir, Rang Dong Field, Offshore Vietnam, *J. Jpn. Assoc. Petrol. Technol., 71(1),* 94-106.

Stockman, H.W., J. Johnson., and S. R. Brown (2001), Mixing at fracture intersections: influence of channel geometry and the Reynolds and Peclet numbers, *Geophys. Res. Lett., 28(22),* 4299-4320.

Takahashi, M., A. Hirata, and H. Koide (1990), Effect of confining pressure and pore pressure on permeability of Inada granite, *Journal of the Japan Society of Engineering Geology., 31(3),* 105-114 (in Japanese with English abstract).

Talon, L., H. Auradou, and A. Hansen (2010), Permeablity estimates of self-affine fracture faults based on generalization of the bottle neck concept, *Water Resour. Res., 46,* W07601, doi:10.1029/2009WR008404.

Tamagawa, T., K. Tezuka, and N. Tsuchiya (2012), Use of a computational fault-extraction process with calibrations o characterize a fractured basement reservoir, Yufutsu, Japan, *AAPG Bulletin*, *96(12)*, 2275-2296.

Tamagawa, T., K. Yoshioka, and K. Tezuka (2010), Estimation of fault-related fractures using automatic fault-extraction process with acoustic emission data in the Yufutsu oil/gas field, *J. Jpn. Assoc. Petrol. Technol., 75(6)*, 462-471.

Tezuka, K., and T. Tamagawa (2004), Feasibility of fracture delineation by Acoustic Emission method in oil/gas reservoir, *J. Jpn. Assoc. Petrol. Technol., 69(6)*, 635-646.

Tsang, C. F., and I. Neretnieks (1998), Flow channeling in heterogeneous fractured rocks, *Rev. Geophys., 36*, 275-298.

Tsang, Y. W., and P. A. Witherspoon (1981), Hydromechanical behavior of a deformable rock fracture subject to normal stress, *J. Geophys. Res., 86(B10)*, 9287-9298.

Vermilye, J. M., and C. H. Scholz (1995), Relation between vein length and aperture, *J. Struct. Geol., 17(3)*, 423-434.

Vesselinov, V. V., S. P. Neuman, and W. A. Illman (2001), Three-dimensional numerical inversion of pneumatic cross-hole tests in unsaturated fractured tuff 2. Equivalent parameters, high-resolution stochastic imaging and scale effects, *Water Resour. Res., 37(12)*, 3019-3042, doi:10.1029/2000WR000135.

Walsh, R., C. McDermott, and O. Kolditz (2008), Numerical modeling of stress-permeability coupling in rough fractures, *Hydrogeol. J., 16*, 613-627.

Wang, J. S. Y., T. N. Narashimhan, C. H. Scholz (1988), Aperture correlation of a fractal fracture, *J. Geophys. Res., 93(B3)*, 2216-2224.

Watatnabe, N., N. Hirano, and N. Tsuchiya (2008), Determination of aperture structure and fluid flow in a rock fracture by high-resolution numerical modeling on the basis of a flow-thorough experiment under confining pressure, *Water Resour. Res., 44, W06412*, doi:10.1029/2006WR005411.

Watanabe, N., N. Hirano, and N. Tsuchiya (2009), Diversity of channeling flow in heterogeneous aperture distribution inferred from integrated experimental-numerical analysis on flow through shear fracture in granite, *J. Geophys. Res., 114*, B04208,

doi:10.1029/2008JB005959.

Watanabe, N., T. Ishibashi, N. Hirano, N. Tsuchiya, Y. Ohsaki, T. Tamagawa, Y. Tsuchiya, H. Okabe (2011a), Precise 3D numerical modeling of fracture flow coupled with X-ray Computed tomography for reservoir core samples, *SPE Journal, 16(3),* 683-691, doi:10.2118/146643-PA.

Watanabe, N., T. Ishibashi, Y. Ohsaki, N. Y. Tsuchiya, T. Tamagawa, N. Hirano, H. Okabe, N. Tsuchiya (2011b), X-ray CT based numerical analysis of fracture flow for core samples under various confining pressure, *Engineering Geology, 123,* 338-346, doi:10.1016/j.enggeo.2011.09.010.

Watanabe, N., T. Ishibashi, N. Tsuchiya, Y. Ohsaki, T. Tamagawa, Y. Tsuchiya, H. Okabe, H. Ito (2012), Geologic core holder with CFR PEEK body for the X-ray CT based numerical analysis of fracture flow under confining pressure, *Rock Mechanics and Rock Engineering, 46(2),* 413-418, doi:10.1007/s00603-012-0311-5.

Witherspoon, P. A., C. J. Amick, J. E. Gale, and K. Iwai (1979), Observations of a potential size effect in experimental determination of the hydraulic properties of fractures, *Water Resour. Res., 15(5),* 1142-1146.

Witherspoon, P. A., J. S. Y. Wang, K. Iwai, and J. E. Gale (1980), Validity of cubic law for fluid flow in a deformable rock fracture, *Water Resour. Res., 16(6),* 1016-1024.

Yanagimoto, Y., and A. Iijima (2003), Hydrothermal laumontization and microfracture formation in reservoir rocks at the Yufutsu field, Hokkaido, northern Japan, *J. Petrol Geol., 26,* 351-372.

Yasuhara, H., A. Polak, Y. Mitani, A. G. Grader, P. M. Halleck, and D. Elsworth (2006), Evolution of fracture permeability through fluid-rock reaction under hydrothermal conditions, *Earth Planet. Sci. Lett., 244,* 186-200.

Yeo, I. W., M. H. de Freitas, and R. W. Zimmerman (1998), Effect of shear displacement on the aperture and permeability of a rock fracture, *Int. J. Rock Mech. Min. Sci., 35(8),* 1051-1070.

Zimmerman, R. W., D. W. Chen, and N. G. W. Cook (1992), The effect of contact area on the permeability of fractures, *J. Hydrol., 139,* 79-96.

Publications

Papers with peer review

Ishibashi, T., N. Watanabe, N. Hirano, A. Okamoto, and N. Tsuchiya (2012), GeoFlow: A novel model simulator for prediction of the 3-D channeling flow in a rock fracture network, *Water Resources Research, 48,* W07601, doi:10.1029/2011WR011226.

Ishibashi, T., T. P. McGuire, N. Watanabe, N. Tsuchiya, and D. Elsworth (2013), Permeability evolution in carbonate fractures: Competing roles of confining stress and fluid pH, *Water Resources Research, 49,* 1-15, doi:10.1002/wrcr.20253.

Watanabe, N., T. Ishibashi, N. Hirano, N. Tsuchiya, Y. Ohsaki, T. Tamagawa, Y. Tsuchiya, H. Okabe (2011), Precise 3D numerical modeling of fracture flow coupled with X-ray Computed tomography for reservoir core samples, *SPE Journal, 16(3),* 683-691, doi:10.2118/146643-PA.

Watanabe, N., T. Ishibashi, Y. Ohsaki, N. Y. Tsuchiya, T. Tamagawa, Hirano, H. Okabe, N. Tsuchiya (2011), X-ray CT based numerical analysis of fracture flow for core samples under various confining pressure, *Engineering Geology, 123,* 338-346, doi:10.1016/j.enggeo.2011.09.010.

Watanabe, N., T. Ishibashi, N. Tsuchiya, Y. Ohsaki, T. Tamagawa, Y. Tsuchiya, H. Okabe, H. Ito (2012), Geologic core holder with CFR PEEK body for the X-ray CT based numerical analysis of fracture flow under confining pressure, *Rock Mechanics and Rock Engineering, 46(2),* 413-418, doi:10.1007/s00603-012-0311-5.

渡邉則昭，石橋琢也，土屋範芳，玉川哲也　(2013), GeoFlowを用いたき裂型貯留層における優先流路分布の評価，石油技術協会誌，*78(6)*，482−490.

Papers with peer review (Proceedings)

Ishibashi, T., N. Watanabe, N. Hirano, A. Okamoto, and N. Tsuchiya, Development of a Discrete Fracture Network Model Simulator “GeoFlow” for Evaluation of Three Dimensional Channeling Flow, *Proc. International Petroleum Technology Conference*, IPTC13143, 2009

Hirano, N., T. Ishibashi, N. Watanabe, A. Okamoto, and N. Tsuchiya, New Concept Discrete Fracture Network Model Simulator, GeoFlow, and Three Dimensional Channeling Flow in Fracture Network, *Proceedings World Geothermal Congress 2010*, Number 2249, 2010

Ishibashi, T., N. Watanabe, N. Hirano, A. Okamoto, and N. Tsuchiya, Experimental and Numerical Evaluation of Channeling Flow in Fractured Type of Geothermal Reservoir, *Proc.*

of 37th Workshop on Geothermal Reservoir Engineering (Stanford University), 759-766, 2012

Ishibashi, T., N. Watanabe, N. Hirano, A. Okamoto, and N. Tsuchiya, Upgrading of Aperture Model Based on Surface Geometry of Natural Fracture for Evaluating Channeling Flow, *Geothermal Resources Council Transactions, 36*, 481-486, 2012

Watanabe, N., K. Sakurai, T. Ishibashi, and N. Tsuchiya, Relative Permeability Measurement and Numerical Modeling of Two-Phase Flow through Variable Aperture Fracture in Granite under Confining Pressure, *Geothermal Resources Council Transactions, 36*, 583-587, 2012

Ishibashi, T., T. P. McGuire, N. Watanabe, N. Tsuchiya, and D. Elsworth, Time-dependent Permeability of Carbonate Fracture Influenced by Stress and pH, *Proc. 6th International Symposium on In-Situ Rock Stress*, 484-489, 2013

Watanabe, N., K. Sakurai, T. Ishibashi, and N. Tsuchiya, Experimental and Numerical Determination of Relative Permeability Curves for Two-phase Flow through a Rock Fracture under Confining Pressure, *Proc. 6th International Symposium on In-Situ Rock Stress*, 524-533, 2013

Paper without peer review

Ishibashi, T., N. Watanabe, N. Hirano, A. Okamoto, and N. Tsuchiya, Three Dimensional Analysis of Channeling Flow by New Discrete Fracture Network Model Simulator, GeoFlow, *Proc. The 15th Formation Evaluation Symposium of Japan*, Paper N, 2009

Ishibashi, T., N. Watanabe, N. Hirano, A. Okamoto, and N. Tsuchiya, Evaluation of Three Dimensional Channeling Flow by New Concept Discrete Fracture Network Model Simulator, GeoFlow, *Proceedings of the Renewable Energy 2010*, Paper O-Ge-2-3, 2010

Watanabe, N., T. Ishibashi, Y. Ohsaki, Y. Tsuchiya, T. Tamagawa, N. Hirano, H. Okabe, and N. Tsuchiya, Analysis of Fracture Flow within Reservoir Core Sample under Confining Pressure by Numerical Modeling Coupled with X-ray Computed Tomography, *Proc. The 16th Formation Evaluation Symposium of Japan*, Paper G, 2010

Ishibashi, T., N. Watanabe, N. Hirano, A. Okamoto, and N. Tsuchiya, Evaluation and Prediction of Fluid Flow through Fracture under Confining Pressure in Various Scales, *Proc. The 17th Formation Evaluation Symposium of Japan*, Paper N, 2011

Watanabe, N., T. Ishibashi, N. Tsuchiya, Y. Ohsaki, T. Tamagawa, Y. Tsuchiya, H. Okabe, and H. Ito, Development of CFR-PEEK Core Holder for X-ray CT Based Numerical Analysis of Fluid Flow within Fractured Samples under Confining Pressure, *Proc. The 17th Formation Evaluation Symposium of Japan, Chiba*, Paper C, 2011

Ishibashi, T., N. Watanabe, T. Tamagawa, N. Hirano, A. Okamoto, and N. Tsuchiya, Impact of

3D Channeling Flow on Well Productivity in the Yufutsu oil/gas field, *Proc. The 18th Formation Evaluation Symposium of Japan*, Paper K, 2012

Watanabe, N., K. Sakurai, T. Ishibashi, and N. Tsuchiya, Experimental and Numerical Investigation of Two-Phase Flow in a Rock Fracture under Confining Pressure, *Proc. The 18th Formation Evaluation Symposium of Japan*, Paper G, 2012

Sakurai, K., N. Watanabe, T. Ishibashi, N. Tsuchiya, Y. Ohsaki, T. Tamagawa, and M. Yagi, Oil-water Relative Permeability Curves for Fractures in Granite and Limestone at Diffrenial Instric Permeabilities, *Proc. The 19th Formation Evaluation Symposium of Japan*, Paper I, 2013

Oral presentations in international conferences

Ishibashi, T., N. Watanabe, N. Hirano, A. Okamoto, and N. Tsuchiya, Three Dimensional Analysis of Channeling Flow by New Discrete Fracture Network Model Simulator, GeoFlow, The 15th Formation Evaluation Symposium of Japan, Chiba, Japan, October 2009

Ishibashi, T., N. Watanabe, N. Hirano, A. Okamoto, and N. Tsuchiya, Evaluation of Three Dimensional Channeling Flow by New Concept Discrete Fracture Network Model Simulator, GeoFlow, Renewable Energy 2010, Yokohama, Japan, June 2010

Watanabe, N., T. Ishibashi, Y. Ohsaki, Y. Tsuchiya, T. Tamagawa, N. Hirano, H. Okabe, and N. Tsuchiya, Analysis of Fracture Flow within Reservoir Core Sample under Confining Pressure by Numerical Modeling Coupled with X-ray Computed Tomography, The 16th Formation Evaluation Symposium of Japan, Chiba, Japan, September 2010 (Best Paper)

Ishibashi, T., N. Watanabe, N. Hirano, A. Okamoto, and N. Tsuchiya, Evaluation and Prediction of Fluid Flow through Fracture under Confining Pressure in Various Scales, The 17th Formation Evaluation Symposium of Japan, Chiba, Japan, September 2011 (Best Student Award, Best Paper)

Watanabe, N., T. Ishibashi, N. Tsuchiya, Y. Ohsaki, T. Tamagawa, Y. Tsuchiya, H. Okabe, and H. Ito, Development of CFR-PEEK Core Holder for X-ray CT Based Numerical Analysis of Fluid Flow within Fractured Samples under Confining Pressure, The 17th Formation Evaluation Symposium of Japan, Chiba, Japan, September 2011

Ishibashi, T., N. Watanabe, N. Hirano, A. Okamoto, and N. Tsuchiya, Experimental and Numerical Evaluation of Channeling Flow in Fractured Type of Geothermal Reservoir, The 37th Stanford Geothermal Workshop, Stanford, USA, January 2012

Ishibashi, T., N. Watanabe, T. Tamagawa, N. Hirano, A. Okamoto, and N. Tsuchiya, Impact of

3D Channeling Flow on Well Productivity in the Yufutsu oil/gas field, The 18th Formation Evaluation Symposium of Japan, Chiba, Japan, September 2012

Watanabe, N., K. Sakurai, T. Ishibashi, and N. Tsuchiya, Experimental and Numerical Investigation of Two-Phase Flow in a Rock Fracture under Confining Pressure, The 18th Formation Evaluation Symposium of Japan, Chiba, Japan, September 2012

Watanabe, N., K. Sakurai, T. Ishibashi, and N. Tsuchiya, Relative Permeability Measurement and Numerical Modeling of Two-Phase Flow through Variable Aperture Fracture in Granite under Confining Pressure, Geothermal Resources Council 2012 Annual Meeting, Reno, USA, October 2012

Elsworth, D., T. P. McGuire, T. Ishibashi, Z. Karcz, N. Tsuchiya, J. Taron, H. Yasuhara, K. Kishida, and Z. Zhong, Evolution of Permeability and Strength in Fractured Rocks: Reinforcing and Competing Roles of Stress, Temperature and Fluid Reactivity, The 47th US Rocks Mechanics Geomechanics Symposium, San Francisco, USA, June 2013

Ishibashi, T., T. P. McGuire, N. Watanabe, N. Tsuchiya, and D. Elsworth, Time-dependent Permeability of Carbonate Fracture Influenced by Stress and pH, 6th International Symposium on In-Situ Rock Stress, Sendai, Japan, August 2013

Watanabe, N., K. Sakurai, T. Ishibashi, and N. Tsuchiya, Experimental and Numerical Determination of Relative Permeability Curves for Two-phase Flow through a Rock Fracture under Confining Pressure, 6th International Symposium on In-Situ Rock Stress, Sendai, Japan, August 2013

Sakurai, K., N. Watanabe, T. Ishibashi, N. Tsuchiya, Y. Ohsaki, T. Tamagawa, and M. Yagi, Oil-water Relative Permeability Curves for Fractures in Granite and Limestone at Diffrenial Instric Permeabilities, The 19th Formation Evaluation Symposium of Japan, Chiba, Japan, September 2013

Poster presentations in international conferences

Watanabe, N., T. Ishibashi, N. Hirano, A. Okamoto, and N. Tsuchiya, Development of a Discrete Fracture Network Model Simulator for 3D Channeling Flow through Rock Fractures with Heterogeneous Aperture Distributions, 6th International Workshop on WATER DYNAMICS, Sendai, Japan, March 2009

Ishibashi, T., N. Watanabe, N. Hirano, A. Okamoto, and N. Tsuchiya, Development of a Discrete Fracture Network Model Simulator “GeoFlow” for Evaluation of Three Dimensional Channeling Flow, International Petroleum Technology Conference, Doha, Qatar, December

2009

Hirano, N., T. Ishibashi, N. Watanabe, A. Okamoto, and N. Tsuchiya, New Concept Discrete Fracture Network Model Simulator, GeoFlow, and Three Dimensional Channeling Flow in Fracture Network, World Geothermal Congress 2010, Bali, Indonesia, April 2010

Ishibashi, T., N. Watanabe, N. Hirano, A. Okamoto, and N. Tsuchiya, Visualization of Three Dimensional Channeling Flow in Fracture System by New Concept Model Simulator, GeoFlow, G-COE Symposium 2010 Dynamic Earth and Heterogeneous Structure, Sendai, Japan, July 2010

McGuire, T. P., T. Ishibashi, D. Elsworth, Z. Karcz, and N. Tsuchiya, Permeability Evolution in Carbonates: Competing Roles of Stress and Fluid Reactivity, Hedberg Conference on Fundamentals of Flow in Carbonates, Provence, France, July 2012

Ishibashi, T., N. Watanabe, N. Hirano, A. Okamoto, and N. Tsuchiya, Upgrading of Aperture Model Based on Surface Geometry of Natural Fracture for Evaluating Channeling Flow, Geothermal Resources Council 2012 Annual Meeting, Reno, USA, October 2012

Ishibashi, T., N. Watanabe, T. Tamagawa, N. Hirano, A. Okamoto, and N. Tsuchiya, Challenge to analysis of 3-D channeling flow through fractured type of reservoir by GeoFlow, 10th International Workshop on WATER DYNAMICS (Deep Carbon Cycle/Geosphere Pollution)&ICDP Japan Beyond-Brittle Project, Sendai, Japan, March 2013

Ishibashi, T., N. Watanabe, N. Tsuchiya, and T. Tamagawa, Evaluation of the 3-D Channeling Flow in a Fractured Type of Oil/Gas Reservoir, 2013AGU Fall meeing, San Francisco, USA, December 2013

Oral presentations in domestic conferences

平野伸夫，石橋琢也，渡邉則昭，土屋範芳，シミュレーションを用いた三次元チャネリングフローの可視化，資源・素材学会　平成21年度春季大会，津田沼（千葉），2009年3月

渡邉則昭，石橋琢也，平野伸夫，岡本敦，土屋範芳，不均質間隙構造を有する地下き裂系における3次元チャネリングフロー，日本地球惑星科学連合　2009年大会，幕張（千葉），2009年5月

石橋琢也，渡邉則昭，平野伸夫，岡本敦，土屋範芳，　3次元チャネリングフロー解析のためのDFNシミュレータ“GeoFlow”の開発，石油技術協会　平成21年度春季講演会，代々木（東京），2009年6月　（石油技術協会優秀発表賞）

平野伸夫，石橋琢也，渡邉則昭，土屋範芳，岩石き裂内流体流動と岩石−水反応場（FWS），

日本鉱物学会　2009年年会，札幌（北海道），2009年9月

渡邉則昭，石橋琢也，平野伸夫，岡本敦，土屋範芳，岩石き裂の不均質間隙構造におけるチャネリングフロー, JAMSTEC IFREE=KANAME 特別セミナー, 横浜（神奈川），2010年3月

土屋範芳，石橋琢也，渡邉則昭，岡本敦，平野伸夫，き裂系における地殻流体の流動，日本地球惑星科学連合　2010年大会，幕張（千葉），2010年5月

石橋琢也，渡邉則昭，平野伸夫，岡本敦，土屋範芳，花崗岩フラクチャーの間隙構造における寸法依存性の評価，石油技術協会　平成22年度春季講演会，博多（福岡），2010年6月

石橋琢也，渡邉則昭，平野伸夫，岡本敦，土屋範芳，封圧下におけるフラクチャー内流体流動のマルチスケールモデリング，石油技術協会　平成23年度春季講演会，代々木（東京），2011年6月

石橋琢也，渡邉則昭，平野伸夫，岡本敦，土屋範芳，GeoFlowによるマルチスケールフラクチャーネットワークの流体流動特性の評価と予測，石油技術協会　平成24年度春季講演会，秋田（秋田），2012年6月

渡邉則昭，櫻井圭介，石橋琢也，土屋範芳，封圧下フラクチャーにおける二成分二相流に関する相対浸透率測定および数値モデリング，石油技術協会　平成24年度春季講演会，秋田（秋田），2012年6月

石橋琢也，渡邉則昭，玉川哲也，平野伸夫，岡本敦，土屋範芳，3Dチャネリングフローのモデリング手法とフィールドスケールへの拡張，日本地熱学会　平成24年度学術講演会，湯沢（秋田），2012年10月

石橋琢也，渡邉則昭，櫻井圭介，玉川哲也，平野伸夫，岡本敦，土屋範芳，フィールドスケール岩石き裂ネットワーク内での3Dチャネリングフロー，日本地球惑星科学連合　2013年大会，幕張（千葉），2013年5月

石橋琢也，渡邉則昭，土屋範芳，Thomas P. McGuire, Derek Elsworth，石灰岩フラクチャーの浸透率の時間発展に関する実験的検討とM−C連成モデリング，石油技術協会　平成25年度春季講演会，代々木（東京），2013年6月

渡邉則昭，石橋琢也，土屋範芳，玉川哲也，GeoFlowを用いたき裂型貯留層における優先流路分布の評価，石油技術協会　平成25年度春季講演会，代々木（東京），2013年6月

櫻井圭介，渡邉則昭，石橋琢也，土屋範芳，大崎豊，八木正彦，玉川哲也，封圧下石灰

岩および花崗岩フラクチャーにおける油−水相対浸透率曲線の評価，石油技術協会平成25年度春季講演会，代々木（東京），2013年6月

石橋琢也，渡邉則昭，土屋範芳，せん断変位および寸法により定式化される岩石き裂の水理学的特性，日本地熱学会　平成25年度学術講演会，幕張（千葉），2013年11月

Poster presentations in domestic conferences

石橋琢也，渡邉則昭，平野伸夫，土屋範芳，き裂不均質間隙構造の寸法依存性を考慮した“GeoFlow”による3次元チャネリングフローの精密モデリング，日本地熱学会　平成22年度学術講演会，つくば（茨城），2010年11月

石橋琢也，渡邉則昭，平野伸夫，岡本敦，土屋範芳，二次元フラクタル則による岩石き裂内流体流動モデルのスケールアップ，日本地熱学会　平成23年度学術講演会，指宿（鹿児島），2011年11月

櫻井圭介，渡邉則昭，石橋琢也，土屋範芳，実験および数値解析による封圧下花崗岩き裂における非混和二相流動特性の解明，日本地熱学会　平成 24 年度学術講演会，湯沢（秋田），2012 年 10 月